ALIGNMENT ISSUES IN LASER INTERFEROMETRIC GRAVITATIONAL-WAVE DETECTORS

by

NERGIS MAVALVALA

B.A. Wellesley College
(1990)

Submitted to the Department of Physics in partial
fulfillment of the requirements for the degree of

DOCTOR OF PHILOSOPHY

at the

MASSACHUSETTS INSTITUTE OF TECHNOLOGY

January, 1997

Author .....
Department of Physics
January, 1997

Certified by .....
Rainer Weiss
Department of Physics
Thesis Supervisor

Accepted by .....
George Koster
Chairperson
Department of Physics

Abstract

In this work we present a detailed quantitative study of the effects of angular misalignment in gravitational wave detectors. To analyze complex optical configurations we have developed a mathematical formalism which is powerful enough to accurately predict the effects of misalignment in coupled cavity systems, such as the LIGO (Laser Interferometric Gravitational-wave Observatory) interferometer. This formalism describes misaligned mirrors and free space propagation as operators acting on the eigenmodes of the perfectly aligned system and treats distortion effects as perturbations. Operators representing complicated optical systems are recursively built upon simpler ones, allowing a straightforward generalization to arbitrarily complex optical configurations. This model has been pivotal in determining the sensitivity to misalignment of the LIGO detector and for designing an automatic alignment system for an interferometer with ten angular degrees of freedom. Phase modulated light circulating in the interferometer is used to discriminate different angular degrees of freedom and to accurately measure misalignment angles. This *wavefront sensing technique* enables sensing of the angular misalignment of the interferometer mirrors relative to the incoming laser beam by spatial sampling of the optical wavefront, thus providing robust error signals for an angular servo system. The wavefront sensing system was successfully implemented on a table-top scale fixed mirror interferometer (FMI) featuring an optical configuration very similar to LIGO: a power recycled Michelson interferometer with Fabry-Perot cavities in the arms. In the FMI experiment four longitudinal degrees of freedom were controlled to maintain resonance and the measured wavefront sensing signals were also used to feedback to the angle actuators of the interferometer mirrors, making this the first interferometer with a LIGO configuration to accomplish closed loop servo control of all *ten* angular degrees of freedom. Good agreement was found between the model predictions and the measured wavefront sensing signals, with typical experimental errors of order ±20%. Quantitative understanding of the alignment sensitivity and implementation of an automatic alignment system using the wavefront sensing technique marks significant progress towards achieving the sensitivity goals of LIGO.

Acknowledgments

I have had the incredible good fortune of interacting with some of the finest scientists possible in the completion of this work. This makes it quite a challenge to keep the acknowledgments briefer than the actual thesis.

I am most deeply indebted to Daniel Sigg, from whom I have learned the science and art of doing an experiment. Daniel has provided hardware, software, ideas, discussions, synergistic presence and friendship, all of which were instrumental to the success of our experiment. We have collaborated closely on the work presented in this thesis and I hope it is a worthwhile reflection of our work together.

I also thank Yaron Hefetz, with whom the FMI alignment experiment got started and who set the stage for a thorough and complete experiment. The modal model implementation presented in this work was first developed by Yaron, from whom I have learned the importance of modeling and design.

I thank Rai Weiss for motivation and guidance in this work and for Reform School; Peter Fritschel and Gabriela González for countless discussions and patient explanations on a variety of topics; David Shoemaker, Mike Zucker and Stan Whitcomb for scientific insights and for general support of our costly experimental (ad)ventures; and all my colleagues in the lab for their willing assistance and for creating an amicable and productive environment.

I would specifically like to thank Daniel Sigg, Rich Abbott and Jay Heefner for the design and fabrication of the wavefront sensors and demodulator boards, and Daniel for patiently calibrating them all; Dave Barker for getting our VME data acquisition system started; Peter Csatorday for making the fast PZT actuators; Marcus Bennett for fabrication of RF photodiodes, 3-shooters and power supplies; and Daniel for much of the remaining electronics (compensation networks, filters, etc.). In addition, Daniel's patient perusal of this thesis and editorial comments have been invaluable.

I thank my parents and sister for constant support and encouragement; my housemates at Saint Paul Street for friendship, meals and good times; and fellow squashers for keeping me sane, on and of the courts.

Finally, I thank Nadia, who makes everything possible.

Table of Contents

Chapter 1

Introduction

1.1 Laser interferometric gravitational wave detectors

Einstein's theory of general relativity predicts the existence of gravitational waves [1]. Radiated by all accelerating aspherical mass distributions, gravitational waves are a ripple in the curvature of spacetime, propagating at the speed of light. They are essential for preserving causality since a gravitational field cannot change instantaneously [2]. The impetus to detect gravitational radiation is great: a direct detection of gravitational waves would unequivocally prove their existence and would be the first measure of their propagation characteristics; more importantly, since astrophysical sources are believed to be the most likely emitters of detectable gravitational radiation and since all known forms of matter are extremely transparent to gravitational waves, it would provide a new and hitherto unexplored window into the universe. Also of profound interest is the physics of strong gravitational fields at the source.

Gravitational radiation produces a strain in space transverse to the direction of propagation. In the weak field limit, using the transverse-traceless gauge, the gravitational-wave strain,

$$h = 2\frac{\Delta L}{L} \tag{1}$$

is a measure of the fractional change, ΔL, in a length of space, L, caused by a passing gravitational wave. The amplitude of the gravitational radiation from even the most promising astrophysical sources is tiny; for neutron star binaries in the nearby Virgo cluster it is typically $h = 10^{-21}$ in the dimensionless units of strain [2]. Since gravitational waves are quadrupolar, the strain has opposite signs along two transverse orthogonal axes, causing a differential displacement of free masses placed on these axes. Variants of a Michelson interferometer have been proposed to measure the gravitational

wave strain by detecting differential changes in the arm lengths, as shown in Fig. 1.1 [3], [4]. For a path length change, ΔL, the light power detected at the antisymmetric port is

$$P_{anti} = P_{in} sin^2(2k\Delta L) \tag{2}$$

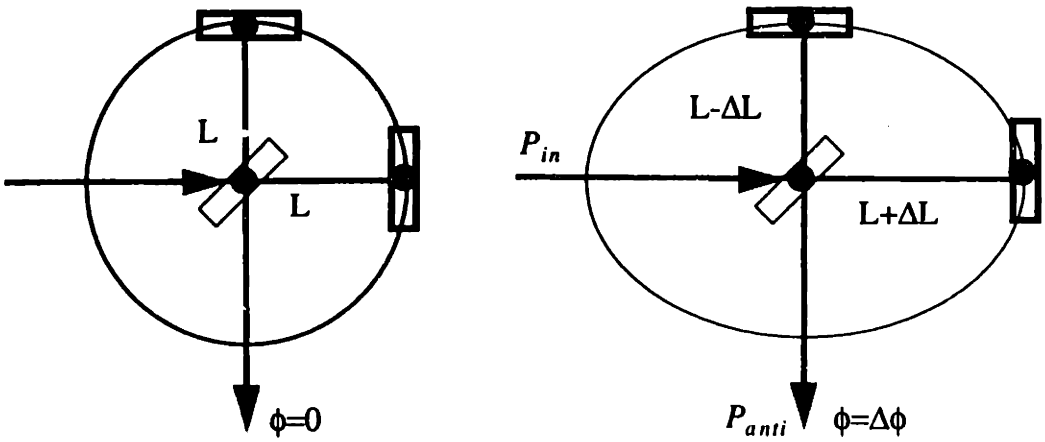

Figure 1.1: A gravitational wave incident normal to the plane interacts with the "freely" suspended mirrors of a Michelson interferometer with arm length L, alternately stretching and shrinking the orthogonal arms by ΔL each half-cycle.

For gravitational waves with periods much greater than the round-trip time of light in the arm of a Michelson interferometer the optical path length change is $\Delta L(t) = h(t)L/2$, so the relative change of phase between two interfering beams is $\Delta\phi(t) = 4\pi h(t)L/\lambda$, where λ is the wavelength of the light. If the Michelson arms are made longer, the phase sensitivity increases until the round-trip time becomes comparable to the gravitational wave period. A maximum is reached when the arm length is equal to one quarter of the wavelength of the gravitational wave.

From an astrophysical standpoint it is desirable to detect gravitational waves at very low frequencies, which would require very long Michelson arms. But practical considerations limit the arm lengths to a few kilometers, and a high phase sensitivity is obtained by using "multiple-bounce" techniques in the interferometer arms [4], [5].

The Laser Interferometric Gravitational-wave Observatory (LIGO) comprises of two long baseline interferometric detectors, currently under construction in Hanford, WA, and

Livingston, LA [6]. For a strain $\delta h \approx 10^{-22}/\sqrt{\text{Hz}}$ and antenna arm length $L = 4$ km, the path length change is $\delta L = \delta h L \approx 10^{-19}$ m$/\sqrt{\text{Hz}}$, which corresponds to an optical phase $\delta\phi = 4\pi b L \delta h/c \approx 10^{-10}$ rad$/\sqrt{\text{Hz}}$[1]. To achieve this sensitivity, required to measure strains of astrophysical interest, the LIGO interferometers, along with their international counterparts, are up to 4 km long and comprise of optical configurations which are significantly more complex than a simple Michelson interferometer. A typical interferometer configuration, currently planned for the LIGO interferometer, is comprised of a Michelson interferometer with Fabry-Perot optical cavities in each arm and a partially transmitting "power recycling" mirror between the input laser and the beamsplitter (see Fig. 1.2).

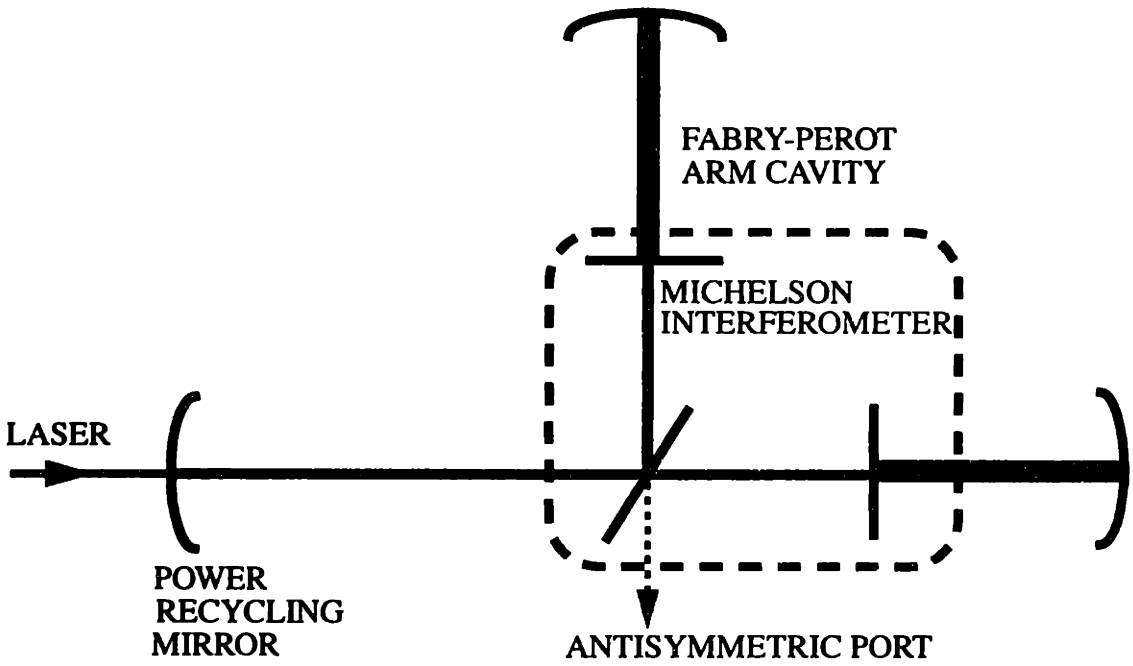

Figure 1.2: Optical components of a realistic gravitational wave antenna.

The sensitivity of the detector is limited by *displacement noise*, due to mirror motions caused by stimuli other than gravitational waves and *phase noise*, due to quantum mechanical shot noise in the detection of photons [7]. These noise sources dominate the detector noise budget in different frequency bands: seismic noise, for example, is a

1. Here $b \sim 100$ is the *bounce* number, that is, the mean number of times the photons traverse each arm of the Michelson interferometer. This is explained in Section 2.1.

dominant noise source at frequencies below 70 Hz, while shot noise limits the detector sensitivity at frequencies above 200 Hz.

1.2 Sensitivity to alignment

Since angular misalignment of the interferometer mirrors can both decrease the power built up in the arm cavities and increase the shot noise load at the gravitational wave signal extraction port, the sensitivity of the interferometer to gravitational wave strain depends on good angular alignment of the interferometer with respect to the incoming laser beam. To set the scale of the alignment precision required for the LIGO interferometer, we observe that directing the laser beam down the 4 km arms and having it return to within one spot diameter (typically ~10 cm) requires a pointing precision of $\sim 10^{-5}$ radian. For the purposes of interferometry, however, the beam overlap must be correct to within a tiny fraction of the beam diameter. In fact, to ensure that mirror misalignment does not degrade the gravitational wave sensitivity in LIGO by more than 0.5% of the maximum for a perfectly aligned interferometer requires the absolute alignment of each mirror relative to the incoming laser beam to be better than 10^{-8} rad [8], [9]. Furthermore, static or low frequency misalignment of the interferometer mirrors couples input beam jitter (direction fluctuations) into differential phase shifts which lead to spurious signals in the gravitational wave readout. To prevent this effect from degrading the gravitational wave sensitivity by more than 0.5%, the fluctuations of the input beam direction at 100 Hz must be less than 10^{-14} rad/$\sqrt{\text{Hz}}$, assuming an rms alignment of 10^{-8} rad per mirror [10].

Moreover, it is not sufficient to align the mirror angles individually relative to a local frame by using, for instance, optical levers. For typical environmental noise inputs to the interferometer, and after attenuation by passive isolation stacks and local damping, the LIGO suspended optics are expected to drift by $\sim 10^{-7}$ rad over a 100 sec timescale [11]. Since these drifts are an order of magnitude larger than the required alignment tolerance (per degree of freedom), there is no viable local fiducial point, and interferometric alignment of the detector is imperative. More importantly, for maximum sensitivity, the incident laser beam is intrinsically the best reference frame to which the interferometer must be aligned. To this end, we use the light already circulating in the interferometer to sense angular misalignments, a technique we call *wavefront sensing*.

1.3 Purpose of this work

In this work we present a detailed quantitative study of the effects of angular misalignment in gravitational wave detectors. Prior to this, an analytical treatment was used to develop an alignment system for a two mirror resonator [12], but this formulation was not readily extensible to other optical systems. To analyze more complex optical configurations we have developed a mathematical formalism which is powerful enough to accurately predict the effects of misalignment in coupled cavity systems, such as the LIGO interferometer [13]. This formalism describes misaligned mirrors and free space propagation as operators acting on the eigenmodes of the perfectly aligned system and treats distortion effects as perturbations. Operators representing complicated optical systems are recursively built upon simpler ones, allowing a straightforward generalization to arbitrarily complex optical configurations. This model has been pivotal in determining the sensitivity to misalignment of the LIGO detector (highlighted in Section 1.2) and for designing an automatic alignment system for an interferometer with ten angular degrees of freedom. Phase modulated light circulating in the interferometer is used to discriminate different angular degrees of freedom and to accurately measure misalignment angles. This *wavefront sensing technique* enables sensing of the angular misalignment of the interferometer mirrors relative to the incoming laser beam by spatial sampling of the optical wavefront, thus providing robust error signals for an angular servo system. The wavefront sensing system was successfully implemented on a table-top scale fixed mirror interferometer (FMI) featuring an optical configuration very similar to LIGO: a power recycled Michelson interferometer with Fabry-Perot cavities in the arms. In the FMI experiment four longitudinal degrees of freedom were controlled to maintain resonance and the measured wavefront sensing signals were also used to feedback to the angle actuators of the interferometer mirrors, making this the first interferometer with a LIGO configuration to accomplish closed loop servo control of all *ten* angular degrees of freedom. Good agreement was found between the model predictions and the measured wavefront sensing signals, with typical experimental errors of order ±20%. Quantitative understanding of the alignment sensitivity and implementation of an automatic alignment system using the wavefront sensing technique marks significant progress towards achieving the sensitivity goals of LIGO.

Chapter 2

Optical configuration of the interferometer

2.1 Optical layout of the interferometer

The principle of interferometric detection of gravitational waves is based on measuring optical phase shifts due to changes in the path length caused by a passing gravitational wave. The goal then is to convert gravitational wave strain into optical phase shifts as efficiently as possible. This leads to the optical layout of a LIGO-like gravitational wave detector shown in Fig. 1.2. The laser light enters the interferometer through the partially transmitting "power recycling" mirror, gets amplified by the Fabry-Perot cavities in the arms of the Michelson interferometer and the gravitational wave signal is detected at the antisymmetric port, which is often called the signal extraction port or dark port.

2.1.1 Michelson interferometer

Before discussing the full LIGO configuration we first consider a simple Michelson interferometer [14]. It is formed by the beamsplitter, the in-line (collinear with the incident laser beam) and perpendicular arm input mirrors. The phase shift per length change in each arm is given by $d\phi/dl = 4\pi/\lambda$ (here λ is the wavelength of light) or

$$d\phi(t) = h(t)\tau_{rt}\frac{2\pi c}{\lambda} \tag{3}$$

where $\tau_{rt} = 2L/c$ is the round-trip travel time for photons leaving and returning to the beamsplitter. Eqn. (3) is only valid if $\tau_{rt} \ll \tau_{gw}$. For longer arms $h(t)$ cannot be considered constant over the length of the antenna. This leads to the interferometer response for arbitrary τ_{rt}:

$$d\phi(t) = h(t)\tau_{rt}\frac{2c}{\lambda}sinc(\pi f_{gw}\tau_{rt})exp(i\pi f_{gw}\tau_{rt}) \tag{4}$$

From eqn. (4) the phase sensitivity has a maximum at $\tau_{rt} = \tau_{gw}/2$. A gravitational wave with $f_{gw} = 100$ Hz corresponds to a maximum phase sensitivity for $\tau_{rt} = 5$ msec or $L = 750$ km. This is an impractical length for interferometer arms which must span the

curved surface of the earth in a vacuum. To make the arm lengths shorter but retain maximal phase sensitivity at 100 Hz, optical "folding" schemes to increase the time the photons spend in the arms have been proposed [4], [5]. In the simplest case (delay line) photons bounce b times in the arms, that is, the light makes b round trips, then the round-trip time, τ_{rt}, in eqn. (4) can be replaced by the storage time $\tau_s = b\tau_{rt} = \frac{2bL}{c}$. In this case, the photons traverse the gravitational wave strain induced length change b times. If the arms are 4 km long, for example, $b \approx 200$ would give $\tau_s = 5$ msec, the storage time for optimal detection of a gravitational wave at 100 Hz. Thus "folding the arms of the interferometer allows for shorter arm lengths while retaining maximum phase sensitivity by "storing" the photons. Two examples of light storage schemes are illustrated in Fig. 2.1. In the optical delay line the light strikes the mirror at a different spot on each traversal of the arm. In the resonant Fabry-Perot cavity light in a single spot constructively interferes at each traversal, effectively averaging the field in the cavity over several traversals.

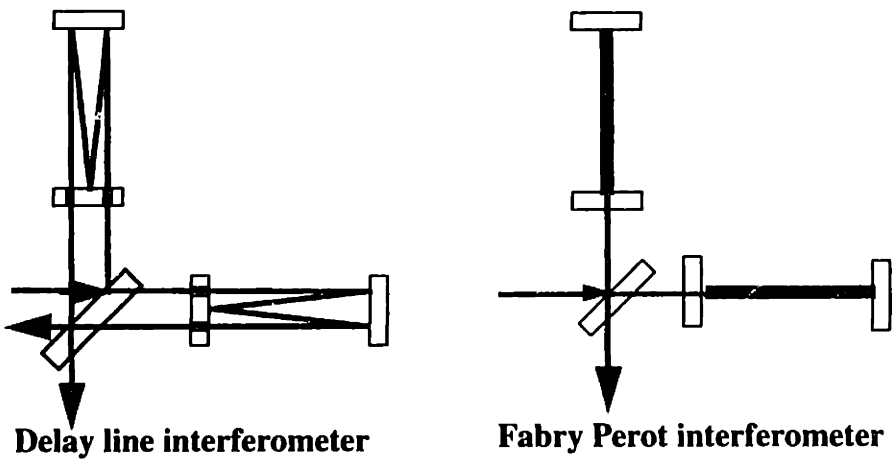

Figure 2.1: Two kinds of light "storage" schemes.

2.1.2 Fabry-Perot arm cavities

In LIGO the light storage scheme of choice is Fabry-Perot cavities in the arms of the Michelson interferometer. The interferometer response for such a scheme is given by

$$d\phi(t) = h(t)\frac{8\pi c}{\lambda}\frac{1}{\sqrt{1+(4\pi f_{gw}\tau_s)^2}} \tag{5}$$

which is the response of a simple pole at $f = 1/(4\pi\tau_s)$. For $f_{gw}\tau_s \gg 1$, $d\phi \approx 2ch/\lambda f_{gw}$, that is, the phase sensitivity is inversely proportional to the signal frequency and independent of the storage time. The choice of storage time — or equivalently, the cavity pole — is dictated by noise considerations. Since there is no point in increasing sensitivity at low frequencies which are dominated by seismic noise, the cavity pole is chosen just below the practical limits of the LIGO seismic wall (100 Hz or $\tau_s \approx 1$ msec). This choice simultaneously maximizes the gravitational wave sensitivity in the frequency band of interest and minimizes the loss in the Fabry-Perot arm cavities. This, in turn, allows the light returning to the laser to be reflected back into the laser using a "power recycling" scheme, further enhancing the detector sensitivity.

2.1.3 Power recycling

Strain sensitivity is increased when more light power is incident on the beamsplitter. This is due to photon counting statistics or shot noise. Phase fluctuations due to the quantum mechanical uncertainty in the number of photons detected at the antisymmetric port of the detector can be expressed as

$$\tilde{\phi} = \sqrt{\frac{2h\nu}{\varepsilon P}} \tag{6}$$

where $h\nu$ is the energy of each photon, ε is the detection efficiency of and P is the power incident on the photodetector. To be maximally sensitive to fluctuations about a null point, the interferometer is operated at a dark fringe, that is, at $\Delta L = n(\lambda/4)$, where n is an integer, such that P_{anti} in eqn. (2) is at a minimum [4]. Now most — not all, since a realistic interferometer has losses and contrast defect — of the power reflected from the arm cavities exits through the symmetric port of the beamsplitter, i.e almost all of the light is returned to the laser. This light is "recycled" back into the interferometer upon reflection from a partially transmitting recycling mirror placed between the laser and the beamsplitter [5], [15]. This increases the light incident on the beamsplitter by a recycling gain factor, G_{rec}. From eqn. (2), the gravitational wave induced signal at the antisymmetric port scales as the power and is enhanced by G_{rec}, but the shot noise grows as the square root of the power, or $\sqrt{G_{rec}}$. The overall strain sensitivity is increased by $\sqrt{G_{rec}}$. The typical power recycling gain expected for the LIGO detector is between 30 and 50.

2.2 The length sensing scheme

The necessity for a length sensing scheme is a consequence of the technical difficulties of building an interferometer which is mechanically and thermally stable enough to hold the mirrors at positions where the conditions for perfect interference are satisfied. Moreover, dark fringe operation at the antisymmetric port leads to a quadratic dependence of P_{anti} to gravitational wave strain, so a more sensitive signal extraction technique must be used. A sensing scheme which measures deviation from resonance conditions is imperative for the gravitational wave detector. These "error signals" are then used to feedback to the mirror positions and maintain the resonance and dark fringe conditions in the interferometer. In this chapter we develop the design of a length sensing scheme based on RF modulation techniques and then extend it to design an alignment sensing scheme, with general applicability to the FMI and the LIGO detector.

2.2.1 The reflection locking technique

Reflection locking is a powerful heterodyne phase detection technique for holding optical cavities on resonance [16], [17]. Since maintaining resonance conditions in Fabry-Perot cavities is central to the development of this work, it is worth discussing some of the physics behind it here. A typical LIGO-like Fabry-Perot cavity consists of a partially transmitting input mirror and a highly reflective end mirror, separated by a distance, l (see Fig. 2.2).

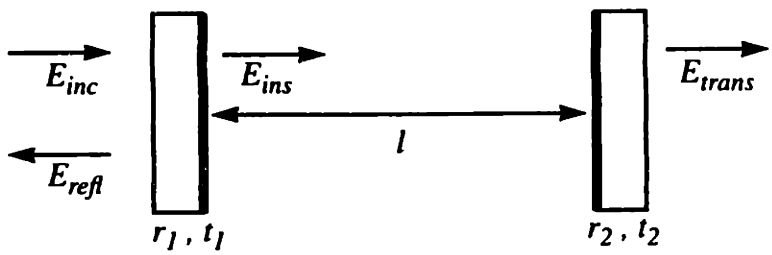

Figure 2.2: A Fabry-Perot cavity of length, l. r_i and t_i are the amplitude reflection and transmission coefficients of the i-th mirrors, respectively.

For an input field, E_{inc}, the fields, as defined in Fig. 2.2, are:

$$E_{ins} = \frac{t_1}{1 - r_1 r_2 exp(-2ikl)} E_{inc} \tag{7}$$

$$E_{trans} = \frac{t_1 t_2 exp(-ikl)}{1 - r_1 r_2 exp(-2ikl)} E_{inc} \tag{8}$$

$$E_{refl} = \frac{r_1 - r_2 exp(-2ikl)}{1 - r_1 r_2 exp(-2ikl)} E_{inc} \tag{9}$$

where $k = 2\pi f/c$ and cavity loss coefficients are combined with transmission losses. Resonance occurs when the round-trip phase $2ikl = 2\pi$. The complex phase in the above expressions immediately implies that the fields have a frequency dependence (spectrum) when the cavity has fixed length, l.

When phase modulated light is incident on an optical cavity, then deviation from the resonance length causes amplitude modulation of the light reflected from the cavity. Close to the resonant state, the magnitude of the amplitude modulation is proportional to the deviation from resonance, while the sign of the phase gives the direction of deviation from the resonant length and can be used as an error signal to hold the cavity on resonance.

When light from the laser is phase modulated at an angular frequency, Ω, the field incident on the cavity is

$$\begin{aligned} E_{inc} &= E_0 exp(i\Gamma cos(\Omega t)) \\ &\approx E_0 exp(i\omega_0 t)[J_0(\Gamma) + J_1(\Gamma) exp(i\Omega t) + J_{-1}(\Gamma) exp(-i\Omega t)] \end{aligned} \tag{10}$$

for $\Gamma \ll 1$. The first term is the carrier, while the second and third terms are phase modulation sidebands at frequencies $(\omega_0 + \Omega)$ and $(\omega_0 - \Omega)$, respectively. The $J_i(\Gamma)$ are Bessel functions, where the amplitude of the carrier is $J_0(\Gamma) \approx 1$ and for the first-order sidebands $J_{\pm 1}(\Gamma) \approx \pm\Gamma/2$ for modulation depth, $\Gamma < 1$. The field reflected from the cavity is also made up of three components, the carrier and the two sidebands, but the cavity with fixed length has a different reflection coefficient for each frequency, denoted by the complex quantities E^{refl} in eqn. (11). Alternatively, each frequency becomes resonant for a different length of cavity. The total reflected field is

$$E_{refl} = [E_0^{refl} + E_+^{refl} exp(i\Omega t) + E_-^{refl} exp(-i\Omega t)] exp(i\omega_0 t) \tag{11}$$

which corresponds to a photocurrent (a photodiode being a square-law detector):

$$\begin{aligned} i = {} & [|E_0|^2 + |E_+|^2 + |E_-|^2] + \\ & [(E_0^* E_+ + E_0 E_-^*) exp(i\Omega t) + CC] + \\ & [E_+ E_-^* exp(2i\Omega t) + CC] \end{aligned} \tag{12}$$

The superscript *refl* is omitted for tractability. The first line in eqn. (12) is the DC photocurrent, the second and third lines give the photocurrent at angular frequencies Ω and 2Ω, respectively. Multiplying the terms in Ω by $cos(\Omega t)$ and averaging over one cycle leads to the in-phase demodulated signal

$$v_I = Re\{E_0^* E_+ + E_0 E_-^*\} \tag{13}$$

and the quadrature phase signal is given by demodulating with $sin(\Omega t)$

$$v_Q = Im\{E_0^* E_+ + E_0 E_-^*\} \tag{14}$$

The demodulator signal at Ω is due to the beating of the carrier with each modulation sideband. Only the carrier is within the resonance linewidth of the cavity and the sidebands are promptly reflected from the input mirror. The carrier, which is stored in the cavity, experiences a phase shift as the cavity length drifts away from resonance. The sidebands, of course, do not. The relative phase between the carrier and the sidebands changes, giving rise to a beat signal. The sidebands, then, can be treated as a constant phase reference for the carrier to beat against.

The DC photocurrent and in-phase demodulator signal for the field reflected from a Fabry-Perot cavity as a function of cavity length are shown in Fig. 2.3. Near resonance, at $l = 0$, the demodulator signal is linearly proportional to l and serves as the error signal for feedback to the cavity mirrors, adjusting their separation to maintain resonance. Null servos such as this are highly desirable since they provide an unambiguous "locking" or zero point.

The optical configuration of the initial LIGO detector consists of a power recycled Michelson interferometer with Fabry-Perot cavities in each arm, as shown in Fig. 2.4. RM refers to the recycling mirror, ITMs and ETMs refer to input and end test masses, respectively, and BS refers to the beamsplitter. The laser light enters the interferometer through the partially transmitting recycling mirror and the gravitational wave signal is detected at the antisymmetric or signal extraction port. The recycling cavity is the optical resonator made up of the RM as an input mirror and the symmetric port of the beamsplitter which can be thought of as a complex rear mirror. The resonance conditions for the recycling and arm cavities are maintained using servo control, as is the dark port condition which requires that no light exit the antisymmetric port. Four lengths are controlled to maintain resonance for the arm cavities and to hold the Michelson on the dark fringe at the

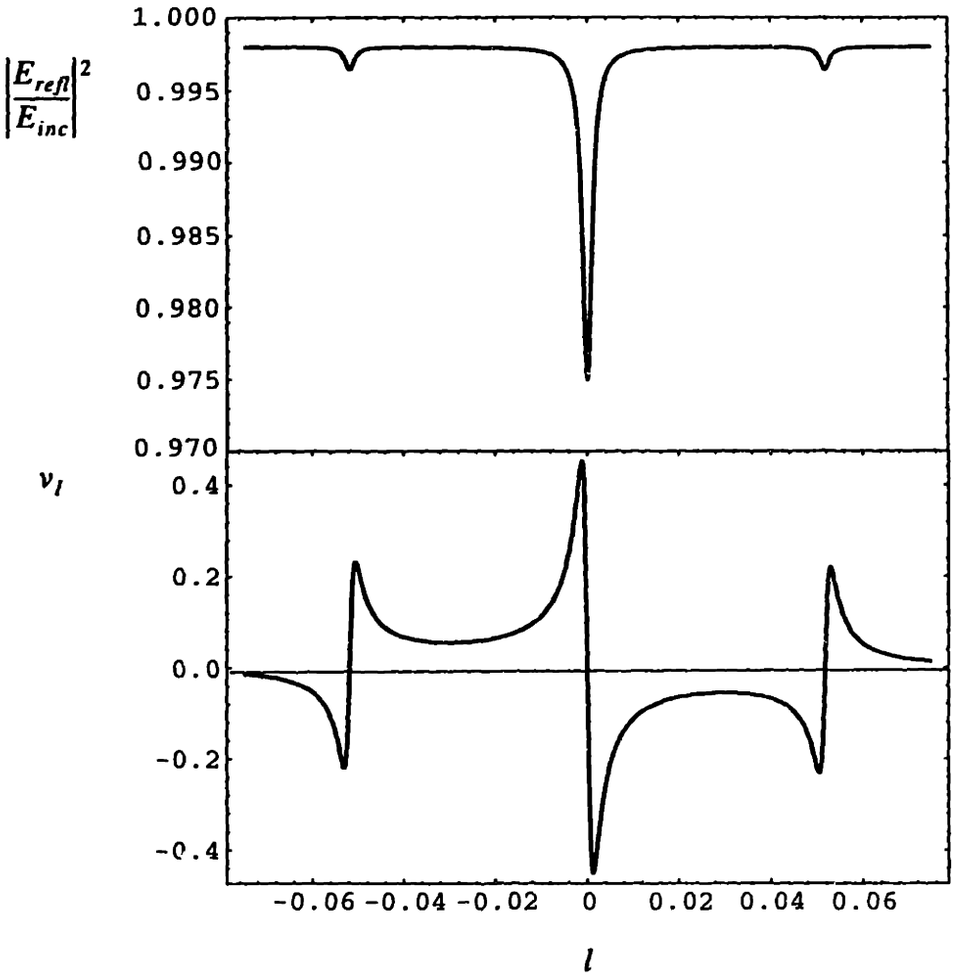

Figure 2.3: The squared amplitude of the reflected field (upper) and the demodulated signal (lower) as a function of the cavity length (in units of wavelength) for a Fabry-Perot cavity with incident phase modulated light. The cavity parameters are those of a typical LIGO cavity (see Section 2.3).

antisymmetric port. These are the arm cavity lengths, L_1 and L_2, and the lengths of the Michelson arms, l_1 and l_2. The arm cavity lengths, L_1 and L_2, are nominally 4 km, while the nominal recycling cavity length $(l_2 + l_2)/2$ is 6 to 15 m and the asymmetry $(l_2 - l_2)/2$ is about 17 cm. The design considerations motivating the vastly different length scales for the various interferometer lengths, intimately related to the longitudinal sensing scheme used, are explained in Section 2.3.

A number of length sensing techniques based on the heterodyne phase detection scheme discussed above can be used to control all four longitudinal degrees of freedom

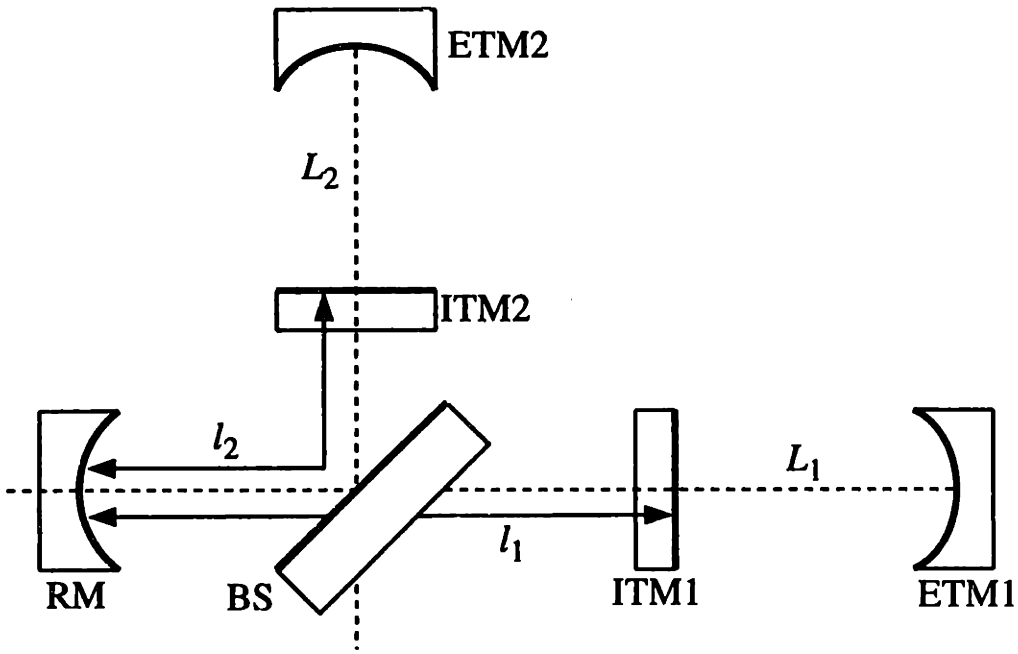

Figure 2.4: Schematic representation of a typical interferometric gravitational wave detector

[18], [19], [20]. Regehr's work [18], [19] details a *single carrier frontal* modulation scheme where the carrier and a pair of phase modulation sidebands are used to probe all four lengths of an interferometer with *asymmetry readout* [21]. Giaime [20] uses a *multiple carrier frontal* modulation scheme with *external modulation* (or Mach-Zehnder) *readout* [22]. In the FMI experiment we use the *multiple carrier frontal* modulation scheme with *asymmetry readout*, which is a synthesis of the above two schemes. It is a modulation scheme with multiple modulation frequencies carefully chosen to ensure that the different frequencies are resonant in some parts of the interferometer but not in others. Frequencies which do not resonate at certain interferometric lengths serve as a constant phase reference to probe those lengths.

The multiple carrier modulation scheme is used in the FMI experiment Since the design of an alignment sensing scheme for LIGO using single carrier modulation requires some extension of the scheme in Regehr *et al.* [18], a modified single carrier scheme is described briefly in Section 2.2.2. The configuration of an interferometer using the multiple carrier modulation scheme is the subject of the rest of this chapter.

2.2.2 Single carrier modulation scheme

The phase modulated light incident on the interferometer comprises of a carrier (C) with two pairs of phase modulation sidebands, one pair is resonant in the recycling cavity (CSB) and other is not (CNR), as shown in Fig. 2.5. The non-resonant sidebands are included to extract distinguishable signals for common misalignment of the ITMs and RM misalignment. This effect is a consequence of the highly degenerate recycling cavity in LIGO and is discussed later.

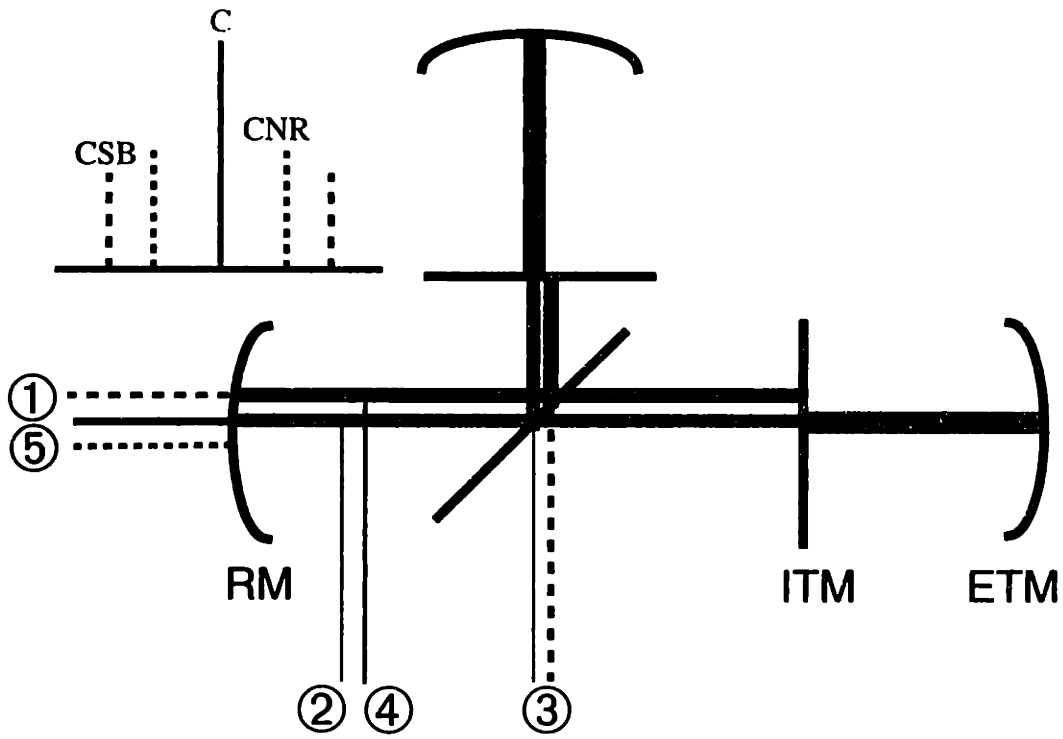

Figure 2.5: Schematic representation of the modified single carrier modulation scheme. Thicker lines represent resonance in a particular interferometer length. The inset on the top left is the spectrum of the input light.

The C resonates in the arm cavities and the recycling cavity, the CSB resonate in the recycling cavity only and the CNR do not couple to the interferometer. Insofar as the length sensing scheme is concerned, the non-resonant sidebands are not used and length sensing signals are extracted following the method of Regehr *et al.* [18]. In Table 2.1 we list the fields that interfere, where in the interferometer the interfering fields are sensed and the longitudinal degrees of freedom to which they are sensitive. Note that we express

the length degrees of freedom as linear combinations of the lengths shown in Fig. 2.4, defined as

$$L_D = \frac{L_1 - L_2}{2} \text{ and } L_C = \frac{L_1 + L_2}{2}$$
$$l_D = \frac{l_1 - l_2}{2} \text{ and } l_C = \frac{l_1 + l_2}{2} \quad (15)$$

INTERFERING FIELDS (RF PHASE)	DETECTION PORT	DEGREES OF FREEDOM
LS1: C and CSB (I)	reflection	$L_C + \varepsilon_1 l_C$
LS2: C and CSB (I)	recycling	$L_C + \varepsilon_2 l_C$
LS3: C and CSB (Q)	antisymmetric	$L_D + \varepsilon_3 l_D$
LS4: C and CSB (Q)	recycling	$\varepsilon_4 L_D + l_D$

Table 2.1: Signal sensitivity to longitudinal degrees of freedom for the single carrier scheme. LS*i* refers to the length sensor probing the *i*-th field (see Fig. 2.5).

The ε_i are small coefficients and we see that the signals LS3 and LS4 can be used to probe L_D and l_D, respectively. However, both LS1 and LS2 are most sensitive to L_C and relatively insensitive (by a factor ε) to l_C. Regehr *et al.* circumvent this degeneracy by operating the LS1 servo loop feeding back to L_C with a much higher gain than the others, which drives the L_C deviations to zero and the dominant term in the LS2 signal becomes proportional to l_C.

The multiple carrier modulation scheme is an alternative which does not encounter this degeneracy and is discussed below.

2.2.3 Multiple carrier modulation scheme

For the multiple carrier modulation scheme, the spectrum of the input light is comprised of three families of frequencies (see Fig. 2.6). These are the carrier (C) and its sidebands (CSB) and the frequency-shifted subcarrier (SC) and two sets of sidebands (SCSB and SCNR). For the FMI the carrier is 514.5 nm light from a CW Ar^+ gas laser; for

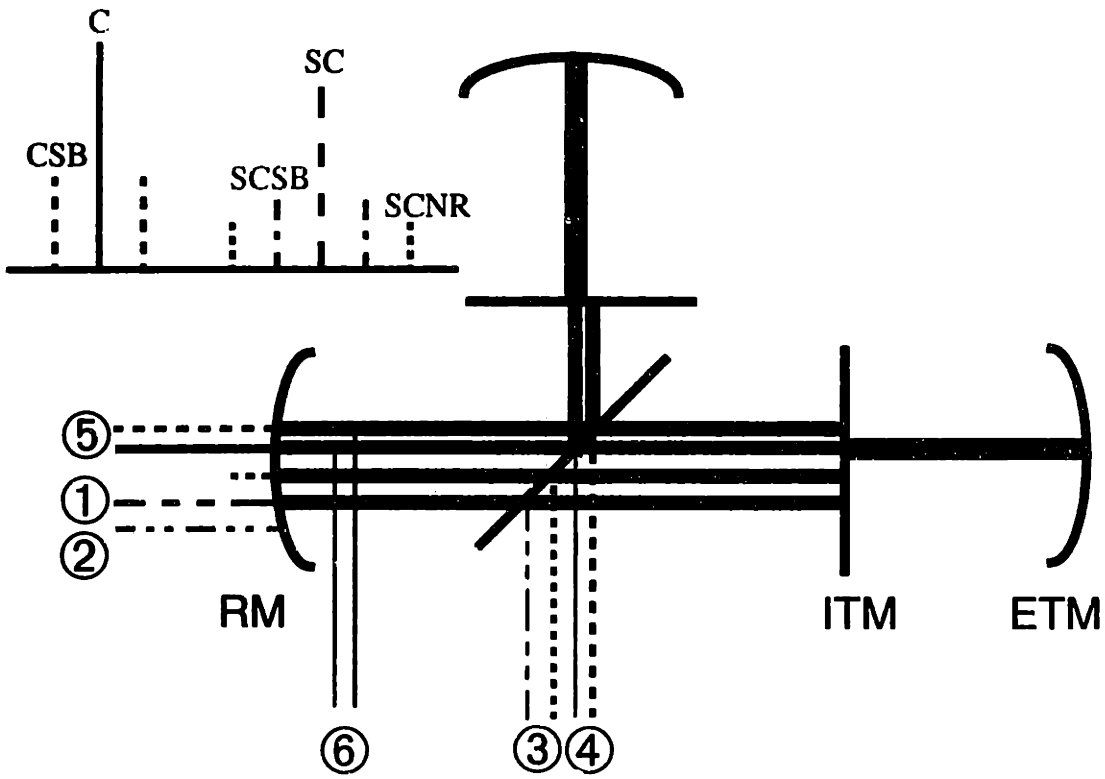

Figure 2.6: Schematic representation of the multiple frequency modulation scheme using a frequency-shifted subcarrier. Thicker lines represent resonance in a particular interferometer length. The inset on the top left is the spectrum of the input light.

LIGO it will be the 1.06 μm transition in a Nd:YAG solid state laser. In the multiple carrier scheme, each family of frequencies is sensitive to a particular degree of freedom at a given position in the interferometer. In Table 2.2 we list the fields that interfere, where in the interferometer the interfering fields are sensed and the longitudinal degrees of freedom to which they are sensitive.

Maximum sensitivity to a given degree of freedom is achieved when the sideband field is independent of that degree of freedom, so that it acts as a constant reference for interference with the carrier field (which changes proportionally with changes in length). For example, if the carrier resonates in the arm cavity, its sidebands must be sufficiently outside of the cavity resonance, so that only the carrier phase is sensitive to changes in cavity length. Further, the field at each frequency that propagates in the interferometer must be resonant in the recycling cavity for maximum coupling.

Interfering Fields		Detection Port	Degree of Freedom
①	LS1: SC and SCNR	reflection	l_C
③	LS2: SC and SCSB	antisymmetric	l_D
④	LS3: C and CSB	antisymmetric	L_D
⑤	LS4: C and CSB	reflection	L_C

Table 2.2: Signals most sensitive to longitudinal degrees of freedom for the multiple carrier scheme. See Fig. 2.6 for corresponding fields.

With this in mind, we analyze the fields listed in Table 2.1. Sensitivity to multiple degrees of freedom necessitates multiple detectors. The fields to be detected and the resonant states of the various frequencies are schematically represented in Fig. 2.6.

We define the length sensing matrix L such that

$$S_i(t, \delta l) = 2J_0(\Gamma)J_1(\Gamma)P_i\sum_j L_{ij}\delta l_j cos(\Omega t + \phi_{ij}) \tag{16}$$

where S_i is the demodulator signal on the i-th sensor; δl_j is the change in length (normalized per unit wavelength) for the j-th degree of freedom; L_{ij} is the length sensitivity matrix; ϕ_{ij} is the intrinsic RF phase; P_i is the power on the detector; and Ω and Γ are the RF modulation frequency and depth, respectively. To ensure that the sensor signal, S_i, is sensitive to a single length degree of freedom and independent of any other length changes, L must be as diagonal as possible. This is a motivating concern for the interferometer design and is discussed in the following section.

2.3 Optical design using the multiple carrier modulation scheme

This section addresses the detailed optical design considerations for the Fixed Mirror Interferometer demonstration of the wavefront sensing system. The length control system uses the same baseline configuration as the initial LIGO interferometer, and is a synthesis of the earlier fixed mirror tests [19], [20]. In addition to being the experimental testbed for implementation of a complete alignment sensing and control scheme, the present FMI is also the first to employ this particular length control system, and many of the design

considerations are directly relevant to a full-scale LIGO design.

The optimal interferometer design, given our choice of basic configuration, involves a detailed study of several parameters. These include five mirror radii of curvature and mirror reflectivities, four lengths, and three families of frequency modulated light and their relative frequency shifts. The optimization of the cavity lengths, mirror curvatures, modulation frequencies and mirror reflectivities is a many-dimensional study. The choice of each of these parameters is subject to constraints, and each can impact one or more of the other parameters. The constraints can be a physical limitation, such as the finite dimensions of the optical layout, or a technical barrier, such as the maximum frequency at which Pockels cells can be modulated before beam distortion is intolerable, or of a scientific nature, such as the maximum asymmetry that can be tolerated before higher order modes due to phasefront curvature mismatch of the arm cavities degrades the detector performance. For the purposes of the FMI study, often the constraints are soft and the choice of an upper bound is informed but arbitrary.

In the following sections we describe the various parameters, constraints on those parameters, and the criteria used in the choice of each parameter vis-a-vis the complete interferometer. We list the physical and technical factors taken into consideration in the design of the optimal interferometer configuration, optimal being the configuration where L is most diagonal and sensitivity to the gravitational wave signal is maximum.

2.3.1 Modulation frequencies

For maximum coupling efficiency, the recycling cavity must be resonant for all frequencies that propagate in the interferometer.

The C and CSB are used to probe the arm cavity lengths, so the carrier is resonant in the arm cavity, while the CSB are outside the cavity resonance. Of course, both must resonate in the recycling cavity.

The SC and its sideband are used to detect deviations in the near Michelson lengths. To ensure that the SC frequency family is insensitive to the arm cavity lengths, we choose the frequency of the SC to be exactly antiresonant in the arm cavity, that is,

$$f_{SC} = \left(n + \frac{1}{2}\right) fsr_{ARM} = \left(n + \frac{1}{2}\right) \frac{c}{2L_1} \tag{17}$$

where n is an integer. Typically, the modulation indices are small ($\Gamma < 1$), so we neglect higher harmonics of the modulated fields. In the case of the SC which is anti-resonant in the arm cavities, however, if the input light has a significant second harmonic frequency component, the frequency of the SC must be detuned from perfect anti-resonance in the arm cavities to avoid a double resonance for its second harmonic.

The C, CSB, SC and SCSB must resonate in the recycling cavity. Upon reflection from the resonant arm cavity, the C acquires a phase shift of π relative to the CSB, which are outside the arm cavity resonance. The round trip phase that satisfies the resonance condition for the C is

$$\frac{2\pi f}{c} 2l_{RC} = (2n+1)\pi \tag{18}$$

where l_{RC} is the length of the recycling cavity. If the free spectral range of the recycling cavity is $2f_0$, where

$$f_0 = \frac{c}{4l_{RC}} \tag{19}$$

then the resonances of fields which resonate in the recycling cavity only occur at frequency intervals of $2f_0$. If all other frequencies are referenced to the carrier double resonance at $n = 0$, then the CSB resonate at frequency intervals of $2f_0$, but shifted by f_0 relative to the carrier resonance, that is,

$$\Delta\nu_{CSB} \equiv f_{CSB} = f_0, 3f_0, 5f_0, \ldots \tag{20}$$

The SC is chosen to be exactly antiresonant in the arm cavity, so we expect a relative phase shift of π between C and SC. The SC, however, experiences a phase shift of π due to the asymmetry. At the symmetric port of the Michelson, the field

$$r_M \propto cos\left(\frac{2\pi f}{c} 2a\right) \tag{21}$$

where the asymmetry (added in one arm, subtracted in the other) is $a = (l_1 - l_2)/2$. The reflection of the Michelson, r_M, varies sinusoidally as a function of frequency for a fixed asymmetry, a. Light at the frequency where $r_M = -1$ undergoes a phase shift of π. In effect, the carrier has a phase shift of π due to the arm cavity resonance, while the SC has a phase shift of π due to the asymmetry, hence there is no relative phase shift between

them. In the recycling cavity, for light at frequencies sufficiently far from the carrier, resonance occurs at intervals of $2f_0$, just as it does for the CSB. Consequently, the frequency of the SC relative to the carrier is given by

$$\Delta\nu_{SC} \equiv f_{SC} = nf_0$$
$$n \text{ even}, n > \frac{fsr_{ARM}}{fsr_{RC}} \tag{22}$$

and the frequency of the SCSB relative to the SC is

$$\Delta\nu_{SCSB} \equiv f_{SCSB} = 2f_0, 4f_0, 6f_0, \ldots \tag{23}$$

The second pair of sidebands on the SC, the SCNR, do not couple into the interferometer at all and are often referred to as the non-resonant sidebands. They are chosen to have a minimal overlap with both longitudinal and transverse modes of the recycling cavity to ensure low coupling into the interferometer.

The above results, including the factors that constrain the choice of frequencies, are summarized in Table 2.3:

FREQUENCY	PHYSICAL OR TECHNICAL CONSTRAINTS	SELECTION CRITERIA
Carrier at $\Delta\nu = 0$	None	(i) Must resonate in both recycling and arm cavities (ii) Minimum carrier light must exit the antisymmetric port
Half free spectral range of recycling cavity, f_0	(i) Should not exceed 20 MHZ, since carrier sideband could be at $3f_0$ (ii) Avoid modulation frequencies greater than 60 MHz	(i) Depends only on the length of the recycling cavity, given by $f_0 = c/4l_{RC}$.

Table 2.3: Modulation frequencies.

FREQUENCY	PHYSICAL OR TECHNICAL CONSTRAINTS	SELECTION CRITERIA
Frequency shifted subcarrier at $\Delta\nu_{SC} = nf_0$	Constrained by center frequency of commercially available acousto-optic modulators[a]	(i) Must resonate in recycling cavity, i.e., $\Delta\nu = nf_0$, where $n = fsr_{ARM}/fsr_{RC}$ and n even (ii) Must be anti-resonant in the arm cavities (iii)Minimum subcarrier light must exit the antisymmetric port
Carrier sideband at $\Delta\nu_{CSB} = f_0$ or $3f_0$	(i) Modulate at frequencies greater than 5 MHz, else the laser is not shot noise limited (ii) Avoid exceeding 60 MHz modulation frequencies (iii)Avoid using f_0 since the J_2 modulation term coincides with the subcarrier sideband at $2f_0$	(i) Must resonate in recycling cavity while experiencing a π phase shift relative to the carrier due to the arm cavity resonance, i.e., $\Delta\nu_{CSB} = f_0, 3f_0, 5f_0, \ldots$
Subcarrier resonant sideband at $\Delta\nu_{SCSB} = 2f_0$	(i) Choose frequencies between 5 and 60 MHz	(i) Must resonate in recycling cavity, i.e. $\Delta\nu_{SCSB} = 2f_0, 4f_0, \ldots$
Subcarrier non-resonant sideband at $\Delta\nu_{SCNR}$	(i) Choose frequencies between 5 and 60 MHz.	(i) Avoid overlap with longitudinal resonances and lower-order transverse modes of the recycling cavity to minimize coupling into the interferometer.

Table 2.3: Modulation frequencies.

a. This is only true for the FMI experiment. For LIGO, the subcarrier frequency shift can be arbitrarily large, since it is generated by frequency locking an auxiliary laser to the master oscillator.

2.3.2 Interferometer lengths

All the modulation frequencies depend on f_0, which, in turn, depends only on l_{RC}. The frequency shift of the SC relative to the carrier depends on L_l (see eqn. (17)). Thus, l_{RC} and L_l are chosen to give a useful set of modulation frequencies. Furthermore, once the mirror radii of curvature are fixed, the lengths of the cavities must be determined simultaneously so that the fundamental modes of the cavities are matched.

The asymmetry is determined by the requirement that the antisymmetric port is dark for the subcarrier. To minimize phase noise on the photodetectors, we reduce carrier losses, which imposes the requirement that no carrier light exit the antisymmetric port. The same argument applies to the SC, so we minimize both the C and SC power at the antisymmetric port. If the Michelson is held on the dark fringe for C, then the antisymmetric port is dark for the SC provided the Michelson has an asymmetry such that the difference in the lengths of the inline and perpendicular Michelson arms is given by

$$l_1 - l_2 = \frac{c}{2f_{SC}} \tag{24}$$

where c is the speed of light and f_{SC} is the subcarrier frequency shift relative to the carrier. Criteria for selection of interferometer lengths are summarized in Table 2.4:

LENGTH	PHYSICAL OR TECHNICAL CONSTRAINTS	SELECTION CRITERIA
Recycling cavity length, l_{RC}	(i) Cannot exceed 6.0 m else will not fit on optical table without a third fold.	(i) Determined along with arm cavity length, L_1, by the mirror radii of curvature and constraints on f_0.
Arm cavity length, L_1	(i) Cannot be shorter than 0.15 m nor longer than 1 m due to spatial considerations.	(i) Determined simultaneously with l_{RC} once mirror radii of curvature are chosen.
Asymmetry, a	(i) Tolerance to mismatch under 1%.	(i) Dark port condition for SC with frequency of a few 100 MHz (for LIGO, optimized for maximum gravitational wave sensitivity.

Table 2.4: Interferometer lengths.

2.3.3 Mirror radii of curvature

The mirror radii of curvature, along with the cavity lengths, influence the characteristics of the fundamental gaussian mode of the cavity, the transverse mode spacing and the condition for a stable resonator. For a cavity of length l and one flat mirror and one curved mirror with radius of curvature R, the waist of the TEM_{00} gaussian mode is given by

$$w_0^2 = \frac{\lambda}{\pi}\sqrt{(R-l)l} \tag{25}$$

the transverse mode spacing for the cavity is

$$\Delta\nu_{trans} = \frac{c}{l}cos^{-1}\left(\sqrt{1-\frac{l}{R}}\right) \tag{26}$$

and the condition for the resonator to be stable is

$$\frac{l}{R} < 1 \tag{27}$$

To ensure that the modulation frequencies that resonate in the recycling cavity do not excite higher order transverse modes of the cavity, we require that there be minimal geometric overlap between the higher-order transverse modes (up to fifth order, since we aperture larger modes) and any of the modulation fields. In other words, we avoid coincidences in the frequencies of the higher-order modes with the modulation sidebands. Since the lengths of the cavities directly impact the modulation frequencies (whose values are constrained, as listed in Table 2.3), it is by varying the mirror radii of curvature that we achieve optimum spacing for the higher-order transverse modes. Table 2.5 summarizes the selection criteria for the mirror radii of curvature.

MIRROR RADIUS OF CURVATURE	PHYSICAL OR TECHNICAL CONSTRAINTS	SELECTION CRITERIA
Arm cavity end mirror, Rad_{ETM}	(i) Super-polished mirrors, subject to availability of tooling at LIGO vendor	(i) Effects transverse mode spacing, i.e., chosen so transverse modes do not coincide with longitudinal resonances of the cavity (ii) must be greater than the length of the cavity to satisfy the stable resonator condition
Arm cavity input mirror, Rad_{ITM}	(i) Also super-polished mirrors (see above)	(i) Chosen to be flat, but could be curved, in which case the curvature of the ITMs could compensate mode mismatch due to asymmetry
Recycling mirror, Rad_{RM}	(i) Commercial mirror (e.g., CVI Corp.), so we try to use stock curvatures, typically available in integral increments of 1 m	(i) Simultaneously match the fundamental mode of the arm cavity and keep $l_{RC} < 6.0$ m (ii) satisfy the stable resonator condition (iii)avoid overlap of transverse modes of both cavities (iv)to avoid diffraction losses due to finite aperture on mirrors, the spot size on the recycling mirror, $w_{RM} < 1.5$ mm

Table 2.5: Mirror radii of curvature.

2.3.4 Mirror reflectivities

The storage time and, therefore, the frequency response of a Fabry-Perot cavity depends on its finesse. The cavity has finesse

$$F = \frac{\pi\sqrt{r_1 r_2}}{1 - r_1 r_2} \tag{28}$$

and storage time

$$\tau_s = \frac{l}{c}\frac{r_1 r_2}{(1 - r_1 r_2)} \tag{29}$$

The amplitude of the transfer function of the gravity wave strain, h, to the phase of the reflected light is

$$\left|\frac{d\phi_r}{dh}\right| = \frac{4\omega_0 \tau_s}{\sqrt{1 + 2\omega_g \tau_s}} \tag{30}$$

where ω_0 and ω_g are the frequencies of the laser light and the gravitational wave, respectively. The cavity pole occurs at $f_p = 1/4\pi\tau_s$, and for LIGO we choose $r_1^2 = 0.97$ and $r_2^2 = 1 - 10^{-4}$ to give storage time $\tau_s = 0.9$ msec or $f_p = 90$ Hz and, accordingly, a finesse of $F \approx 200$. The rear mirror reflectivity, r_2, is chosen to be as close to unity as possible to minimize losses. For the FMI, this choice of r_1, r_2 and length $l = 0.575$ m corresponds to a much shorter storage time, $\tau_s = 125$ nsec, but a LIGO-like finesse of 200.

The reflectivity of the recycling mirror is chosen so that the carrier light reflected from the interferometer is minimized, which leads to maximum build up of power in the recycling cavity. This is achieved by returning all the carrier light coming back at the laser from the symmetric side of the beamsplitter to the interferometer. From eqn. (9), the amplitude reflectivity for a resonant cavity is

$$r_{cav} = \frac{r_1 - r_2}{1 - r_1 r_2} \tag{31}$$

When $r_1 = r_2$, then $r_{cav} = 0$. If we treat the arm cavity as a compound rear mirror, with $r_{cav}^{ARM} \equiv r_2^{RC} = \sqrt{0.97}$, we find that $r_1^{RC} = r_2^{RC} = \sqrt{0.97}$ is the recycling mirror reflectivity that critically matches the carrier losses due to the arm cavity resonance. Since mirror reflectivities degrade with time, and since r_{cav} increases more rapidly for $r_1 > r_{crit}$ than for $r_1 < r_{crit}$, we choose $R_{RC} \equiv (r_1^{RC})^2 = 0.95$. These results are summarized in Table 2.6:

MIRROR REFLECTIVITIES	PHYSICAL OR TECHNICAL CONSTRAINTS	SELECTION CRITERIA
Arm cavity end mirror, R_{ETM}	(i) Super-polished mirrors, specially coated at REO (LIGO vendor), subject to availability from LIGO standard inventory	(i) High reflection, $T = 10^{-4}$ (ii) Low loss, $A = 10^{-4}$
Arm cavity input mirror, R_{ITM}	(i) Same as above	(i) Chose $T = 0.0028$ and $A = 10^{-4}$ to give ~3% reflection loss from the arm cavity on resonance
Recycling mirror, R_{RM}	(i) Commercial mirror (e.g., CVI Corp.), typically available in stock reflectivities of integral increments of 5%	(i) In principle, critically couple the carrier, i.e., transmission of the RM is equal to the reflection losses from the arm cavity on resonance. In actuality, choose a commercial reflectivity such that $T_{RM} > T_{crit}$ to allow for mirror degradation.

Table 2.6: Mirror reflectivities.

2.3.5 Proposed configuration for the FMI

Based on the selection criteria and the constraints discussed in the previous section, the design parameters listed in Table 2.7 yield an optimal design for the FMI. For comparison, the experimentally measured values of the parameters are also shown. They are fairly close to the design specifications with one significant difference: a pellicle pick-off plate is inserted between the recycling mirror and beamsplitter to probe the field in the recycling cavity, which we treat as 5.5% loss on the RM.

PARAMETER	DESIGN	EXPERIMENT
MODULATION FREQUENCIES	λ_C = 514.5 nm f_{CSB} = 58.5 MHz f_{SC} = 391 MHz f_{SCSB} = 39.0 MHz f_{SCNR} = 32.0 MHz	λ_C = 514.5 nm f_{CSB} = 58.71 MHz f_{SC} = 391.6 MHz f_{SCSB} = 39.16 MHz f_{SCNR} = 32.33 MHz
INTERFEROMETER LENGTHS	l_{RC} = 3.84 m L_{ARM} = 0.575 m a = 0.384 m	l_{RC} = 3.83 m L_{ARM} = 0.575 m a = 0.383 m
MIRROR RADII OF CURVATURE	Rad_{RM} = 6.0 m Rad_{ITM} = ∞ Rad_{ETM} = 15.0 m	Rad_{RM} = 6.0 m Rad_{ITM} = ∞ Rad_{ETM} = 15.0 m
MIRROR REFLECTIVITIES	R_{RM} = 0.90 R_{ITM} = 0.97 R_{ETM} = $1 - 10^{-6}$	R_{RM} = 0.93 R_{ITM} = 0.97 R_{ETM} = $1 - 10^{-6}$
MIRROR LOSSES	L_{RM} = 0.001 L_{ITM1} = 100×10^{-6} L_{ITM2} = 100×10^{-6} L_{ETM1} = 100×10^{-6} L_{ETM2} = 100×10^{-6}	L_{RM} = 0.055 L_{ITM1} = 67×10^{-6} L_{ITM2} = 37×10^{-6} L_{ETM1} = 100×10^{-6} L_{ETM2} = 100×10^{-6}

Table 2.7: Design parameters for the FMI and their experimental realization.

2.3.6 Length sensitivity matrix

For the configuration described above, the length sensing matrix, L (see eqn. (16)), is highlighted in Table 2.8 below:

DETECTION PORT	RF PHASE	l_C	l_D	L_C	L_D
Reflection, SCNR	I	**-770**	10^{-1}	-6	10^{-3}
Dark port, SCSB	Q	10^{-7}	**-132**	10^{-7}	-1
Reflection, CSB	I	-247	-7	**-27500**	-10^{-1}
Dark port, CSB	Q	10^{-10}	-100	10^{-9}	**-13250**

Table 2.8: Length sensitivity matrix (in units of wavelength) for the FMI, using *design* parameters.

It is remarkably diagonal with the largest off-diagonal terms a comfortable factor of 100 smaller than the diagonal terms.

In Fig. 2.7 we plot the amplitude of the fields inside the recycling cavity and the arm cavity, the field at the antisymmetric port and the field reflected from the whole interferometer as a function of frequency. The horizontal axis is in terms of the dimensionless quantity $m = f/f_0$. The carrier is located at $m = 0$, the CSB could be at $m = \pm 1, \pm 3, \pm 5$, the SC is at $m = 20$, and the SCSB are at $m = 20 \pm 2, 20 \pm 4$. The SCNR are ideally in the valleys, at $m = 20 \pm 1, 20 \pm 3$, so that they do no couple into the interferometer.

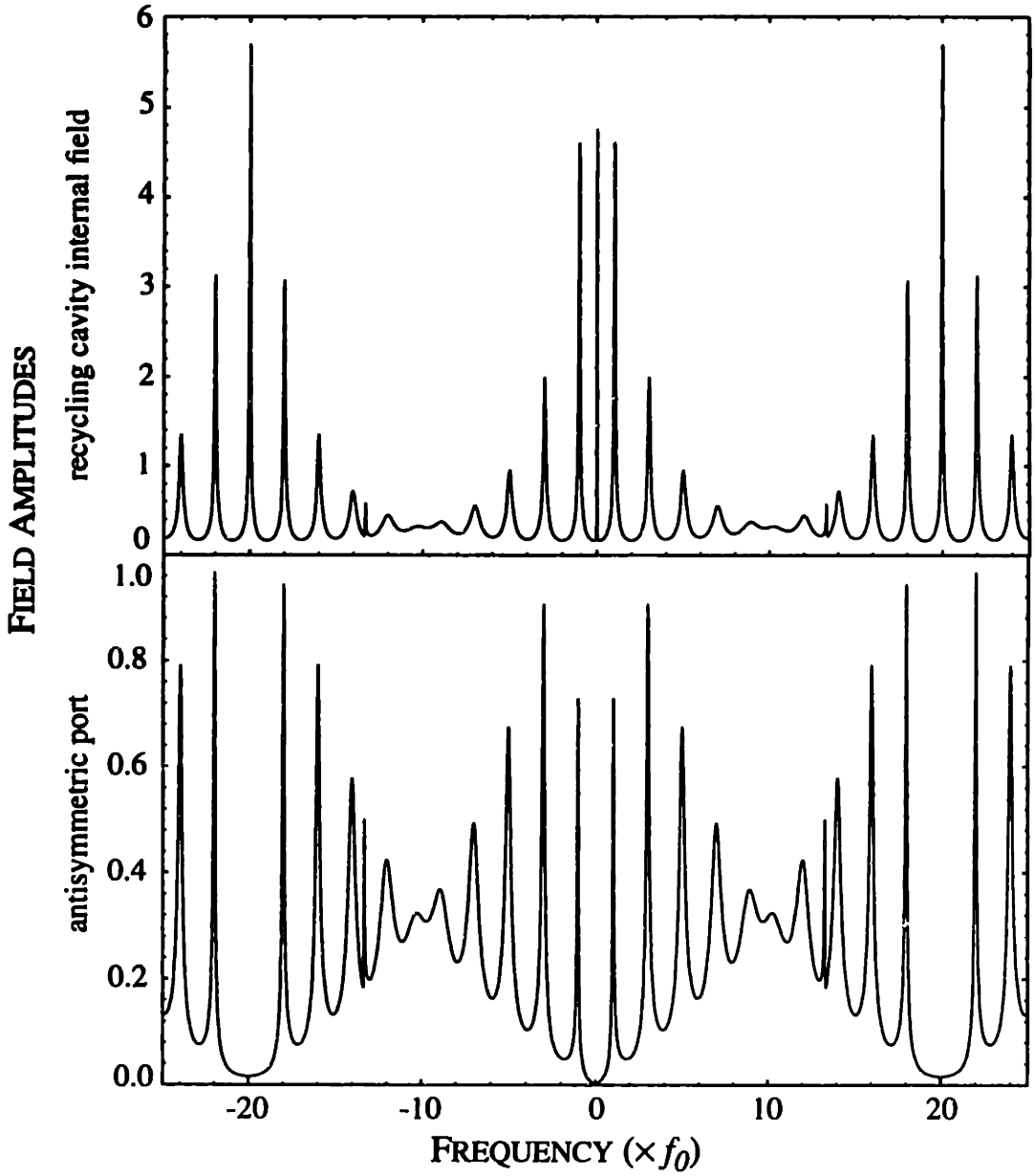

Figure 2.7: Amplitude of the fields in the recycling cavity (upper) and at the antisymmetric port (lower) for 1 W of input power as a function of frequency (in units of f_0, the half free spectral range of the cavity) when the interferometer in resonant for the carrier. The carrier double resonance occurs at $f = 0$.

2.4 The alignment sensing scheme

The general concept of using the transverse (off-axis) modes of an optical resonator to detect misalignment and mismatch was proposed by Anderson [23]. Variations of this idea in conjunction with phase sensitive detection have been proposed and experimentally demonstrated for simple two mirror resonators [24], [12]. Specifically, Morrison *et al.* [12] use a variant of the Pound-Drever-Hall reflection-locking technique (see Section 2.2) for alignment sensing. This is particularly advantageous since light which is already circulating in the interferometer is used to sense both longitudinal and transverse degrees of freedom, which also ensures that the interferometer is aligned relative to the input light beam. Morrison *et al.* investigated a flat-curved Fabry-Perot cavity, where they showed that for an infinitely long cavity an angular misalignment of the flat input cavity mirror produces an alignment signal in the near field of the light reflected from the input mirror. Similarly, a misalignment of the rear curved mirror produces a signal in the far field.

In this section we present an intuitive, geometrical picture of misalignment in optical cavities and a detection scheme based on the reflection-locking technique of Section 2.2. A mathematical formalism for applying this technique to a general distorted or misaligned optical system is developed in Chapter 3.

2.4.1 Misalignment and higher-order modes

In this section we consider two kinds of misalignment of optical beams: first, beams whose optical axes are laterally shifted with respect to each other, and, second, beams with tilted axes. We show that in both cases misalignment excites higher-order modes of the propagating beam, as presented by Morrison *et al.* [12].

In the paraxial approximation, the solutions to the scalar wave equation in one dimension can be expressed as a superposition of Hermite-Gaussian modes [25]. The field distribution is given by:

$$U_m(x,z) = \left(\frac{2}{\pi}\right)^{1/4}\left(\frac{1}{2^m m! w(z)}\right)^{1/2} H_m\left(\frac{\sqrt{2}x}{w(z)}\right) \exp\left(-x^2\left(\frac{1}{w(z)^2}+\frac{ik}{2R(z)}\right)\right)\exp\left(i\left(m+\frac{1}{2}\right)\eta(z)\right)\exp(-ikz) \tag{32}$$

where the z-axis points in the beam propagation direction and where $\eta(z)$, $w(z)$ and $R(z)$ are the mode-dependent Guoy phase shift, the spot size and the curvature of the phase front at position z, respectively,

$$\eta(z) = tan^{-1}\left(\frac{z}{z_0}\right), \quad w(z) = w_0\sqrt{1+\left(\frac{z}{z_0}\right)^2} \quad \text{and} \quad R(z) = z + \frac{z_0^2}{z} \tag{33}$$

and the Rayleigh length, z_0, is given by $z_0 = \pi w_0^2/\lambda$ with w_0 the waist size. $H_m(x)$ is the Hermite polynomial of order m. At the plane $z = 0$, the spatial distributions of the fundamental and first two higher-order modes are

$$U_0(x) = \left(\frac{2}{\pi}\right)^{1/4}\left(\frac{1}{w_0}\right)^{1/2} exp\left(\frac{-x^2}{w_0^2}\right) \tag{34}$$

$$U_1(x) = \left(\frac{2}{\pi}\right)^{1/4}\left(\frac{1}{w_0}\right)^{1/2}\left(\frac{2x}{w_0}\right)exp\left(\frac{-x^2}{w_0^2}\right) \tag{35}$$

$$U_2(x) = \left(\frac{2}{\pi}\right)^{1/4}\left(\frac{1}{w_0}\right)^{1/2}\left(\sqrt{8}\left(\frac{x}{w_0}\right)^2 - 1\right)exp\left(\frac{-x^2}{w_0^2}\right) \tag{36}$$

These relations will be useful in deriving the spatial distributions of interfering beams which are misaligned with respect to each other.

Consider two perfectly interfering Hermite-Gaussian beams propagating in the positive z-direction with electric fields given by:

$$\begin{aligned} E_1 &= A_1 exp\left(\frac{-x^2}{w_0^2}\right)exp(-ikz) \\ E_2 &= A_2 exp\left(\frac{-x^2}{w_0^2}\right)exp(-ikz) \end{aligned} \tag{37}$$

When E_2 is laterally displaced in the positive x-direction by a small amount, x_0, we get

$$E_2 = A_2 exp\left(\frac{-(x-x_0)^2}{w_0^2}\right)exp(-ikz) \tag{38}$$

which can be expanded to second-order in x_0 to give

$$E_2 \approx A_2 exp\left(\frac{-x^2}{w_0^2}\right)\left(1-\left(\frac{x_0}{w_0}\right)\left(\frac{x}{w_0}\right)+\left(\frac{x_0}{w_0}\right)^2\left(\frac{1}{2}\left(\frac{x}{w_0}\right)^2-1\right)\right)exp(-ikz)$$
$$\approx A_2\left(\left(1-\left(\frac{x_0}{w_0}\right)^2\left(1-\frac{\sqrt{2}}{16}\right)\right)U_0-\frac{1}{2}\left(\frac{x_0}{w_0}\right)U_1-\frac{\sqrt{2}}{16}\left(\frac{x_0}{w_0}\right)^2U_2\right) \quad (39)$$

Similarly, if E_2 is tilted by a small angle θ with respect to E_1, then we get

$$E_2 = A_2 exp\left(\frac{-x^2}{w_0^2}\right)exp(-2ik\theta x)exp(-ikz) \quad (40)$$

which, to second-order in x_0 , gives

$$E_2 \approx A_2 exp\left(\frac{-x^2}{w_0^2}\right)\left(1-i\left(\frac{\theta}{\theta_D}\right)\left(\frac{x}{w_0}\right)+\frac{1}{2}\left(\frac{\theta}{\theta_D}\right)^2\left(\frac{x}{w_0}\right)^2\right)exp(-ikz)$$
$$\approx A_2\left(\left(1-\left(\frac{\theta}{\theta_D}\right)^2\left(1-\frac{\sqrt{2}}{16}\right)\right)U_0-\frac{i}{2}\left(\frac{\theta}{\theta_D}\right)U_1-\frac{\sqrt{2}}{16}\left(\frac{\theta}{\theta_D}\right)^2U_2\right) \quad (41)$$

where $\theta_D = \lambda/(\pi w_0)$ is the divergence or Rayleigh angle of the Hermite-gaussian beam. In both eqns. (39) and (41) we see that the amplitude of the TEM_{10} mode (the U_1 terms) is proportional to the normalized shift or tilt. The next higher-order term in the expansion of U_1 is $(x_0/w_0)^3$ or $(\theta/\theta_D)^3$. A significant distinction between the shift and tilt is the quadrature phase associated with the U_1 term in eqn. (41).

2.4.2 A heterodyne technique for alignment sensing

The heterodyne detection technique of Section 2.2.1 can be extended to spatial sensing of the wavefront [12] (see Fig. 2.8). If one of the mirrors of a resonant optical system is misaligned, higher-order transverse modes are excited. As shown in eqns. (37) and (39), a small misalignment about the y-axis excites TEM_{10} mode to first order in the misalignment angle. In the suppressed carrier technique of Section 2.2.1, the beat between the carrier leaking out of the interferometer due to deviation from resonance and the promptly reflected RF sidebands is used to detect purely longitudinal deviations. In the presence of angular misalignments, the carrier field leaking out of the interferometer has a TEM_{10} spatial component (which is not necessarily resonant in the interferometer). The magnitude of the TEM_{10} mode can be measured by detecting the spatial gradients in the interfering carrier and sideband fields. A segmented photodetector which is split along the

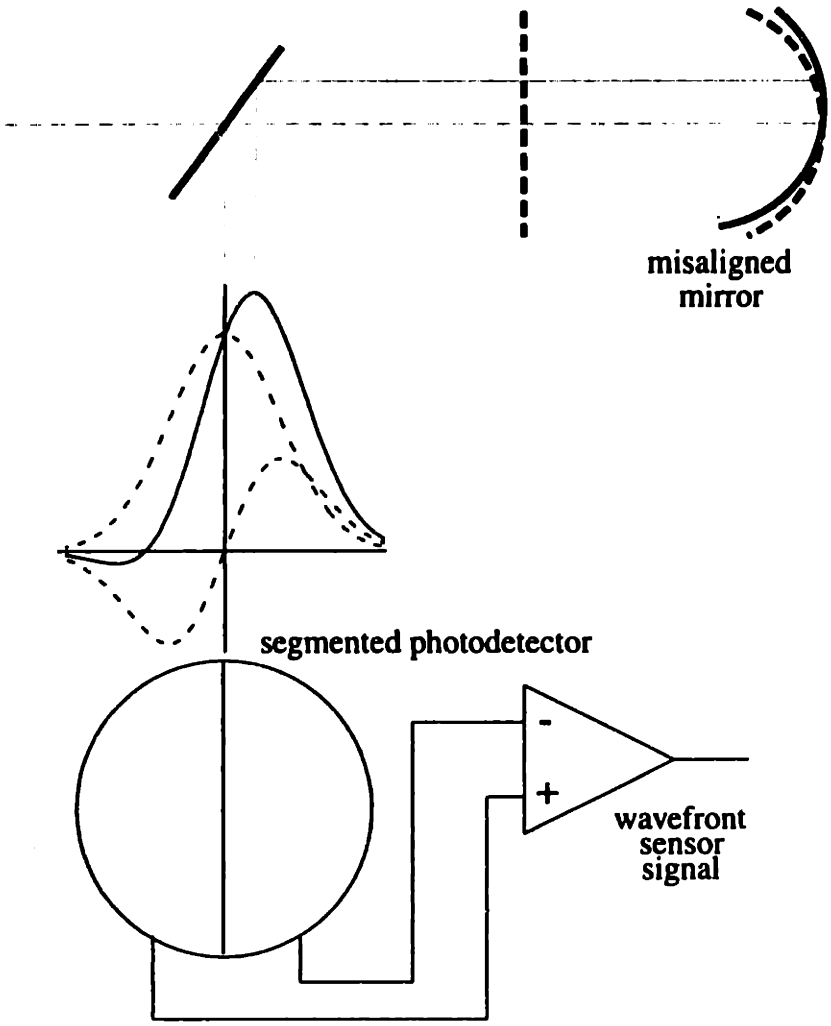

Figure 2.8: Wavefront sensing for a simple Fabry-Perot interferometer. To first order, the spatial mode in the presence of misalignment (solid curve) is a linear superposition of the TEM_{00} and TEM_{10} modes of the cavity (dashed curves).

y-axis and where the signals from the two half-planes are subtracted from each other, is most sensitive to this spatial interference and at the same time rejects any signal coming from longitudinal deviations.

This method of heterodyne sensing of misalignment is called *wavefront sensing*, since it is spatial distortion of the wavefront which is used to probe angular misalignment. In an optical cavity, to first order, a misalignment of the optic axis of the cavity with respect to the phase modulated incident beam will excite higher-order modes of the cavity. Since the wavefront is sensed by differencing the signals on opposite segments of a split

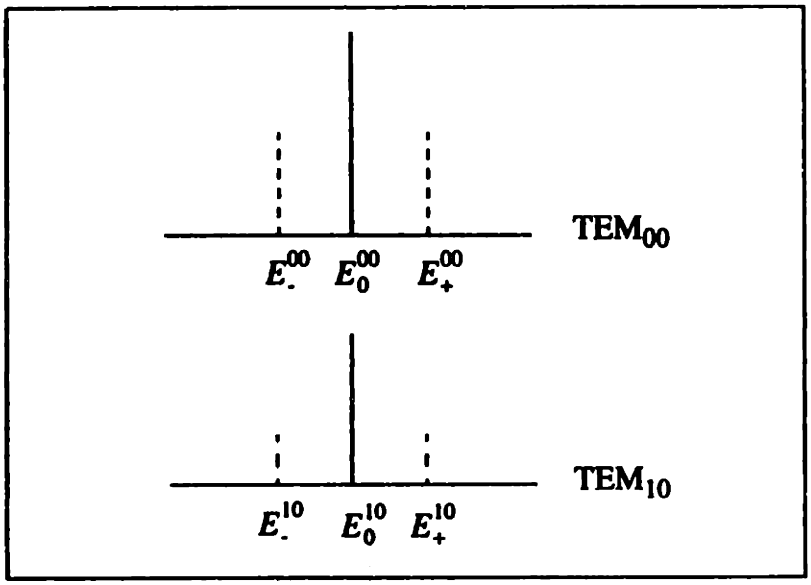

Figure 2.9: Spectrum of the field on the photodetector in the presence of misalignment. The carrier (solid) and the phase modulation sidebands (dashed) are shown for both the TEM_{00} and TEM_{10} modes, respectively.

photodetector, the TEM_{00} (even) will have a non-zero overlap with the TEM_{10} (odd) mode. Further, only terms with a frequency difference of Ω will be down-converted by the demodulator. As a result, the demodulated wavefront sensor signal is due to the beat between the TEM_{00} component of the field at the carrier frequency and the TEM_{10} component at the RF frequency superposed with the TEM_{10} component at the carrier frequency beating against the TEM_{00} component at the sideband frequency.

Following the notation in Fig. 2.9, the signal on the split photodetector is

$$\begin{aligned} i = {} & [(E_0^{00*}E_0^{10} + E_+^{00*}E_+^{10} + E_-^{00*}E_-^{10}) + \mathrm{CC}] + \\ & [(E_0^{00*}E_+^{10} + E_-^{00*}E_0^{10} + E_+^{00}E_0^{10*} + E_0^{00}E_-^{10*})\,exp(i\Omega t + \eta) + \mathrm{CC}] + \\ & [(E_+^{00}E_-^{10*} + E_-^{00*}E_+^{10})\,exp(2i\Omega t + \eta) + \mathrm{CC}] \end{aligned} \tag{42}$$

and the in- and quadrature-phase demodulator signals, respectively, are

$$v_I = Re\{(E_0^{00*}E_+^{10} + E_-^{00*}E_0^{10} + E_+^{00}E_0^{10*} + E_0^{00}E_-^{10*})\,exp(i\eta)\} \tag{43}$$

$$v_Q = Im\{(E_0^{00*}E_+^{10} + E_-^{00*}E_0^{10} + E_+^{00}E_0^{10*} + E_0^{00}E_-^{10*})\,exp(i\eta)\} \tag{44}$$

Note that the above expressions are completely analogous to eqns. (12), (13) and (14). From eqn. (32), we see that each higher-order mode, $TEM_{m,n}$, has a different Guoy phase

shift, $\phi_{m,n} = (m+n+1)\eta(z)$, which implies that each higher-order mode picks up a different phase shift as it propagates through a distance, z. This phase shift is crucial for distinguishing signals due to misalignments of longitudinally separated optical components and is discussed in the following section.

2.4.3 Distinguishing misalignment of various optical components

Since the different order modes propagate with different Guoy phases, the detected modulation depth also depends on the distance between the photodetector and the cavity or interferometer output. Higher-order modes generated by tilted optical elements which have a longitudinal separation — the input and rear mirrors of a cavity, for example — have to travel different distances to the photodetector and can thus be distinguished by using two segmented photodetectors at two different locations. For a non-degenerate cavity of length l, it turns out that two detectors in reflection separated by a phase shift $\eta(l)$ will each be maximally sensitive to the rear or input mirror, respectively. Consequently, the amplitude of the misalignment signals depends on the Guoy phase difference of the interfering TEM_{00} and TEM_{10} modes; the *Guoy phase telescopes* play an important role in the wavefront sensing scheme to determine the origin of the misalignment.

Guoy phase telescopes get their name from conventional telescopes, namely, a set of lenses that transforms the geometric characteristics of a light beam, or, equivalently, projects the beam at a different plane. We have two constraints on the Gaussian beam at the detection plane, first, that its Guoy phase be optimized for maximum detection of the primary degree of freedom, and second, that the spot size be about 1 mm. A smaller spot size implies greater sensitivity to centering errors, whereas a larger spot size is apertured by the photodiode. Guoy phase accumulation goes as $tan^{-1}(z/z_0)$, so, in principle, we could simply propagate a beam with given z_0 to different distances to accumulate different Guoy phase shifts. This is, however, impractical. For the FMI $z_0 = 2.88$ m, so to acquire 90° of phase shift the beam must propagate to a distance $z_0 = \infty$. Furthermore, mere propagation allows little control of the spot size at the detector position. Since a TEM_{00} Hermite-Gaussian mode acquires 180° of phase shift as it goes through the focal plane of a lens, and lenses can, of course, be used to adjust the magnification of the spot, telescopes are used to set the Guoy phase and spot size at the detector.

The Gaussian beam at the output port of the interferometer is specified by a state vector

$$\begin{bmatrix} R(z_{port}) \\ w(z_{port}) \\ \eta(z_{port}) \end{bmatrix} \tag{45}$$

where $R(z_{port})$, $w(z_{port})$ and $\eta(z_{port})$ are the phasefront curvature, the spot size and the accumulated Guoy phase shift, respectively. This state vector is then propagated through a a series of lenses and propagation distances to give the desired state vector at the wavefront detector position. The transformation through a lens of focal length f is

$$\begin{bmatrix} R(z) \\ w(z) \\ \eta(z) \end{bmatrix} \xrightarrow{\text{lens of focal length } f} \begin{bmatrix} Rf/(f-K) \\ w \\ \eta \end{bmatrix} \tag{46}$$

and for free space propagation through a distance d:

$$\begin{bmatrix} R(z) \\ w(z) \\ \eta(z) \end{bmatrix} \xrightarrow{\text{propagation distance } d} \begin{bmatrix} (z'+d)\left(1+\left(\frac{z_0'}{z'+d}\right)^2\right) \\ w_0'\sqrt{1+\left(\frac{z'+d}{z_0'}\right)^2} \\ \eta + tan^{-1}\left(\frac{z'+d}{z_0'}\right) - tan^{-1}\left(\frac{z'}{z_0'}\right) \end{bmatrix} \tag{47}$$

where

$$w_0' = \frac{\lambda w R}{\lambda^2 R^2 + \pi^2 w^4} \tag{48}$$

is the beam waist of a Gaussian beam which has curvature R, spot size w and Guoy phase η at position, z, of the initial state vector, and

$$z' = \frac{\pi w^4 R}{\lambda^2 R^2 + \pi^2 w^4} \tag{49}$$

is the position of the beam waist from z and $z_0' = \pi w_0'^2/\lambda$. In our convention, $z' > 0$ if the beam waist is to the left (decreasing z) of z. Operating on the state vector at the

interferometer port with a cascaded series of transformations, we find the focal lengths and positions of the lenses which give the required state vector at the detector.

2.4.4 A complete wavefront sensing scheme

Having developed the wavefront sensing scheme for a Fabry-Perot interferometer, we now extend this detection technique to the full interferometer, much the same as the extension of the longitudinal sensing scheme in Section 2.2. Analogous to eqn. (16), we define the alignment sensitivity matrix such that

$$WFS_i(t, \eta, \Theta) = 2J_0(\Gamma)J_1(\Gamma)P_i\sum_j A_{ij}\Theta_j cos(\eta - \eta_{ij})cos(\Omega t + \phi_{ij}) \tag{50}$$

where WFS_i is the wavefront sensor signal at the i-th port; Θ_j is the (normalized per divergence angle) misalignment angle for the j-th degree of freedom; A_{ij} is the alignment sensitivity matrix; η is the Guoy phase shift to the detector; η_{ij} and ϕ_{ij} are the intrinsic Guoy and RF phases, respectively; P_i is the power on the detector; and Ω and Γ are the RF modulation frequency and depth, respectively.

INTERFERING FIELDS	DETECTION PORT	MISALIGNED OPTIC(S)
WFS1: SC and SCNR	reflection (η_1)	RM
WFS2: SC and SCNR	reflection (η_2)	common ITMs
WFS3: SC and SCSB	antisymmetric	differential ITMs
WFS4: C and CSB	antisymmetric	differential ETMs
WFS5: C and CSB	reflection	common mode ETMs

Table 2.9: Signals most sensitive to angular degrees of freedom.

In Table 2.9, we list the interfering fields, the detection port and the primary angular degree of freedom to which they are sensitive. We detect the subcarrier non-resonant sideband signal at two different Guoy phase shifts to distinguish the common ITM misalignment from RM misalignment.

A very important aspect of the multi-dimensional heterodyne alignment sensing technique described here is that it uses the same phase modulated light as the longitudinal sensing system. In fact they share common features: predictably, differential misalignments and length deviations are detected at the antisymmetric port in the Q-phase,

while common degrees of freedom appear in the I-phase at the symmetric port; the subcarrier is anti-resonant in the arm cavities and therefore oblivious to the ETMs. Referring back to Fig. 2.6, this is summarized in Table 2.10.

DETECTOR	①	②	③	④	⑤	⑥
Length d.o.f.	l_C		l_D	L_D	L_C	
Angular d.o.f.	RM	ITM_C	ITM_D	ETM_D	ETM_C	

Table 2.10: Summary of signals for longitudinal and angular degrees of freedom (d.o.f.) using the multiple frequency modulation scheme.

Developing a mathematical algorithm to calculate the matrix elements of A and to design an optimal detection scheme for arbitrarily complex optical interferometers is the central focus of Chapter 3.

Chapter 3

Theory of mode decomposition

In this chapter, we present a formalism which can be used to study the problem of misalignment in the LIGO interferometer, with the goal of characterizing the sensitivity of the interferometer to angular misalignment and designing a dynamic scheme for maintaining alignment [13].

The general concept of using the transverse (off-axis) modes of an optical resonator to detect misalignment is explained in Section 2.4. Here we extend this concept by developing a formalism to analyze more complex optical systems comprised of arbitrarily complicated arrangements of optical elements. In particular, it can be applied to systems consisting of cavities placed inside other cavities. The field circulating in the misaligned or distorted optical system is decomposed into a superposition of the eigenmodes of the unperturbed system; the scale of the imperfections or misalignments determines the number of eigenmodes needed for an accurate description. Misaligned or distorting optical components are represented as operators in the basis of these eigenmodes. This approach relies on analytical methods, which gives it tremendous advantage over currently used numerical methods, e.g., Fast Fourier Transform [26], [27], which are computationally demanding. The analytic methods were developed before the FFT codes and most of the conceptualization of mirror perturbations and misalignments was done analytically. For simplicity and tractability, we first apply our model to the ubiquitous Fabry-Perot cavity, and then build up more complex optical configurations by cascading additional optical elements. We thereby emphasize the generality of the model as an analytical tool for calculating field distortions in any complex optical system.

The formalism for calculating misalignment and distortion operators in the modal space is presented in the next section. In Section 3.3 we apply this formalism to derive the fields in a Fabry-Perot cavity and in more complex optical systems such as coupled cavities and a recycled Michelson interferometer configuration.

3.1 Formalism for mode decomposition

The x- and y- axes of the coordinate system are chosen to be transverse to the beam propagation (and optical axis) of the perfectly aligned and undistorted system (z-axis). Using the paraxial approximation [25] one can quite generally expand the electromagnetic field of a light beam as a superposition of orthonormal Gaussian modes in the form

$$E(x, y, z) = \sum a_{mn} U_{mn}(x, y, z) \tag{51}$$

where a_{mn} can be represented as a vector in the modal space. The $U_{mn}(x,y,z)$ are Gaussian modes, which may be Hermite-Gaussian functions (see examples in Section 3.3 and definitions in Appendix A). Our goal is to compute the eigenfunctions $U_{mn}(x,y,z)$ only once for the perfectly aligned and undistorted system and then treat any angular misalignment or distortion as a perturbation which transfers energy between transverse modes only. In other words, the perturbation can be expressed as a matrix operator acting on a complex vector space (the modal space), and the solutions to the paraxial wave equation of the misaligned or distorted system can be calculated through a perturbation series approach from the solutions of the unperturbed system.

If $M(x,y,z_2,z_1)$ is an operator which transforms the electromagnetic field of a *misaligned or distorted* optical system at position z_1 into a field at position z_2, that is

$$E'(x, y, z_2) = M(x, y, z_2, z_1) \otimes E(x, y, z_1) \tag{52}$$

its representation $M_{mn,kl}(z_2,z_1)$ in the modal space can be written as

$$M_{mn,kl}(z_2, z_1) = \int_{-\infty}^{\infty}\int U^{\dagger}_{mn}(x, y, z_2) M(x, y, z_2, z_1) U_{kl}(x, y, z_1)\, dx\, dy \tag{53}$$

where the functions $U_{mn}(x,y,z)$ are the eigenmodes of the *unperturbed* system.

An important simplification in calculating the modal space representation of these operators for a real physical system can be obtained by entirely separating the longitudinal propagation from misalignment and distortion effects caused by lenses and mirrors, which affect the wavefront at a fixed longitudinal position only.

Since the $U_{mn}(x, y, z)$ are the vacuum eigenmodes, the modal space representation of the propagation operator must be diagonal. In the Hermite-Gaussian basis, e.g., the propagator simplifies to

$$P_{mn,kl}(\eta) = \delta_{mk}\delta_{nl}\, e^{-ik(z_2 - z_1)} e^{i(m+n+1)\eta} \tag{54}$$

where $\eta = \eta(z_2) - \eta(z_1)$ is the Guoy phase shift between position z_2 and z_1 (see Appendix A). We have included all the rapid longitudinal (z-coordinate) variation in the propagator of the Gaussian beam. The propagator is the only operator which retains a significant z-dependence. Hence, for lenses and mirrors eqn. (53) reduces to

$$M_{mn,kl} = \langle mn|M(x, y)|kl\rangle \tag{55}$$

where the bra-ket product is defined as the integration over the transverse degrees of freedom and where $\langle mn|$ and $|kl\rangle$ are the Gaussian eigenmodes with all z-dependence due to propagation removed.

By calculating the modal space representation of both the propagation and the effects of misalignment, it is possible to calculate the eigenmodes of any misaligned or distorted configuration of the optical system by means of linear algebra only, without repeatedly solving the paraxial wave equation.

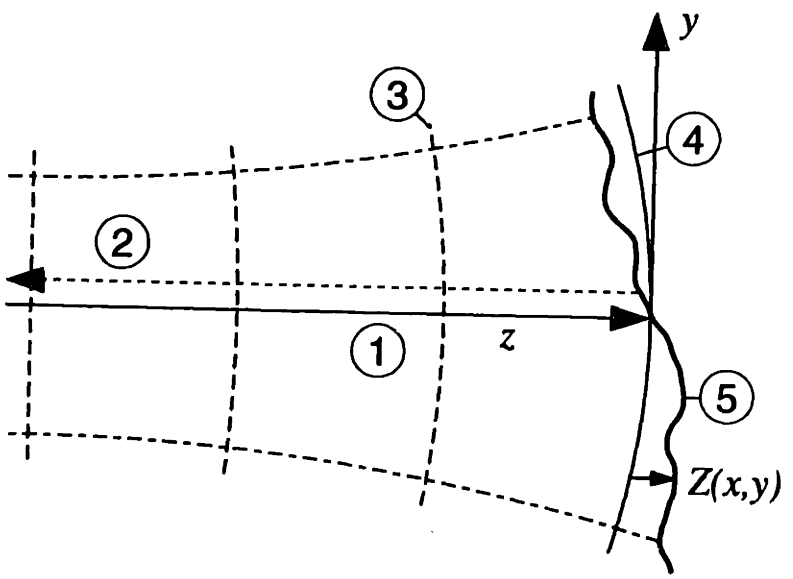

Figure 3.1: Reflection on an imperfect and misaligned mirror surface. ① direction of incoming laser beam, ② reflected beam, ③ undistorted wavefront, ④ ideal mirror surface, ⑤ physical mirror surface and $Z(x,y)$ deviation from ideal mirror surface.

Consider a slightly imperfect and slightly misaligned mirror[1] (see Fig. 3.1). Spatial

variations over the mirror surface cause each part of the wavefront which is incident at a lateral offset (x,y) to acquire an additional phase shift due to a local displacement in the z-direction. The parameters of the unperturbed Gaussian beam are matched to the ideal mirror surface and all deviations from the ideal surface are contained in the function $Z(x,y)$. The mirror distortion operator can then be written as[1]

$$M(x, y) = e^{-2ikZ(x, y)} \tag{56}$$

If $Z(x, y)$ is a real function, this operator is unitary and, thus, conserves energy[2]. The modal space representation then becomes [28]:

$$M_{mn, kl} = \langle mn|e^{-2ikZ(x, y)}|kl\rangle = \langle mn|exp\left(-2ik \sum_{op,qr} |op\rangle Z_{op,qr}\langle qr|\right)|kl\rangle \tag{57}$$

Since the transverse size of the Gaussian beam is fully described by the spot size, $w(z)$, which is simply a transverse scaling factor, the z-dependence of $Z_{op,qr}$ in eqn. (57) can be removed by the variable substitutions $x' = \sqrt{2}x/w(z)$ and $y' = \sqrt{2}y/w(z)$. Expanding $Z(x,y)$ in a series of orthonormal polynomials H_i (such as the Hermite or Laguerre polynomials) of the form

$$-2kZ(x, y) = \sum_{i, j} c_{ij} H_i(x') H_j(y') \tag{58a}$$

one obtains:

$$-2kZ_{op,qr} \equiv 2\sum_{i, j} c_{ij} T^{ij}_{op, qr} = \sum_{i, j} c_{ij}\langle op|H_i(x)H_j(y)|qr\rangle|_{z=0} \tag{58b}$$

The $T^{ij}_{op, qr}$ are Hermitian operators which serve as generators for the unitary transformation that describes the wavefront distortion. A detailed calculation of these generators in the Hermite-Gaussian basis is presented in Appendix A.

The physical meaning of the individual terms in the expansion of eqn. (58a) — using Hermite polynomials in the expansion — can be understood as follows: the constant term, c_{00}, corresponds to longitudinal displacements of the mirror; terms proportional in $H_1(x)$

---

1. The validity of this approximation is clarified later on.
1. Generally, one has to multiply the right hand side of eqn. (56) by the reflection coefficient to obtain the true reflected field of the mirror.
2. The distortion operator which describes reflection from the rear surface of the mirror is given by $\bar{M}(x, y) = exp(2ikZ(x, y)) = M^{\dagger}(x, y)$.

or $H_1(y)$ and, hence, linear in x or y correspond to yaw and pitch, respectively, where the coefficients c_{10} and c_{01} are proportional to the rotation angle; the term proportional to $H_2(x) + H_2(y)$ corresponds to a deviation in the curvature of the spherical phase front; a term proportional to $H_2(x) - H_2(y)$ depicts astigmatism; and so on.

For a small rotation about the y-axis $Z(x,y)$ can be written as $Z(x, y) = \theta_x x$. By substituting $\Theta_x = \theta_x \pi w(z)/\lambda$, which is the normalized rotation angle, the operator becomes:

$$-2kZ(x, y) = -\sqrt{8}\Theta_x \frac{\sqrt{2}x}{w(z)} = -\sqrt{2}\Theta_x H_1(x') \tag{59}$$

In the Hermite-Gaussian basis, the recursion relationship for the Hermite polynomials simplifies the generator T^{10} to

$$T^{10}_{op,qr} = \frac{1}{\sqrt{2}}\delta_{pr}(\sqrt{q}\,\delta_{o,q-1} + \sqrt{o}\,\delta_{o,q+1}) \tag{60}$$

The Hermite-Gaussian basis is particularly well-suited to describe small misalignments, as indicated by the simple form of eqn. (60). Notably, if the generator in eqn. (60) is applied to the fundamental TEM_{00} mode, the TEM_{10} is the only resulting mode. Any other higher-order mode which can be excited by a misaligned mirror is introduced by the matrix exponential of eqn. (57) only; in other words, they are not significant, if the normalized rotation angle is small compared to unity.

A similar problem is the distortion of the wavefront when it passes through an optical element such as a partially transmitting mirror or a lens. If the deviation in thickness of the optical element from its ideal shape is denoted by $d(x,y)$, then the phase distortion operator can be written as

$$M(x, y) = e^{-i(n-1)k\,d(x,y)} \tag{61}$$

where n is the refractive index of the optical medium. This operator is of the same form as the distortion operator in reflection with one exception: the linear term in $d(x,y)$ does not account for an angular tilt, but instead describes a wedge. In fact, an angularly misaligned optical element shifts the beam laterally. For a small tilt θ_x about the y-axis, the shift in the x-direction can be calculated using Snell's law:

$$\Delta(x) \approx \theta_x \left(1 - \frac{1}{n}\right) d \tag{62}$$

where n and d are the index of refraction and the thickness of the optical element, respectively. A detailed calculation of the lateral shift operator is presented in Appendix A.2.

With regard to optical cavities, tilting the partially transmitting input mirror of the cavity has two effects: first, the wavefront of the field inside the cavity is distorted by the tilt of the reflecting surface, and second, the incident beam is shifted laterally upon transmission through the input coupler. Comparing eqn. (62) with eqn. (59), the effect of lateral shift turns out to be much smaller, roughly by a factor of d/z_0, which is negligible for most practical cavity configurations.

3.2 Wavefront sensing in the modal space

In this section an expression for the demodulated signal is derived for a misaligned optical system in the modal space. If $O(\omega)$ is an operator which depicts an entire optical system and if the incoming laser beam consists of a carrier and a pair of phase modulation sidebands, for small modulation depths the field at the output of the system can be written as

$$E_{out} = E_0 + E_+ + E_- \tag{63}$$

$$E_0 = O(\omega_0) E_{inp} \quad \text{and} \quad E_\pm = \frac{\Gamma}{2} O(\omega_0 \pm \Delta\omega) E_{inp} \tag{64}$$

where ω_0 corresponds to the frequency of the carrier, $\Delta\omega$ is the modulation frequency, Γ is the modulation depth and E_{inp} is the incident field in the modal space (usually the fundamental mode). The carrier and the modulated fields can have spatial components.

The total light power on the photodetector which is placed at a distance η in Guoy phase away from the output of the optical system is

$$\bar{S} = [P(\eta) E_{out}]^\dagger D^\Omega [P(\eta) E_{out}] \tag{65}$$

where D^Ω is an operator that accounts for the physical dimensions of the photodetector and $P(\eta)$ is the propagator defined in eqn. (54). If $\bar{S}$ is demodulated with the modulation

frequency $\Delta\omega$, then only terms which have an $e^{-i\Delta\omega t}$ dependence on the modulation frequency remain in the down-converted signal:

$$S = (E_0)^\dagger P^\dagger(\eta) D^\Omega P(\eta) E_- + \frac{\varepsilon_0 c}{2}(E_+)^\dagger P^\dagger(\eta) D^\Omega P(\eta) E_0 \tag{66}$$

Here we adopt the convention that the real part of the down-converted signal denotes the I-phase while the imaginary part denotes the Q-phase.

In Appendix A.4, we calculate the demodulation operator D^Ω in the modal space for arbitrarily shaped detectors. From the form of the propagator (see eqn. (54)), it can be seen that the η dependence in S can be expressed in terms of a sine and cosine series:

$$S = \sum_{s=0}^{\infty} d_s cos(s\eta) + \sum_{s=0}^{\infty} e_s sin(s\eta) \tag{67}$$

where the coefficients d_s and e_s are complicated functions of the detector shape and the output fields. They are completely independent of the detector position if the ratio of the beam spot size over the detector diameter is held constant.

The above expansion is helpful in understanding the Guoy phase dependence of the demodulated signal. For instance, a single photodetector which covers the full cross-section of the beam has only one non-zero coefficient, d_0. Similarly, d_1 and e_1 are the only significant coefficients for small angular misalignments measured by a half-plane detector which is split along one axis.

3.3 Application to various interferometer configurations

In this section we develop the modal expressions for the fields in the various optical configurations shown in Fig. 3.2.

3.3.1 Fabry-Perot cavity

The mode decomposition technique is applied to calculate the alignment signals of a Fabry-Perot cavity (see Fig. 3.2(a)). The cavity round-trip propagation in matrix form reads:

$$P_{rt} = (-r_1)(-r_2) M_1 P M_2 P \tag{68}$$

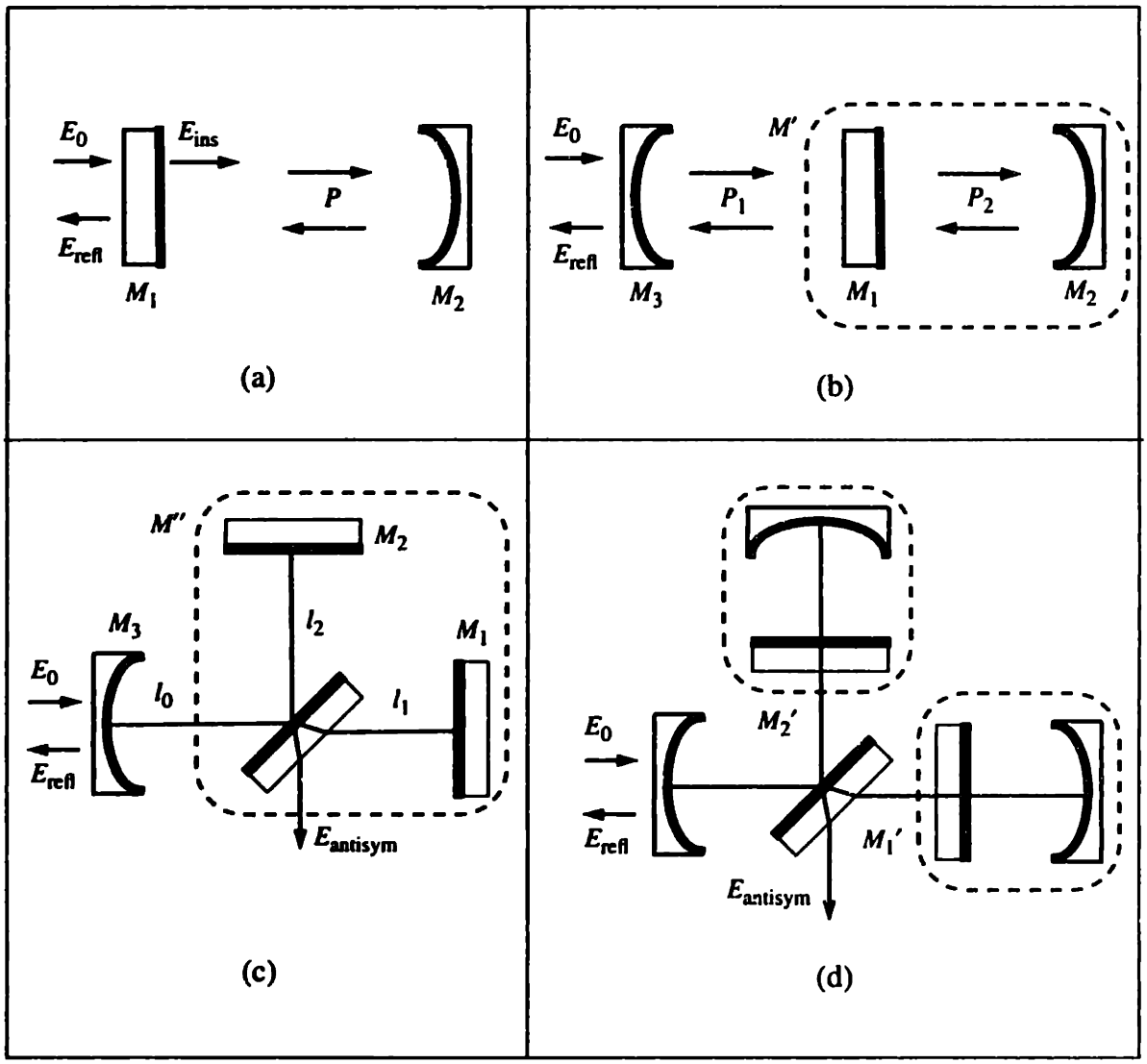

Figure 3.2: Setup of (a) a Fabry-Perot interferometer, (b) a coupled pair of cavities, (c) a recycled Michelson interferometer and (d) a recycled Michelson interferometer with arm cavities.

where M_1 and M_2 are the misalignment matrices of the input and the rear mirror, respectively, P denotes the propagator between the two mirrors[1] and r_1 and r_2 are the amplitude reflection coefficients of the two mirrors[2]. The steady-state equation for the field inside the cavity, E_{ins}, can then be written as

1. Note that both the plane wave phase factor and the Guoy phase shift are exactly the same for both beam directions.
2. We follow the convention that if the light is reflected from the coated surface of a mirror (drawn as bold curve in Fig. 3.2), an additional factor of (−1) has to be taken into account.

$$E_{ins} = P_{rl}E_{ins} + t_1E_0 = t_1(I - P_{rl})^{-1}E_0 \tag{69}$$

and the reflected field becomes:

$$E_{refl} = r_1M_1{}^{\dagger}E_0 - t_1r_2PM_2PE_{ins} = r_1M_1{}^{\dagger}\left(I - \frac{r_1^2 + t_1^2}{r_1^2}P_{rl}\right)(I - P_{rl})^{-1}E_0 \equiv M'E_0 \tag{70}$$

where t_1 is the amplitude transmission coefficient of the input mirror, E_0 is the input field and I is the identity matrix.

For small misalignments the only important modes are the fundamental TEM_{00} mode and the lowest order transverse (Hermite-Gaussian) modes, TEM_{10} and TEM_{01}. Using the notation where all three modes are the components of a single vector, an electromagnetic field in modal space can be written as:

$$E = \begin{bmatrix} a_{00} \\ a_{10} \\ a_{01} \end{bmatrix} \tag{71}$$

Making use of eqns. (54) and (60) and including terms to first order in Θ_x and Θ_y only[1], the propagator and the mirror misalignment matrices become

$$P(z_2, z_1) = e^{-ik(z_2 - z_1)}\begin{bmatrix} e^{i\eta} & 0 & 0 \\ 0 & e^{2i\eta} & 0 \\ 0 & 0 & e^{2i\eta} \end{bmatrix} \quad \text{and} \quad M(\Theta_x, \Theta_y) \approx \begin{bmatrix} 1 & -2i\Theta_x & -2i\Theta_y \\ -2i\Theta_x & 1 & 0 \\ -2i\Theta_y & 0 & 1 \end{bmatrix} \tag{72}$$

Assuming that the incoming light E_0 is a pure phase modulated TEM_{00} mode with a carrier which is resonant in the Fabry-Perot cavity and sidebands which are exactly anti-resonant, then the alignment signal S measured with a half-plane detector — as defined in eqns. (A.14) and (A.16) — can be obtained from eqns. (66), (67) and (70). To first order in Θ, S is given by

$$S = S_0\Gamma E_0^2[\Theta_{1x}cos(\eta_0 + \bar{\eta}) + \Theta_{2x}cos(\eta_0 + \bar{\eta} + \eta)] \tag{73}$$

---

1. Note that the eigenvalues of $M(\Theta_x,\Theta_y)$ can exceed unity, if just first order terms are included. Terms of at least second order in Θ_i must be included, if M is to be used in eqn. (70).

where $\bar{\eta}$ is the Guoy phase shift that the TEM_{00} mode of the reflected beam acquires between the input mirror and the photodetector. For a Fabry-Perot cavity S_0 and η_0 are complicated functions of r_1, t_1, r_2 and η. An attractive feature of eqn. (73) is that if additional higher-order modes are included in its derivation, they contribute to the order of Θ^3 or higher only. This is illustrated in Fig. 3.3, where the angular error signal S and the electromagnetic field strength of the modes inside the cavity are plotted against the misalignment angle of the front mirror Θ_{1x}. The calculations were made with one transverse degree of freedom only. It can be seen that the first order approximation (2 modes) is in good agreement with the 'exact' solution (22 modes) up to normalized angles of 0.3. Cavity parameters of a typical LIGO arm cavity were used, with a cavity length of 4 km, radii of curvature for the input and rear mirror of −14500 km and 7400 km, respectively, a perfectly reflecting rear mirror and an input mirror with a power transmission of 3%.

The Guoy phase η is pivotal to the mode decomposition technique. Each non-degenerate mode of the field has a different propagation phase associated with it, and it is precisely this property that allows us to infer which optical component in the optical train is misaligned. From eqn. (73) it can be seen that the Guoy phase difference of the misalignment signal, generated by the input and rear mirrors of a Fabry-Perot cavity, is the Guoy phase shift acquired by the fundamental mode when propagating from one mirror to the other. This has unfortunate implications for a highly degenerate cavity, for which the misalignment signals from the input and rear mirrors become indistinguishable.

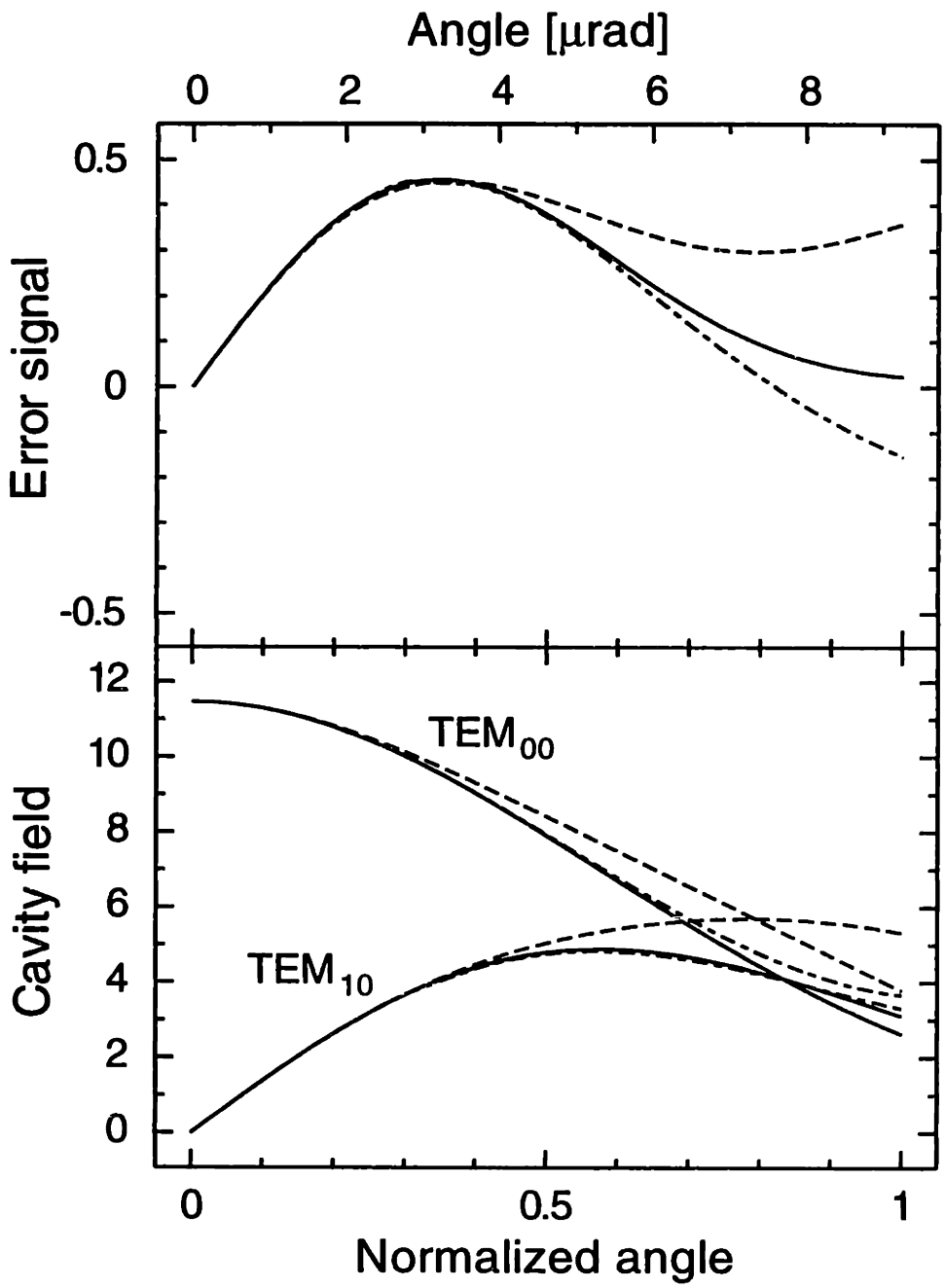

Figure 3.3: Angular error signal (top) and mode decomposition (bottom) as a function of the misalignment angle of the front mirror in a resonant Fabry-Perot interferometer. The calculations were made with one transverse degree of freedom only, using 2 modes (dashed line), 4 modes (dash-dotted line) and 22 modes (solid line), respectively. The cavity fields are given in units of the input field, whereas the error signal is given relative to the input power and the modulation depth, calculated for the Guoy phase of the detector which gives the maximum signal at small angles. The cavity parameters are given in the text.

3.3.2 Coupled cavities

The single cavity equations can be used to calculate the fields propagating in a pair of coupled cavities. Referring to Fig. 3.2(b), one can calculate the field reflected from mirror 3 by replacing M_1 and M_2 and their corresponding mirror reflectivities in eqns. (68) and (69) with M_3 and M', given in eqn. (70), that is

$$E_{refl} = r_3 M_3^{\dagger}\left(I + \frac{r_3^2 + t_3^2}{r_3} M_3 P_1 M' P_1\right)(I + r_3 M_3 P_1 M' P_1)^{-1} E_0 \tag{74}$$

where M_3 and t_3 are the mirror matrix and amplitude transmission coefficient for mirror 3, respectively, and P_1 and P_2 are the free space propagators corresponding to the length of each cavity.

3.3.3 Recycled Michelson

Similarly, for a Michelson interferometer with a partially transmitting mirror at the input, as shown in Fig. 3.2(c), all the complexity of the Michelson interferometer can be contained in a matrix operator M''. The field reflected from the input mirror is then given by

$$E_{refl} = r_3 M_3^{\dagger}\left(I + \frac{r_3^2 + t_3^2}{r_3} M_3 P_0 M'' P_0\right)(I + r_3 M_3 P_0 M'' P_0)^{-1} E_0 \tag{75a}$$

$$\text{with} \quad M'' = -t_{BS}^2 r_1 P_1 M_1 P_1 - r_{BS}^2 r_2 P_2 M_2 P_2 \tag{75b}$$

and the field at the antisymmetric output of the interferometer becomes

$$E_{antisym} = t_3 r_{BS} t_{BS}(-r_1 P_1 M_1 P_1 + r_2 P_2 M_2 P_2)(I + r_3 M_3 P_0 M'' P_0)^{-1} E_0 \tag{76}$$

where r_{BS} and t_{BS} are the amplitude reflection and transmission coefficients of the beamsplitter.

3.3.4 Complete interferometer

In this manner we can piece together any optical system and extract the spatially varying fields at any transverse plane along the direction of propagation of the wavevector. Fig. 3.2(d) shows the optical layout for the complete LIGO interferometer. Fields for this system can be calculated by replacing $(-r_1 M_1)$ and $(-r_2 M_2)$ in the equations for the

simple Michelson interferometer with matrices M_1' and M_2' which are similar to the cavity operator M' of Fig. 3.2(b) and eqn. (70). For the complete interferometer, then, the fields just inside the recycling mirror, in reflection from the recycling mirror and at the antisymmetric port, respectively, are:

$$E_{RC} = t_{RM}(I + r_{RM}M_{RM}^{\dagger}P_{l_0}M_C P_{l_0})^{-1}E_0 \tag{77}$$

$$E_{refl} = r_{RM}M_{RM}^{\dagger}\left(I + \frac{r_{RM}^2 + t_{RM}^2}{r_{RM}}M_{RM}P_{l_0}M_C P_{l_0}\right)(I + r_{RM}M_{RM}P_{l_0}M_C P_{l_0})^{-1}E_0 \tag{78}$$

$$E_{antisym} = t_{RM}M_D P_{l_0}(I + r_{RM}M_{RM}P_{l_0}M_C P_{l_0})^{-1}E_0 \tag{79}$$

where

$$M_C = -(t_{BS}^2 P_{l_1}M_1'P_{l_1} + r_{BS}^2 P_{l_2}M_2'P_{l_2}) \tag{80}$$

$$M_D = r_{BS}t_{BS}(-P_{l_1}M_1'P_{l_1} + P_{l_2}M_2'P_{l_2}) \tag{81}$$

M_C and M_D are the common (reflection from symmetric port of the beamsplitter) and differential (transmission out the antisymmetric port) Michelson operators, respectively; and

$$M_1' = r_{ITM1}M_{ITM1}^{\dagger}\left(I + \frac{r_{ITM1}^2 + t_{ITM1}^2}{r_{ITM1}}r_{ETM1}M_{ITM1}P_{L_1}M_{ETM1}P_{L_1}\right) (I + r_{ITM1}r_{ETM1}M_{ITM1}P_{L_1}M_{ETM1}P_{L_1})^{-1} \tag{82}$$

$$M_2' = r_{ITM2}M_{ITM2}^{\dagger}\left(I + \frac{r_{ITM2}^2 + t_{ITM2}^2}{r_{ITM2}}r_{ETM2}M_{ITM2}P_{L_2}M_{ETM2}P_{L_2}\right) (I + r_{ITM2}r_{ETM2}M_{ITM2}P_{L_2}M_{ETM2}P_{L_2})^{-1} \tag{83}$$

are the operators for reflection from the arm cavities. Here we revert to the standard naming convention of Fig. 2.4 (or see Fig. 3.4 below).

3.4 Resonance and dark port conditions

3.4.1 Resonance condition

The resonance condition of a cavity (both arm cavities and the recycling cavity) can be expressed as a condition on the round-trip operator M_{rt}

$$M_{rt} = e^{-2ikL} M_1^{\dagger} P_L M_2^{\dagger} P_L \tag{84}$$

When the phase of an eigenmode is an exact multiple of 2π, the mode resonates. The resonance condition is usually different for each eigenmode: higher order modes are not resonant, when the fundamental mode is.

The round-trip operator M_{rt} has an eigenmode E with eigenvalue c. If a cavity must be resonant for the eigenmode E, then the length of the cavity has to be adjusted by a length ΔL such that

$$-2k\Delta L + arg(c) = 2\pi n \quad \text{with } n \in Z \tag{85}$$

Similarly, a condition for an eigenmode to be anti-resonant can be written as

$$-2k\Delta L + arg(c) = 2\pi\left(n + \frac{1}{2}\right) \quad \text{with } n \in Z \tag{86}$$

3.4.2 Dark port condition

For dark port operation no carrier light leaves the interferometer through the antisymmetric port and all the power is reflected towards the recycling mirror. It is this condition which gives the recycling cavity a high finesse. Again, if E is the resonant eigenmode of the recycling cavity, then the power at the antisymmetric port can be written as

$$P_{dark} = \frac{1}{2} E^{\dagger}_{anti} E_{anti} \propto E^{\dagger} P_{l_C}{}^{\dagger} M_D^{\dagger} M_D P_{l_C} E \tag{87}$$

where l_C and l_D are defined in eqn. (15). Using the definitions of M_1' and M_2' above, the derivative can then be approximated by

$$\frac{d}{dl_D} P_{dark} \propto sin(-4kl_D + arg(\xi)) + \ldots \tag{88}$$

$$\text{with} \quad \xi = E^{\dagger} P_{l_2}{}^{\dagger} M_2'^{\dagger} P_{l_2}{}^{\dagger} P_{l_1} M_1' P_{l_1} E \tag{89}$$

where we neglect the terms due to resonant built-up in the recycling cavity. (These terms are zero at the exact dark port condition, that is, the dependence of the power in the recycling cavity on the differential Michelson length l_D is second order only.) The dark port condition can then be formulated as

$$-4k\,l_D + arg(\xi) = 2\pi\,n \quad \text{with } n \in Z \tag{90}$$

If both the resonance condition of the recycling cavity and the dark port condition of the Michelson are to be adjusted, it must be done iteratively. First, the resonance is set and the resonant eigenmode is used to calculate the differential Michelson length correction for the dark port condition. This will slightly change the resonant mode, so the resonance condition has to be applied again. This is repeated until both the common and the differential Michelson lengths have converged.

3.5 Calculated alignment sensitivity matrix

The modal model is a versatile tool and is used, for example, to calculate the alignment sensitivity matrix for various interferometer configurations and to determine sensitivity of the gravitational wave signal to angular misalignments.

3.5.1 The bimodal implementation

In this section we describe the modal model representation of the interferometer using the TEM_{00} and TEM_{10} modes only. In Fig. 3.4 we set up the coordinate system and naming conventions. Ten angular degrees of freedom completely describe the interferometer in Fig. 3.4, since misalignment of the beamsplitter is equivalent to tilts of the arm cavities. With the z-axis always pointing along the direction of the beam propagation vector and the y-axis always pointing upward, the x-axis is horizontal and perpendicular to the beam propagation direction. Since the beamsplitter mirrors the image in the horizontal but not the vertical direction, the coordinate system for the off-line arm is left-handed for the incident beam. Essentially, with each reflection in the interferometer, the coordinate system flips, that is, a right-handed coordinate system becomes left-handed. A positive misalignment angle corresponds to a right-handed rotation about the axis defined by the rotation vector (Fig. 3.4). Similarly, the convention for mirror reflectivity is that the amplitude reflection coefficients are negative for reflections from the coated

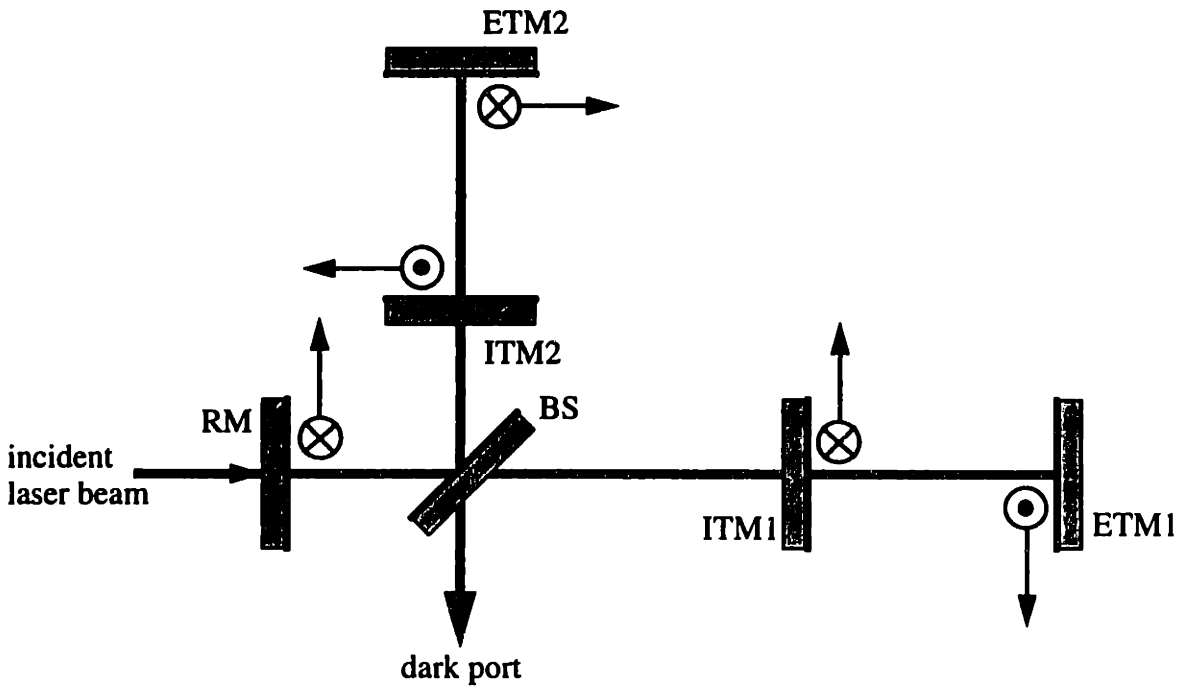

Figure 3.4: Sign convention of the misalignment angles. The rotation axes (vectors) for both horizontal and vertical misalignments are shown. The coated mirror surfaces are drawn in bold.

surface and positive for reflections from the substrate side. Mirror radii of curvature are positive when the concave surface faces the incident beam. In accordance with these conventions, the input field in the one-dimensional modal space is a vector:

$$E_{inc} = E_0 \begin{bmatrix} \sqrt{1 - x^2 - \alpha^2} \\ x - i\alpha \end{bmatrix} \tag{91}$$

where E_0 is the input field; x and α are the beam shift and tilt in units of beam radius and divergence angle, respectively. Similarly, propagation through a distance $(z_2 - z_1)$, and mirrors with misalignment angle Θ in units of divergence angle are represented by matrices:

$$P(z_2, z_1) = e^{-ik(z_2 - z_1)} \begin{bmatrix} e^{i\eta} & 0 \\ 0 & e^{2i\eta} \end{bmatrix} \text{ and } M = \begin{bmatrix} \sqrt{1 - 4\Theta^2} & -2i\Theta \\ -2i\Theta & \sqrt{1 - 4\Theta^2} \end{bmatrix} \tag{92}$$

The above expression for M is similar to that in eqn. (72), with one important difference: the diagonal terms must be expanded to order Θ^2 to ensure that the eigenvalues of M do

not exceed unity. The same argument holds for TEM_{00} component of the input field vector.

Using the fields in eqns. (77) through (83) and the above operators, we calculate the amplitudes of the RF photocurrents[1] on half-plane detectors placed at the output ports of the misaligned interferometer. Misalignment of the interferometer mirrors causes deviations from resonant lengths and longitudinal resonance is recovered by a "resonance finder". The resonance finder is a four-dimensional root finding routine which sets the microscopic interferometer lengths to null the signals on the length sensors (see Table 2.1), which is equivalent to the algorithm in Section 3.4. For each misalignment angle the Guoy phase shift from the appropriate port is adjusted to maximize the signal on the wavefront sensor which is primarily sensitive to that degree of freedom (see Table 2.9). The RF amplitudes on each wavefront sensor are scaled by the input power, the modulation depths of the phase modulated input fields and the normalized misalignment angle to deduce the alignment sensitivity matrix (see eqn. (50) in Chapter 2).

3.5.2 The alignment sensitivity matrix for the FMI

With the *design* parameters in Table 2.7 on page 34, we use the modal model to calculate alignment sensitivity matrix for the interferometer configuration studied in the FMI experiment, described in Chapter 4. The alignment sensitivity matrix for the FMI is given in the highlighted bottom right corner of Table 3.1. Also included are the Guoy phase shifts from the detection ports for maximum detection of the highlighted degree of freedom. The misalignment angles used for the calculations are linear combinations of the individual mirror angles θ_i:

$$\begin{bmatrix} ETM_D \\ ITM_D \\ ETM_C \\ ITM_C \\ RM \end{bmatrix} = \frac{1}{\sqrt{2}} \begin{bmatrix} 0 & -1 & 0 & 1 & 0 \\ -1 & 0 & 1 & 0 & 0 \\ 0 & 1 & 0 & 1 & 0 \\ 1 & 0 & 1 & 0 & 0 \\ 0 & 0 & 0 & 0 & \sqrt{2} \end{bmatrix} \begin{bmatrix} \theta_1 \\ \theta_2 \\ \theta_3 \\ \theta_4 \\ \theta_5 \end{bmatrix} \tag{93}$$

1. The RF amplitudes are a factor of 2 larger than the down-converted demodulator signals given in eqns. (13) and (14) in Chapter 2 (due to time averaging over one cycle). All numerical results presented in this work are given as RF amplitudes of the field.

where θ_1 and θ_2 are the misalignment angle of the ITM and ETM mirrors of the on-line arm, respectively, θ_3 and θ_4 are the misalignment angle of the ITM and ETM mirrors of the off-line arm, respectively, and θ_5 is the misalignment angle of the recycling mirror.

	PHASES		ANGULAR DEGREES OF FREEDOM				
PORT	RF	GUOY	*RM*	ITM_C	ITM_D	ETM_D	ETM_C
1 reflection, SCNR	I	152°	**-5.49**	0.73	0.88	0	0
2 reflection, SCNR	I	92°	-3.00	**1.65**	**1.61**	0	0
3 dark port, SC	Q	168°	-1.97	**-8.00**	**8.59**	0	0
4 dark port, C	Q	80°	-2.48	35.2	-28.7	**36.9**	**-30.1**
5 reflection, C	I	87°	-2.06	4.16	4.27	**4.66**	**4.69**
6 recycling, C	I	140°	**-46.9**	72.2	73.0	**67.8**	**68.5**

Table 3.1: Alignment sensitivity matrix for the FMI with *design* (ideal) parameters. The RF and Guoy phases of each detector (row) are optimized. Off-diagonal matrix elements which are less than 10^{-2} of the diagonal elements are rounded to zero.

The signals on WFS6 are redundant with those on WFS5, but we include them here as an optional detector. Experimental determination of the elements of the above matrix is the crux of the FMI experiment and is discussed in the next chapter.

Chapter 4

Experimental technique

In this chapter we describe the Fixed Mirror Interferometer experiment. The primary objectives of the experiment are to demonstrate the wavefront sensing scheme proposed in the preceding chapters and to characterize the performance of the wavefront sensors, which are designed to meet LIGO alignment requirements. Since the instrument response and control actuation of the fixed mirror system is vastly different from that of a LIGO-like suspended interferometer, issues of frequency response to noise inputs and actuator noise will not be addressed. Sensor noise will be dealt with insofar as is necessary to characterize the wavefront sensors. The main objective of the current FMI experiment is, then, to experimentally determine the alignment sensitivity matrix, to compare the experimental result and the matrix elements calculated using the modal model (see Section 3.5) and to demonstrate that wavefront sensing signals can be used to dynamically control *all ten* angular degrees of freedom simultaneously.

4.1 Overview of experimental layout

The optical layout of the FMI experiment is similar to that of the LIGO interferometer and reflects some of the complexity of the long baseline detector. There are four longitudinal and ten angular degrees of freedom to be controlled. The environmental excitations are significant since the experiment is neither in vacuum, nor particularly well isolated seismically. Two aspects of the experiment have required most of our efforts: first, since this was the first experimental test of the multiple frequency modulation scheme using this particular optical configuration, the lock acquisition and continuous operation have been a challenge, and, second, since we wish to make a quantitative comparison between theory and experiment, the absolute calibration procedures have been crucial. Main features of the experiment include wavefront sensors and demodulators, a VME-based data acquisition computer to read in 128 channels of data and to implement digital closed loop control, fast PZT actuators which allow for a 20 kHz bandwidth on the length control servos and an auxiliary pointing system for absolute angular calibration.

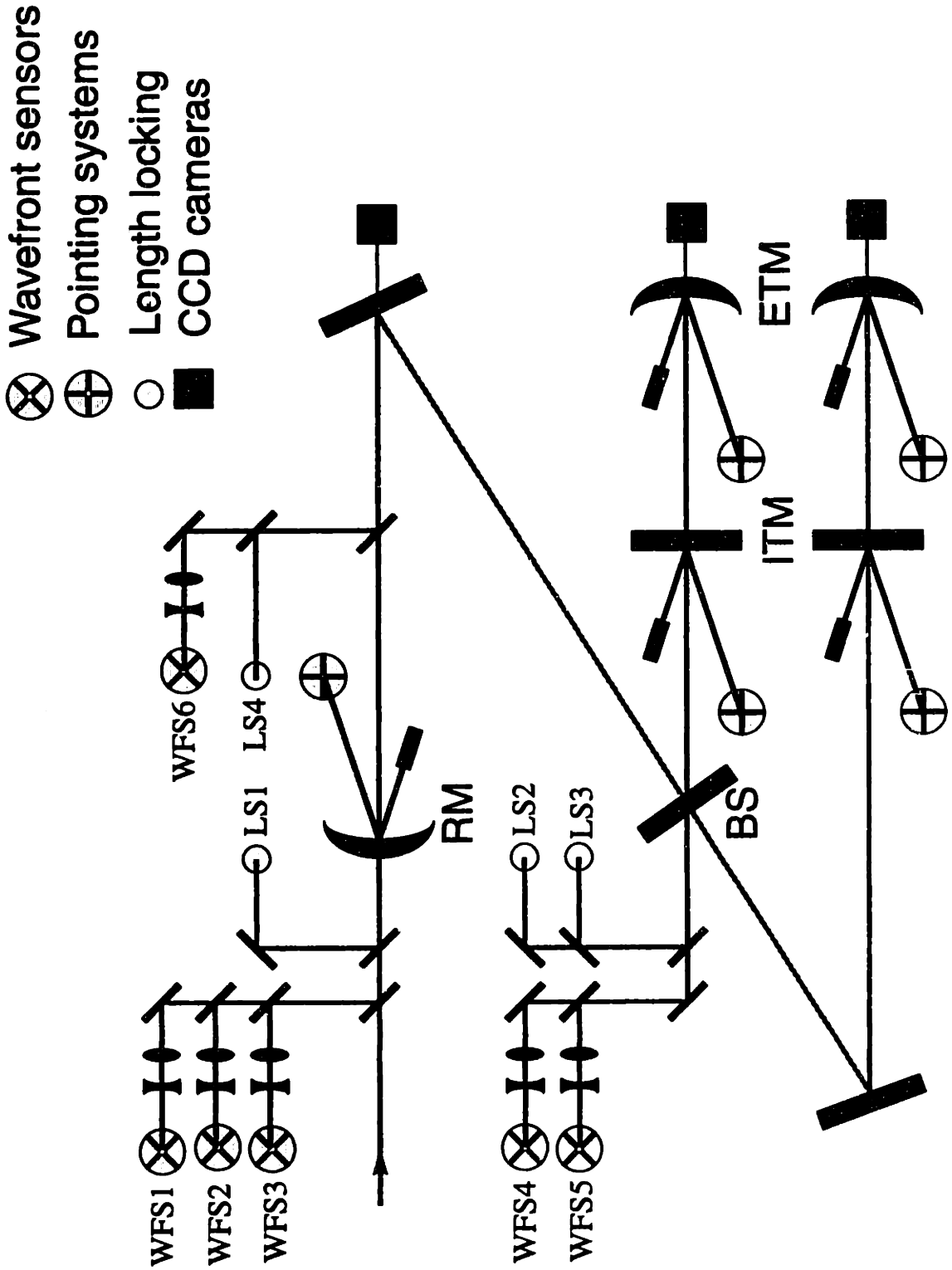

Figure 4.1: Schematic overview of the FMI experiment.

In Fig. 4.1 the optical layout of the FMI experiment is shown, along with the three sensing systems, namely, the length sensors, the wavefront sensors with Guoy phase telescopes and the pointing system. The interferometer layout differs somewhat from the typical LIGO layout; most of these differences pose no disadvantage to the experimental objectives, in fact, they are often beneficial. As a consequence of the limited space on the optical table and the constraints imposed on the interferometer lengths (see Table 2.4), the arm cavities are parallel and lie adjacent to each other and the recycling cavity has a fold in it. This provides a topology where there are two mirrors, and thus two actuators, per length degree of freedom. We take advantage of this by using one "fast" (large bandwidth but small dynamic range) and one "slow"(small bandwidth but large dynamic range) PZT actuator to control each length.

The interferometer parameters realized in the FMI experiment were quite similar to the design parameters. Both are listed in Table 2.7. The model predictions which are compared with the measurement use the experimentally determined parameters.

4.2 Description of the alignment sensing measurement

Using eqn. (50), the signal on the j-th wavefront sensor signal is converted into an ADC voltage by the expression:

$$V_j^{ADC}(t, \eta, \Theta) = 2\varepsilon P_j J_0(\Gamma) J_1(\Gamma) k_{PD} G_{ADC} Z_j A_{ij} \theta_i cos(\eta - \eta_{ij}) cos(\Omega t + \phi_{ij}) \quad (94)$$

where ε is the quantum efficiency of the photodiode; θ_i is the misalignment angle for the i-th degree of freedom; A_{ij} is the alignment sensitivity matrix; η is the Guoy phase shift to the detector (see Section 4.3.2); η_{ij} and ϕ_{ij} are the intrinsic Guoy and RF phases, respectively; P_j is the TEM_{00} power on the detector; Ω and Γ are the RF modulation frequency and depth, respectively; G_{ADC} is the ADC gain; Z_j is the transimpedance gain of the wavefront sensor; and k_{PD} is a constant factor which scales the infinite half-plane photodiode used in calculations to a finite apertured diode. All the optical properties of the interferometer and the fields propagating in it are contained in the alignment sensitivity matrix, A_{ij}, and these are, in fact, the coefficients we wish to compare with the modal model predictions.

The measurement of the alignment sensitivity matrix is carried out by dithering each

of the ten angular degrees of freedom simultaneously — but at different frequencies — and writing the measured wavefront sensor signals to disk. Capturing a data set entails acquiring longitudinal and angular lock of all degrees of freedom (detailed in Section 4.4.3). At this point the interferometer is resonant and aligned and all degrees of freedom are under closed loop control. The angular degrees of freedom are then modulated at frequencies outside the bandwidth of the angle servos, typically 40 to 100 Hz. Power spectral densities for the pointing system and wavefront sensor signals are computed off-line and the alignment sensitivity matrix elements are inferred using the amplitudes of the signals at each dither frequency and scaling appropriately by the measured optical and electronics gains. The signal on a given wavefront sensor at each dither frequency corresponds to the sensitivity of the detector to that particular degree of freedom. In this manner, by measuring the signal amplitudes at all the dither frequencies present in the Fourier spectrum for each wavefront sensor, we construct the alignment sensitivity matrix.

4.3 Experimental apparatus

4.3.1 Wavefront sensor

Since our alignment sensing scheme is predicated on detection of spatial asymmetries of the light where the combination of the TEM_{00} component of the carrier beating against the TEM_{10} component at the RF sideband frequency and the TEM_{10} component of the carrier beating against the TEM_{00} component at the RF sideband frequency is measured, the wavefront detector is a quadrant photodiode (see Fig. 4.2). The wavefront sensor consists of two parts: the "head" is a module containing the quadrant photodiode with a tuned circuit, an RF preamplifier and a DC diode current sensing stage following each diode segment; each detector head is followed by a demodulator board, where the photocurrent signal for each quadrant is down-converted separately [30]. The outputs of this board are the demodulated signals and the average photocurrent for each segment of the photodiode. The five demodulator boards are hosted in a VME chassis.

The photodiode is an Advanced Photonix, Inc. quadrant photodetector, SD-197-23-21-041. Each segment has area 5.4 mm^2. The absolute responsivity for argon light at 515 nm is about 0.22 A/W. The photodiode operates in a linear regime up to

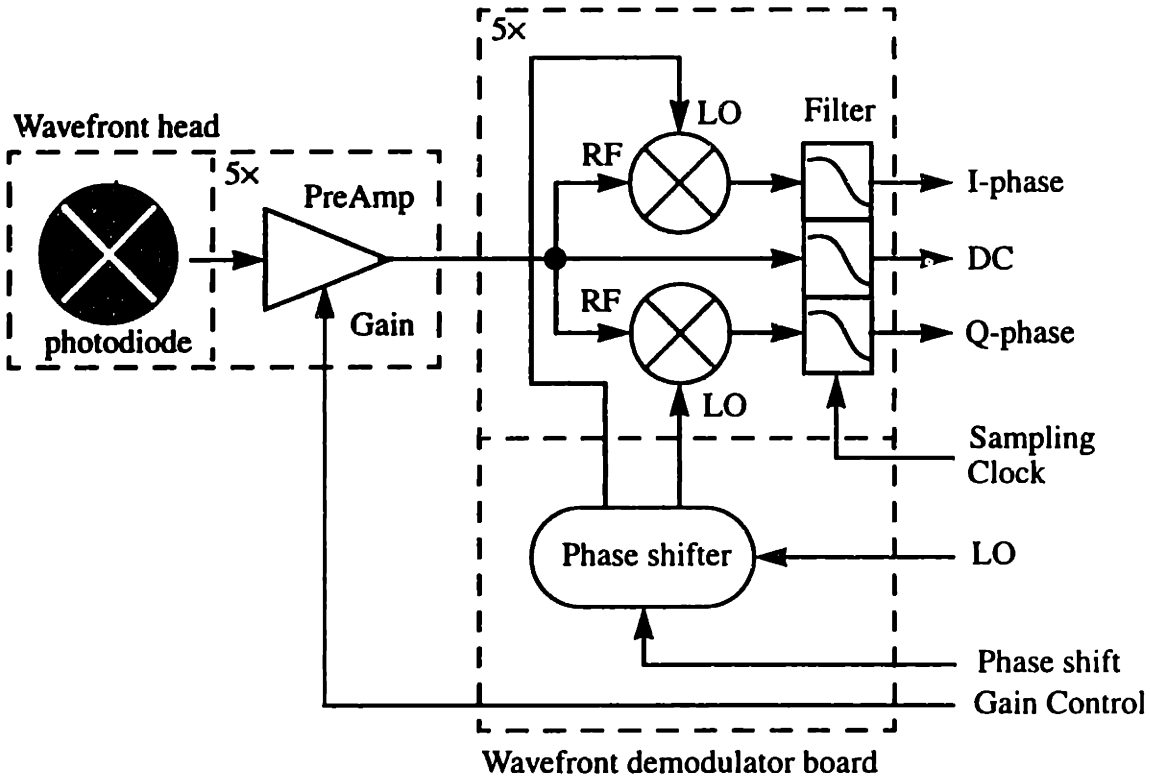

Figure 4.2: Wavefront Sensor.

0.1 mW/mm^2 and goes into saturation about an order of magnitude above this level. Typical DC photocurrents during normal operation are about 0.5 mA, the RF signal current is about 0.8 μA rms. At RF frequencies the photodiode capacitance becomes important; it is about 10 pF with a 50 V bias. The bias is applied through an LC filter to decouple the bias supply from the RF signal. The RF photocurrent is converted to voltage with an inductive load in parallel with the diode capacitance (a tuned circuit which is resonant at the modulation frequency), after which it is amplified using a low-noise CLC425 amplifier. The shot noise limited photocurrent is about 20 μA per segment. Since the angular misalignment signal is given by the differences between two opposite segments of the quadrant photodiode, the four quadrants have to be well balanced, that is, their gains and intrinsic time delays should be equal within the required measuring precision.

The demodulator board has an RF part and a low frequency part. The RF part, which performs the actual demodulation of the detected light intensity, comprises of a local oscillator which provides the demodulation clock signals and a mixer which performs the

down conversion. Down-conversion is done into both the In-phase and the Quadrature-phase. The local oscillator is running at double the modulation frequency and is synchronized to an external clock signal using a phase-locked loop (PLL). The demodulation signals for I-phase and Q-phase down-conversion are obtained using two divide-by-two counters — one triggering on the positive edge and one on the negative edge of the local oscillator. The PLL has an additional advantage that its reference input can be used as a global RF phase adjuster with a constant voltage-per-radian conversion ratio. The down-converted signals are filtered and amplified to give a 10 kHz bandwidth.

The calibration of the wavefront sensor RF transimpedance gain, Z_i in eqn. (94), is performed in two ways: one method is to use the shot noise equivalent photocurrent to infer the transimpedance and the other method is to shine amplitude modulated light of known modulation depth on the photodiode and directly measure the RF transimpedance. Gain calibrations using these two methods are consistent to within a few percent. The uncertainty in the absolute gain is about ± 5% for the 32 and 39 MHz wavefront sensors and ± 10% for the 58 MHz modules.

4.3.2 Guoy phase telescopes

The Guoy phase at a given detector is chosen to maximize the signal due to misalignment of the primary degree of freedom for which it is responsible, as highlighted in Section 2.4.3. For each detector, the magnitude of the off-diagonal terms in the sensitivity matrix have sinusoidal dependence on the Guoy phase shift, but unlike the diagonal terms, they are usually closer to the zero of the sinusoidal variation. The off-diagonal terms of the alignment sensitivity matrix are thus first-order sensitive to the Guoy phase shift, while the diagonal terms are only second-order sensitive. Consequently, some care must be taken in the design and implementation of the Guoy phase telescopes.

Given the uncertainties in the focal lengths and positions of the lenses, an optimization algorithm based on a simulated annealing technique [31] is used to minimize errors in the Guoy phase and spot size and at the same time make the telescopes as insensitive as possible to uncertainties in their physical layout. We use a two lens solution for the telescopes, which greatly simplifies the algorithm for optimizing the design constraints. The resulting Guoy phase telescopes for the wavefront detectors are listed in Table 4.1. The detector and demodulation frequency are given in column 1. The angle in column 2 is

WFS	Φ_{Guoy}	f_1 (m)	z_1 (m)	f_2 (m)	z_2 (m)	z_{det}(m)	ERROR
1 (32)	152°	+0.500	5.661	–0.025	6.212	6.458	±8°
2 (32)	92°	+0.500	5.661	–0.025	6.185	6.629	±6°
3 (39)	168°	+0.500	1.845	–0.100	2.460	2.746	±17°
4 (59)	80°	+0.500	1.845	–0.050	2.305	2.682	±7°
5 (59)	87°	+0.500	5.661	–0.025	6.184	6.622	±6°
6 (59)	140°	+0.500	1.525	–0.050	2.055	2.388	±16°

Table 4.1: Data for the Guoy phase telescopes. The Guoy phase shift is given from the port.

the Guoy phase which maximizes the diagonal degree of freedom of the alignment sensitivity matrix. It is the propagation needed from the port in question: for example, for wavefront sensor 1, which detects misalignment of the recycling mirror primarily, the Guoy phase which maximizes the signal is 152° from the recycling mirror, or 205° from the waist (nominally at the flat arm cavity input mirrors). f_1 and z_1 are the focal length and position from the waist of the first lens, respectively; f_2 and z_2 are the focal length and position of the second lens, respectively; and z_{det} is the position of the wavefront sensor (see Fig. 4.3). The errors listed are primarily due to uncertainty in the position of the second lens, z_2, which is not intrinsically difficult to measure, but makes the greatest contribution to the error budget because of the particular optimization process we use. We eliminate the uncertainty in the beam up to z_2 (the greatest error comes from the uncertainty in f_1) by a sequence of steps which we call the *infinity adjustment*. We move the second lens to a position z_∞ so the spot is focussed at infinity, which is equivalent of minimizing the divergence of the beam. We then move it by a distance $\Delta z = z_\infty - z_2$, which is known from calculation and easily measured since it is typically a centimeter. The remaining errors come from our ability to determine z_∞, and hence z_2. Since we use the properties of the telescope to minimize the errors, it is no coincidence that the signals on the wavefront sensors with the greatest uncertainty in the Guoy phase are also the most insensitive to Guoy phase shift.

The typical two-lens design of Guoy phase telescopes uses the first lens to focus the beam, more gently for longer focal length lenses. As the beam goes through a waist (near the focal plane), it acquires an additional 180° of Guoy phase. The second lens is placed

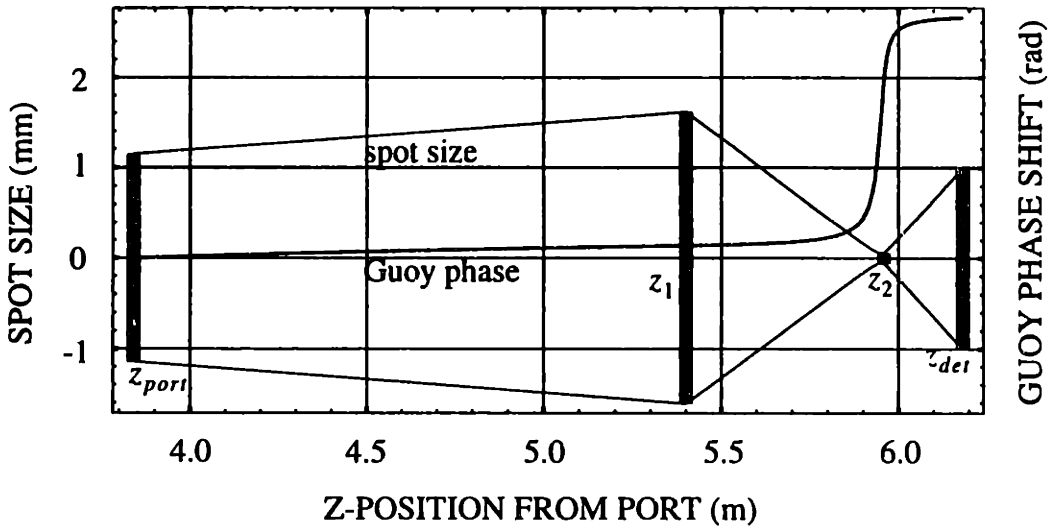

Figure 4.3: Beam profile and Guoy phase shift for a Guoy phase telescope. The spot size and guoy phase shift are plotted as a function of position from the port. z_{port} refers to the position of the port (recycling mirror in this case), z_1 and z_2 to the positions of the first (converging) and second (diverging) lenses, respectively, and z_{det} to the position of the detector.

near the focal plane of the first lens, at a distance such that it picks up the required Guoy phase. Since the spot size near the focus is very small (typically 100 μm), the second lens is usually a strong negative lens which also expands the beam (shown in Fig. 4.3). This is a particularly robust scheme since the distances which are practically most difficult to control are least critical. Specifically, there are three advantages to this design: first, insensitivity to the position of the first lens, which is usually a few meters from the output port and can have a large uncertainty; second, the spacing between the two lenses is crucial, but this is typically a few centimeters and, therefore, easily determined; and, third, the detector position is not critical, again a desirable effect. In fact, with this telescope design, the detector can be ±1 cm from the design position and contribute less than 0.1% to the Guoy phase error.

4.3.3 Input optics train

The input optics train consists of three optical paths: light from the laser is split into the frequency stabilization path, the carrier path and the frequency-shifted subcarrier path. After shifting the SC frequency and adding the phase modulation sidebands, light from the C and SC paths is recombined and launched into a fiber, which serves as a mode cleaner

(see Fig. 4.4).

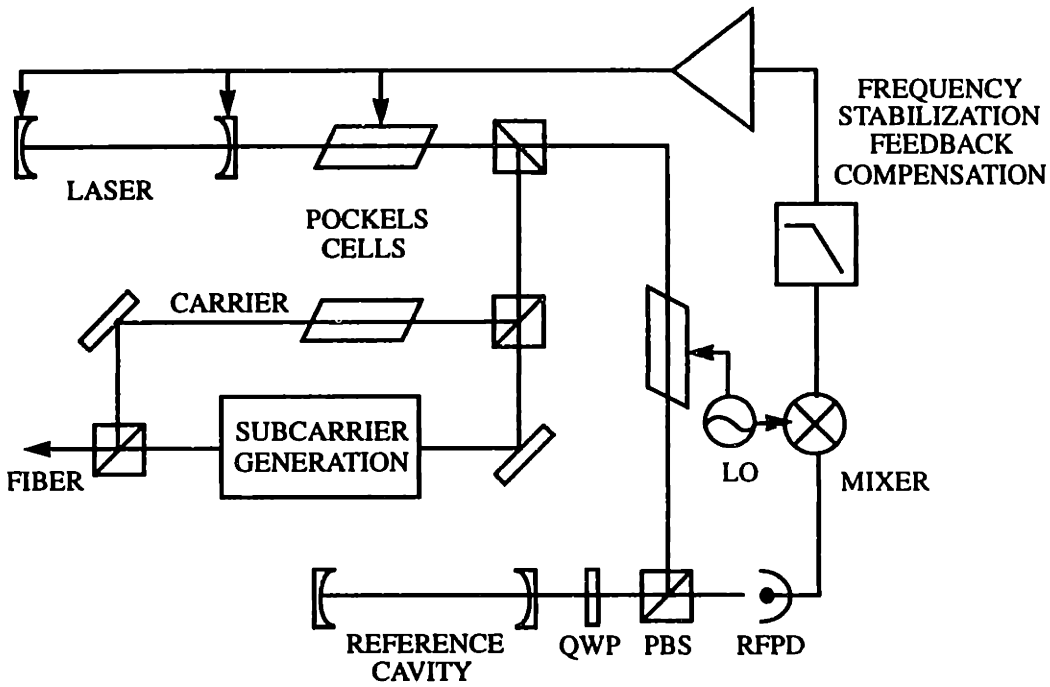

Figure 4.4: Input optics train. The subcarrier generation scheme is detailed in Fig. 4.5. QWP refers to a quarter-wave plate; PBS to a polarizing beamsplitter; RFPD to an RF photodiode; and LO to the local oscillator.

Frequency stabilized laser

The light source for the FMI experiment is frequency-stabilized light from a Spectra Physics 2020 Ar^+ CW laser operated single-mode at 515 nm. Typical output power during operation is 250 mW. The frequency of the laser is stabilized by locking the laser frequency to a reference Fabry-Perot cavity using the ubiquitous heterodyne reflection locking technique outlined in Section 2.2.1. The fluctuations of the resonant frequency of the reference cavity are significantly lower than those of an unstabilized Ar^+ laser and we achieve typical frequency noise levels of 0.4 $Hz/\sqrt{Hz}$. About 10% of the laser light is used for frequency stabilization and is phase modulated at 12.33 MHz with a Pockels cell. The light reflected from the cavity is measured with an RF photodiode and demodulated to obtain the error signal which is used to control the laser frequency. The RF photodiode (RFPD) in this case is a monolithic EG&G SGD-200 silicon diode reverse biased at 170 V. Again the RF photocurrent is converted into a voltage using a resonant circuit comprised

of the diode capacitance in parallel with an inductor, followed by two stages of amplification. The RF signal is down converted using a double-balanced mixer. Control signals at low frequencies (DC to 300 Hz) are applied to the "slow" PZT actuator at the output coupler of the laser resonator, at intermediate frequencies (DC to 100 kHz) to the "fast" PZT at the cavity rear mirror and at high frequencies (DC to 1 MHz) to two Pockels cells in series, which are external to the laser cavity.

Carrier and subcarrier generation

The carrier light is phase modulated at 58.5 MHz using a Pockels cell. The subcarrier light is double-passed through an acousto-optic modulator (AOM) at 195.5 MHz to give a frequency shift of 391 MHz relative to the carrier (detailed in Fig. 4.5), after which it passes through two Pockels cells at 39 and 32 MHz, respectively.

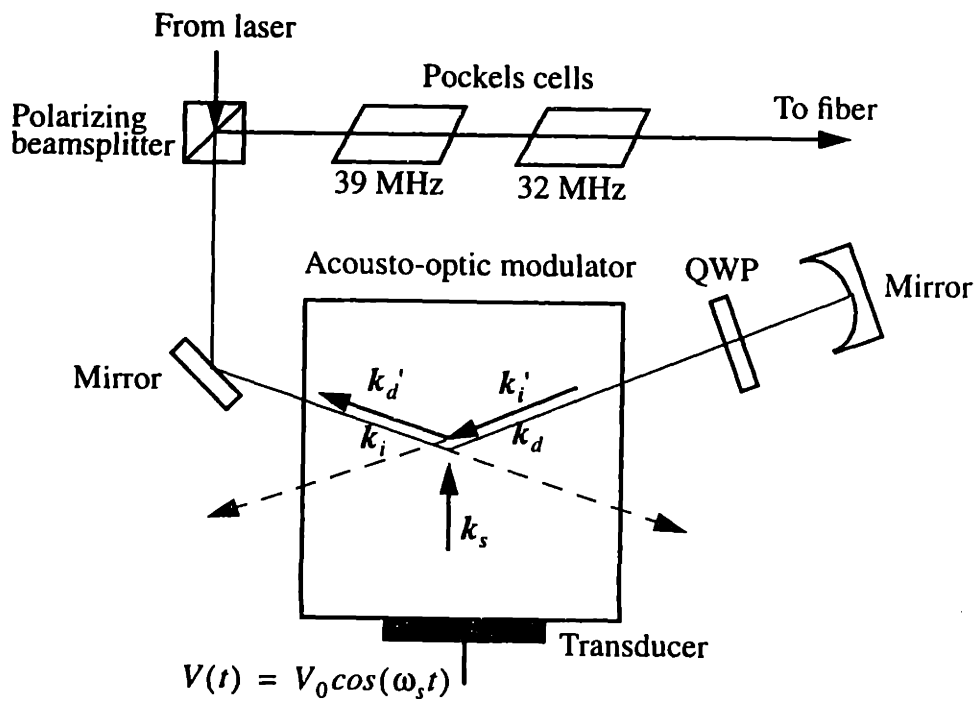

Figure 4.5: Subcarrier generation using a double-passed acousto-optic modulator.

The principle behind the double-passed AOM is simple: an acoustic wave induces a spatial modulation of the refractive index of the acousto-optic medium, which diffracts the passing optical wave. Using the notation in Fig. 4.5, from conservation of momentum the wavevectors for the incident, diffracted and acoustic waves — k_i, k_d and k_s, respectively

— follow the relationship

$$k_i + k_s = k_d \tag{95}$$

and from conservation of energy

$$\omega_i + \omega_s = \omega_d \tag{96}$$

The diffracted wave is both deflected and frequency-shifted relative to the input wave. Upon reflection from a curved mirror, the wave returning to the AOM is $ck_i' = -(\omega_i + \omega_s)\hat{k}_d$, and exiting the AOM we get

$$ck_d' = -(\omega_i + 2\omega_s)\hat{k}_i \tag{97}$$

which is a wave travelling in the opposite direction to the input light and shifted in frequency by $2\omega_s$. The curved mirror has the advantage of retroreflecting the single-passed light beam when its deflection angle changes due to small adjustments in frequency. The incoming laser light is well polarized and is maximally transmitted through the beamsplitter, its polarization is rotated by 90° upon double-passing the quarter-wave plate, so the light returning from the AOM is maximally reflected towards the Pockels cells and fiber.

The Isomet 1250C AOM used in the FMI experiment has a maximum diffraction efficiency of 90% per pass with 800 mW of RF power at about 200 MHz. The double-passed diffraction efficiency of 80% was seen to gradually degrade to about 50% over a year.

After passing through two modematching lenses each, the carrier and subcarrier beams are recombined on a beamsplitter and launched into a fiber which transports light from the input optics table to the interferometer table. The fiber functions as a mode cleaner and ensures collinearity of the carrier and subcarrier light which is incident on the interferometer. Intensity drifts at the output of the fiber are measured to be about ± 5% over minutes.

Modulation depths are measured using the intensity spectrum of a scanning Fabry-Perot cavity. The modulation depths in most of the FMI data runs are typically: $\Gamma_{32} = 0.423 \pm 3\%$, $\Gamma_{39} = 0.253 \pm 7\%$ and $\Gamma_{32} = 0.205 \pm 8\%$. Since the sideband power scales as Γ^2, the low modulation depths limit our measurement sensitivity.

4.3.4 Mirror actuators

Longitudinal and angular positions of the FMI mirrors are controlled by piezoelectric transducers (PZTs). Three varieties of actuators are used in the FMI. Angular degrees of freedom are controlled using Physik Instrumente P-286 disk translators with a maximum expansion range of 100 μm at 1000 V and a resonant frequency of 2.5 kHz. These are bimorph piezo actuators where a thin ceramic disk which contracts radially is attached to a metal sheet of similar size. This bending effect causes the center of the disk to arch up when a voltage is applied. Two disk PZTs, one for each angular degree of freedom, are attached to the mic heads of a gimbal mount (Burleigh SG-201). For longitudinal actuation we use two types of PZT actuators. The "slow" PZTs are commercially available Burleigh PZ-81 3-element models with a typical range of 2 μm at 1000 V. These PZTs have resonances at about 300 Hz. The three PZT elements are balanced to give pure axial translations of the mirrors which are centered on the actuation axis. The "fast" PZTs were developed in-house to satisfy the specific needs of the FMI experiment. Since the seismic, acoustic and mechanical excitations are rather significant in the FMI environment, particularly from DC to a couple of kilohertz, the bandwidth of the length control servos should exceed 10 kHz to ensure sufficient gain in the kilohertz band. PZT and mounting structure resonances pose a severe limitation to the bandwidth and we found it necessary to design an actuator with a flat frequency response out to tens of kilohertz. A schematic representation of the fast PZT actuator is shown in Fig. 4.6.

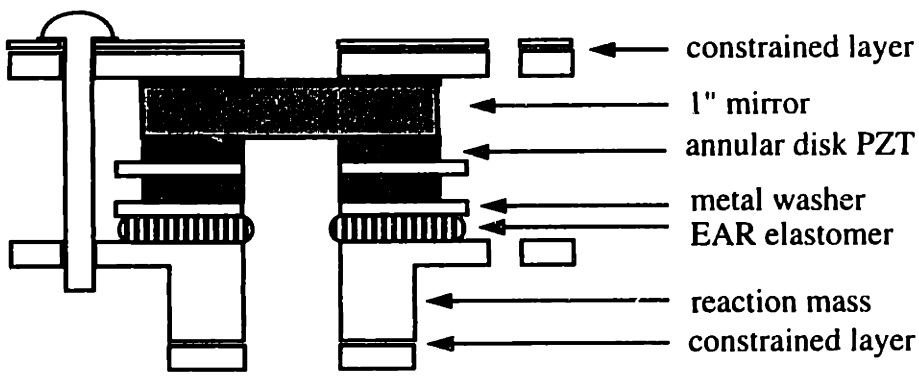

Figure 4.6: Fast PZT actuator: the reaction mass and clamp plate have a constrained layer of epoxy; the EAR elastomer is used for compliance; electric fields are applied using metal washers.

The notable features of the actuator design are the use of constrained layer damping to suppress low-frequency shear modes; a relatively massive bottom piece to provide sufficient reaction force; clamping with a radial arrangement of screws, which allows for the absence of adhesives — an alleged cause of contamination of mirror coatings; the use of an elastomer as a compliance layer to ensure that the mirrors don't crack; and maintaining a 1/2" clear aperture. Two PZTs are used in a push-pull arrangement, one forward- and one reverse-biassed. The annular disk PZTs (Piezo Kinetics Inc. PKI-550) are specified for maximum voltage of 400 V forward or 200 V reverse, which limits the operating range to ±200 V. The motion sensitivity is about 450×10^{-12} m/V which limits the maximum range of the fast actuator to approximately one-half of a fringe. Though the first resonance occurs at about 60 kHz, there is an in-line resonance at about 40 kHz which can be suppressed by careful tightening of the screws (we find 5 in-lbs to work best). Typical actuator characteristics are summarized in Table 4.2.

Actuator	Sensitivity	Resonant frequency
Angle actuator	100×10^{-9} m/V [a]	2.5 kHz
"Fast" length actuator	0.45×10^{-9} m/V	60 kHz
"Slow" length actuator	2.0×10^{-9} m/V	0.5 kHz

Table 4.2: Characteristics of the PZT actuators.

a. For our particular mounting geometry this corresponds to about 3 μrad/V.

4.3.5 Pointing system

The pointing system is a standard optical lever. A 3 mW intensity stabilized diode laser (Power Technology, Inc. LPM-03) is reflected from an auxiliary mirror affixed to the gimbal plate on which the interferometer mirror is mounted. The reflected beam is incident on a quadrant photodiode. Each quadrant is followed by two amplifier stages where sum and difference signals are processed and output through a 1 kHz single pole filter.

The absolute angle sensitivity of the pointing system is calibrated by using a plane glass plate of known thickness placed between the laser and the photodetector at a known

angle which deflects the beam on the photodetector. For a plate of thickness T at an angle θ, the deflection, dx, is given by

$$dx = T\left(\sin\theta - \frac{\cos\theta\sin\theta}{\sqrt{n^2 - \sin^2\theta}}\right) \tag{98}$$

We use a 1.06 mm thick BK7 plate with refractive index $n = 1.514$ at a fixed angle of 10.3° to get a deflection of 0.065 mm. Over a 1 m lever arm this corresponds to angles of about 0.07 mrad or 1.4 V for a typical pointing system sensitivity of 20 V/mrad. This in-situ calibration plate is itself calibrated using a micrometer stage and is accurate to ±3%. The pointing system calibration is observed to drift by ±15% due to changes in beam shape and size and due to pointing fluctuations.

4.3.6 VME-based data acquisition and control system

The real-time data acquisition system used in the FMI experiment consists of a Motorola 68040 based embedded controller, four 32-channel (single-ended) 12-bit analog-to-digital converters (ADCs) and a 16-channel 12-bit digital-to-analog converter (DAC) residing on a VME bus. To ensure a rapid data transfer rate the VME processor stores data locally to a SCSI disk. A maximum sampling rate of 1 kHz can be achieved.

The front end CPU runs an EPICs database on top of the VxWorks real-time operating system. The EPICs system on a Sun workstation is then used to connect the EPICs database via an ethernet link and to provide a graphical user interface (GUI). The network connection and the EPICs database are too slow to keep up with the 1 kHz sample rate, so a C-program is run on the front end to link to the database kernel performing the fast I/O tasks and the digital servo control. Consequently, the database is used only for status and operator control channels, all other functions are performed by the lower-level sequencer.

4.4 Servo systems

4.4.1 Length control

There are four longitudinal degrees of freedom to be held on resonance in the interferometer: the two arm cavity lengths, the recycling cavity length and the differential Michelson. In Fig. 4.7 one of the four length sensing and control systems is shown.

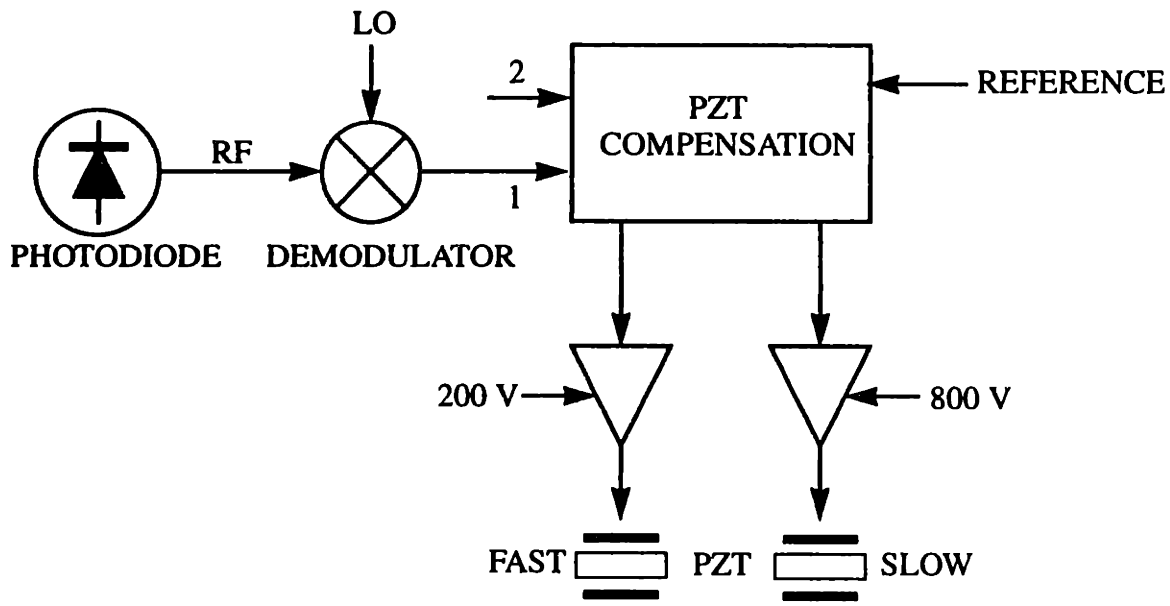

Figure 4.7: Length sensing and control.

Referring to the notation in Fig. 4.1, the sum of the two arm lengths is measured with LS4 which detects the beating of the reflected light between the carrier and its sidebands. The difference of the two arm cavity lengths is measured by LS3 at the dark port. The two measured RF signals are separately down-converted. The resulting error signals are added and subtracted to obtain the error signals for each arm cavity. The error signals are fed into a compensation network which produces the needed control signals for the ITMs and ETMs. The near mirrors are mounted on the slow large dynamic range PZTs, while the back mirrors are mounted on fast PZTs. The common length of the near Michelson interferometer — equivalently the recycling cavity length — is measured with the subcarrier and its 32 MHz non-resonant sideband at the symmetric port (LS1), whereas its differential length is measured with the subcarrier and its 39 MHz resonant sideband at the dark port (LS2). No adding or subtracting is required here, because the recycling mirror and the recycling cavity folding mirror both adjust the common length, whereas the differential length is adjusted by the beamsplitter and the off-line arm folding mirror. High voltage drivers are used to generate the required signals for the PZTs. The amplitude modulated light is detected using the same type of RF photodiode circuit described in Section 4.3.1, but reverse biased at 170 V.

Several design considerations and constraints are important for the PZT compensation

network. To counter the mechanically noisy environment of the FMI, we require the bandwidth of the length servos to be above 10 kHz, but we also need a large dynamic range at DC. To this end we divide the control signal into a low frequency range and a high frequency range to drive both the slow and the fast PZTs. The control signal of the fast PZT is used as the error signal of the slow PZT compensation. The fast PZTs have a sharp resonance ($Q \cong 10$) at about 60kHz, which is notched out. To facilitate acquisition of the resonant state in the interferometer, it would be desirable to have an unconditionally stable servo controller, but this imposes gain limitations which would not allow long locking periods. For this reason we implement a single pole at 1 Hz with a lag compensation (a pole/zero pair at 10 Hz / 5 kHz). The latter is engaged once initial lock is acquired. Salient features of the PZT compensation network are listed in Table 4.3.

DESCRIPTION	VALUE
Pole	10 Hz
Notch for compensating the PZT resonance	57 kHz (Q=10)
Double poles	48 kHz (Q=1)
Additional lag compensation (pole/zero)	10 Hz / 5 kHz
Additional pole for slow PZT compensation	1 Hz
Unity gain (fast PZT)	25 kHz
Unity gain (slow PZT)	~100 Hz

Table 4.3: Length control compensation network

The control signals are input to low-noise high voltage amplifiers which drive the PZTs. The slow PZTs use a 0 - 800 V high voltage amplifier, while the fast PZTs use a ±200 V power supply.

4.4.2 Angular control

The alignment degrees of freedom are controlled by a digital servo system implemented via the VME computer described in Section 4.3.6. The closed loop control sequencer performs the following functions: the error signals are generated by differencing the down-converted signals from opposite quadrants of the wavefront sensor, which are read into the ADCs; they are then multiplied by the inverse of the alignment

sensitivity matrix and passed through a low-pass digital filter (single pole at 0.1 Hz) to yield the feedback signals. The digital filter is given by [32]:

$$U_k = e^{-2\pi f_p T_s} U_{k-1} + K_s(1 - e^{-2\pi f_p T_s}) E_{k-1} \tag{99}$$

where U_k is the control signal of the present time sample, U_{k-1} is the control signal of the previous time sample, E_{k-1} is the error signal from the previous sample period, f_p is the pole frequency, T_s is the reciprocal of the sample rate and K_s is the DC gain, defined as $K_s = (f_{BW}/f_p - 1)$.

The control signals are written to the DAC channels which drive the inputs to the high voltage angle PZT drivers after additional analog low-pass filtering to remove digitization noise.

4.4.3 Lock acquisition

A lock acquisition sequence for the interferometer is outlined below:

- align the ITMs by optimizing the overlap of the spot from each arm at the antisymmetric port (minimize contrast defect);
- engage the differential Michelson length servo (LS2);
- align the recycling cavity by scanning the RM and minimizing the TEM_{10} mode in the spectrum;
- engage the recycling cavity servo (LS1);
- the recycled Michelson is now locked using the subcarrier loops[1];
- adjust beam centering on the wavefront sensors using the differential DC photocurrents;
- engage the recycled Michelson subset of the angle servos;
- adjust ETM alignment for best spot overlap on the transmission cameras;
- adjust arm cavity length offset to make *both* arms flash through resonance[2], taking care not to let the subcarrier come into resonance in either arm;
- simultaneously ramp up the gain in LS3 and LS4 servos;

1. Both the LS1 and LS2 servos have enough phase margin to acquire lock with the high gain "slow" controllers engaged.
2. The partial state when the carrier is resonant in just one of the arm cavities does not disturb the Michelson loops, but causes a sign flip (due to a bright fringe at the antisymmetric port) in the arm servos. Therefore, *both* arms must be near resonance to engage the arm cavity loops.

- the arm cavities lock;
- ramp up the gain to the "slow" controllers;
- engage all angle servos;
- at this point all four longitudinal and all ten angular degrees of freedom are under closed loop control.

4.5 Data Analysis

A typical data run is about 30 seconds long and data from the wavefront sensors and the pointing system along with auxiliary channels are gathered at a sampling rate of 1 kHz (or 500 Hz), yielding a total of about 8 MB of data on disk. Before analysis the data is binned (usually 2 or 4 samples) and truncated to 2^{14} data points to optimize for the following Fourier transforms.

4.5.1 Fourier analysis

Each angular degree of freedom is dithered using a sine function at a frequency between 40 and 100 Hz and is demodulated using the same frequency. The upper plot in Fig. 4.8 shows the amplitude spectral density of the pointing system measuring the horizontal misalignment of the RM. Clearly present is the peak at 40 Hz, the dither frequency for horizontal misalignment. The smaller peak at 44 Hz is due to the vertical dither and is a measure of the alignment of the pointing system with respect to the rotation axis of the mirror. We note that this effect is only a few percent. To obtain the physical amplitude of the angular dither, the time series data is multiplied by a sine function at the dither frequency. The resulting time series is then summed over all data points, thus averaging out signals at all frequencies other than the one at the dither frequency. This down-conversion is repeated for each angular degree of freedom using the corresponding pointing system spectrum with its dither frequency. Scaling by the calibration of the individual pointing systems we calculate the true physical alignment dither amplitudes, θ_j, for each angular degree of freedom, j.

Since each angular degree of freedom has a different dither frequency, the wavefront sensor signals corresponding to a given degree of freedom appear at that particular dither frequency. The lower plot in Fig. 4.8 shows the amplitude spectral density of the

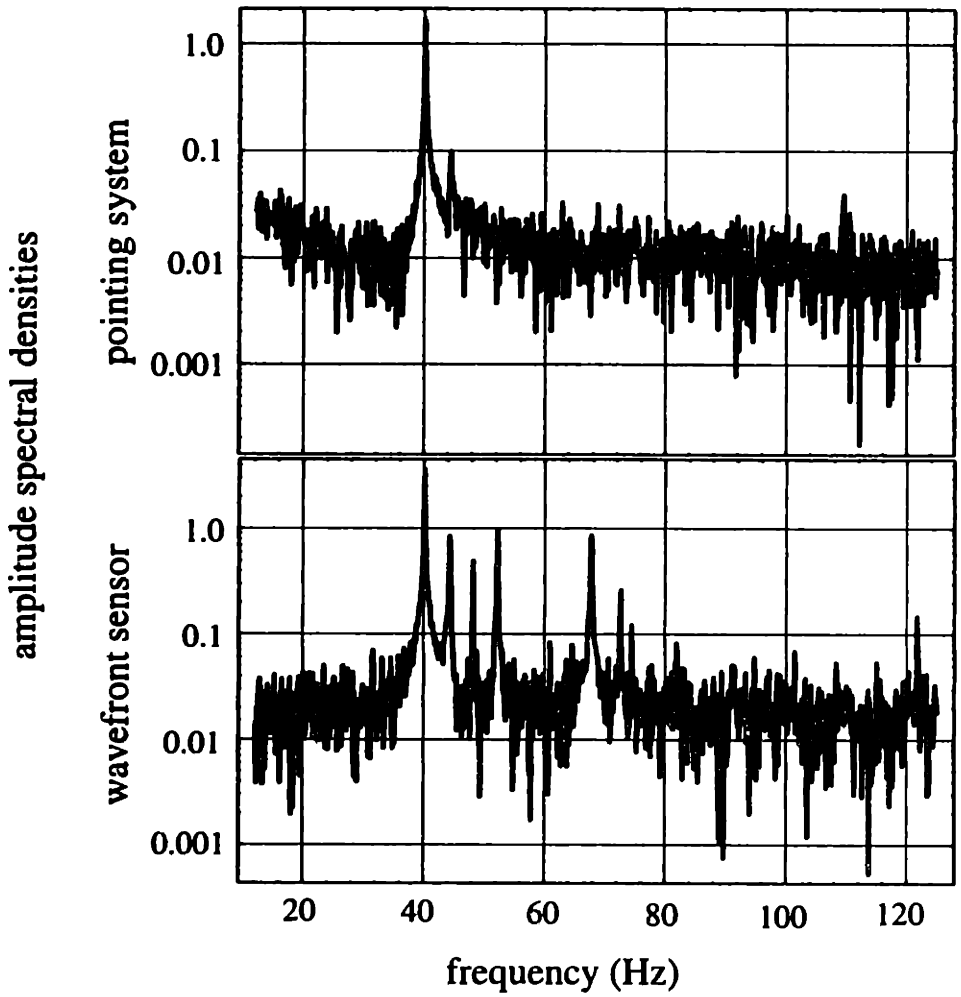

Figure 4.8: Fourier spectrum of pointing system signal for horizontal misalignments of the RM and the corresponding signal on WFS1. The peak at 40 Hz is due to horizontal misalignment of the recycling mirror, RM_x; RM_y appears at 44 Hz; $ITM1_y$ at 48 Hz; $ITM1_x$ at 52 Hz; $ETM1_y$ at 56 Hz; $ETM2_y$ at 59 Hz; $ETM1_x$ at 63 Hz; $ITM2_x$ at 67 Hz; $ITM2_y$ at 72 Hz; and $ETM2_x$ at 76 Hz.

horizontal signals on WFS1 at the reflection port. The Guoy phase shift is adjusted for greatest sensitivity to RM misalignments. Indeed, the strongest signal appears at 40 Hz, the frequency of the horizontal dither on the RM. As is to be expected, signals at the horizontal dither frequencies of ITM1 and ITM2 — 52 Hz and 67 Hz, respectively — are also pronounced. We note that the vertical dither of the RM at 44 Hz appears stronger than the pointing system readout indicates. This effect is too large to be explained solely by the

uncertainty in the orientation of the wavefront sensor heads with respect to the rotation axes of the mirror mounts. In two of the wavefront sensors (WFS1 and WFS2) a rather large asymmetry between horizontal and vertical signals is observed, that is, one of the signals is too large and the orthogonal signals are too small. This is also believed to be due to mode contamination. In fact, we measure the beam shape on these two detectors to be fairly elliptical (~20%), which would lead to corrections with opposite signs to horizontal and vertical signals. Furthermore, the signs of the effect are well correlated with the orientation of the elliptical beam. To decrease the uncertainty induced by this effect, we average over the horizontal and vertical signals when comparing the measured results with the predicted ones. We find that only 85% of the total input power actually couples into the interferometer (this effect is included in Table 4.4). The power reflection coefficient for the recycling cavity on resonance is expected to be near zero for the subcarrier, that is, the SC is almost critically matched. Instead, we measure a power reflection coefficient of 0.15, which implies that effective input power is 15% less than we expect. Coupling losses due to the measured 20% ellipticity of the input beam (~4%), coupling losses due to imperfect modematching (~3%) and the non-TEM_{00} component of the fiber output (~7%) account for this effect. We emphasize that this effect is not an intrinsic limitation of the wavefront sensing technique, but rather, an artifact of the quality of the optical components used in the FMI.

The signal amplitude V_{ij}^{ADC} on the i-th wavefront sensor due to the j-th degree of freedom is determined from the measured time series using the same down-conversion technique as for the pointing system. We then invert eqn. (94) to obtain the alignment sensitivity matrix:

$$\overline{A_{ij}} = \frac{V_{ij}^{ADC}}{2\varepsilon k_{PD} P_i J_0(\Gamma_i) J_1(\Gamma_i) Z_i \theta_j} \tag{100}$$

The RF and Guoy phase dependences are now included in the alignment sensitivity matrix elements $\overline{A_{ij}}$, that is,

$$\overline{A_{ij}} = A_{ij} cos(\eta - \eta_{ij}) cos(\Omega t + \phi_{ij}) \tag{101}$$

where we choose the RF phase of each detector to yield maximum signal for the diagonal terms, that is, $cos(\Omega t + \phi_{ii}) = 1$ after the down-conversion. Similarly, the Guoy phase at each detector is chosen to give maximum signal for the on-diagonal elements and to thus

minimize the uncertainty associated with the Guoy phase telescopes, that is, $cos(\eta + \eta_{ii}) = 1$.

The factor k_{PD} is a constant and depends only on the photodiode shape. The ADC gains are between 2 and 10 with negligible uncertainty of 0.1% (inferred from vendor specifications) and the photodetector quantum efficiency is measured to be $\varepsilon = 0.20 \pm 0.01$. Typical pointing system angles are found to be $\theta_j \approx a_j \times 10^{-7}$ rad $\pm$ 10%, where $0.5 \leq a_j \leq 3.0$ for the different angular degrees of freedom.

Since the laser light at each port is split among the different sensors, the power, P_i, is the input power multiplied by the fraction of power which is dedicated to the corresponding detector. The power levels at each detector are listed in Table 4.4:

DETECTOR	WFS1	WFS2	WFS3	WFS4	WFS5	WFS6
P_i (10^{-6} W)	399	342	486	967	727	208
σ_{P_i}/P_i	±0.06	±0.06	±0.06	±0.06	±0.06	±0.08

Table 4.4: Power levels at each detector and associated fractional uncertainties.

The transimpedance gains of the wavefront sensors, Z_i, are calibrated off-line and are listed in Table 4.5:

DETECTOR	WFS1	WFS2	WFS3	WFS4	WFS5	WFS6
Z_i (10^3 Ohm)	2389	2329	1681	1036	1037	1134
σ_{Z_i}/Z_i	±0.05	±0.05	±0.05	±0.10	±0.10	±0.10

Table 4.5: Transimpedance gain and fractional uncertainty for each wavefront sensor (the transimpedance gain for each wavefront sensor is averaged over all four quadrants).

The modulation depths are measured using a separate analyzer cavity and are listed in Table 4.6:

MODULATION FREQUENCY (MHZ)	32	39	59
Γ_i	0.423	0.253	0.205
σ_{x_n}/x_n	±0.05	±0.05	±0.10

Table 4.6: Modulation depth and fractional uncertainty for each modulation frequency.

4.5.2 Statistical errors

Both angular fluctuations due to acoustic excitations of the mirror mounts and the quantization noise of the ADCs are treated as statistical errors. Fluctuations are averaged out by the duration of the measurement (30 seconds) and quantization noise is suppressed by oversampling of the data. Statistical errors are determined from the power spectrum by estimating the noise level with data to the left and right of the Fourier peaks. The statistical uncertainty is typically under ±3%. Most of the measurement errors, then, are believed to be systematic.

4.5.3 Systematic errors

The measurement of the alignment sensitivity matrix elements is directly proportional to the parameters in eqn. (94) with the exception of the Guoy and RF phase deviations from the maximum, which have a cosinusoidal dependence. The matrix elements are also found to be insensitive to small changes in the geometric (g-) parameters of the beam: this is to be expected for a reasonably collimated beam as in the FMI where the divergence angle is small. On the other hand, the matrix elements are strongly influenced by changes in the optical fields and, therefore, rather sensitive to mirror reflectivities and losses, denoted by l. The dependence of the matrix elements on the interferometer losses is not straightforward — the losses effect the fields detected at the different ports differently — so we use the modal model to calculate the derivative of each matrix element with respect to optical losses in the interferometer. We find that loss in the recycling cavity, which reduces the recycling gain, is the most significant effect. The uncertainty in the measurement of the A_{ij} also depends on the fractional uncertainties in the quantum efficiency, ε; the input power, P_{IN}; the absolute angle, θ_j; the fraction of the light

detected on each wavefront sensor, f_i; the modulation depths, Γ; the transimpedance gains, Z_i; and the Guoy phase shift η_{ij}. The fractional uncertainty in each matrix element, A_{ij}, is given by

$$\frac{\sigma_{A_{ij}}}{A_{ij}} = \sqrt{\sum_n \left[\frac{1}{A_{ij}}\left|\frac{\partial A_{ij}}{\partial x_n}\right|\sigma_{x_n}\right]^2} \tag{102}$$

where $A_{ij}(x_n) = A(\varepsilon, P_{IN}, \theta_j, f_i, \Gamma_i, Z_i, \eta_{ij}, l)$, assuming that each of the x_n are independent of each other. $\sigma_{A_{ij}}$,the uncertainty in the value of each A_{ij}, depends only on the uncertainties, σ_{x_n}, in the parameters, x_n. From eqn. (94),

$$A_{ij} = \frac{V_{ij}^{ADC}}{\varepsilon P_i \theta_j \Gamma_i Z_i cos(\eta - \eta_{ij})} g(l) \tag{103}$$

where $g(l)$ is a non-analytical function of the losses. Eqn. (103) implies that

$$\frac{1}{A_{ij}}\left|\frac{\partial A_{ij}}{\partial x_n}\right| x_n = 1 \text{ for } x_n = \{\varepsilon, P_{IN}, \theta_j, f_i, \Gamma_i, Z_i\} \tag{104}$$

and

$$\frac{1}{A_{ij}}\frac{\partial A_{ij}}{\partial \eta} = tan(\eta - \eta_{ij}) \tag{105}$$

while $(1/A_{ij})(\partial A_{ij}/\partial l)$ are calculated using the modal model. The x_n can be divided into three categories based on how they contribute to the uncertainty in A: the uncertainties in ε, P_i, and θ_j are the same for all matrix elements and are summarized in Table 4.4 and the preceding text; uncertainties in Z_i and Γ_i are different for the three modulation frequencies and are listed in Table 4.5 and Table 4.6, respectively; uncertainties in $(\eta - \eta_{ij})$ and l are different for *each* matrix element and are given in corresponding matrix form in Table 4.7 and Table 4.8, respectively.

DETECTOR	$\sigma_{\eta_{ii}}$	RM	ITM1	ITM2	ETM1	ETM2
WFS1	8°	–0.01	±0.22	±0.22	0	0
WFS2	6°	±0.16	–0.01	–0.01	0	0
WFS3	16°	±0.13	–0.04	–0.04	0	0
WFS4	6°	±0.05	±0.01	±0.01	–0.01	–0.01
WFS5	6°	±0.06	±0.01	±0.01	-0.01	-0.01
WFS6	6°	±0.04	±0.04	±0.04	±0.03	±0.03

Table 4.7: Uncertainty in each matrix element due to the uncertainty in the Guoy phase shift of each telescope. For the on-diagonal terms we include second-order corrections.

DETECTOR	RM	ITM1	ITM2	ETM1	ETM2
WFS1	–0.11 +0.13	–0.11 +0.14	–0.11 +0.13	0	0
WFS2	–0.10 +0.13	–0.11 +0.14	–0.10 +0.13	0	0
WFS3	–0.18 +0.24	–0.18 +0.23	–0.18 +0.23	0	0
WFS4	–0.15 +0.20	–0.15 +0.19	–0.15 +0.19	–0.15 +0.19	–0.15 +0.19
WFS5	–0.06 +0.06	–0.06 +0.07	–0.06 +0.08	–0.07 +0.08	–0.06 +0.08
WFS6	–0.11 +0.18	–0.11 +0.17	–0.11 +0.17	–0.11 +0.17	–0.11 +0.17

Table 4.8: Uncertainty in each matrix element due to a ±0.01 uncertainty in the loss of the recycling cavity.

In Table 4.9 we list the measurement error associated with each matrix element.

DETECTOR	RM	ITM1	ITM2	ETM1	ETM2
WFS1	–0.17 +0.19	–0.28 +0.29	–0.27 +0.28	0	0
WFS2	–0.24 +0.25	–0.17 +0.19	–0.17 +0.19	0	0
WFS3	–0.28 +0.29	–0.24 +0.28	–0.24 +0.28	0	0
WFS4	–0.23 +0.26	–0.22 +0.25	–0.22 +0.25	–0.22 +0.25	–0.22 +0.25
WFS5	–0.18 +0.18	–0.17 +0.18	–0.17 +0.18	–0.18 +0.18	–0.18 +0.18
WFS6	–0.21 +0.24	–0.22 +0.24	–0.22 +0.24	–0.21 +0.24	–0.21 +0.24

Table 4.9: Total fractional error associated with each matrix element.

In the above analysis only the diagonal terms of the Jacobian matrix are considered. This is a valid approach given that we expect our errors to be independent, to first order.

Chapter 5

Results and Discussion

5.1 Measured alignment sensitivity matrix

The measured elements of the alignment sensitivity matrix are presented in Table 5.1; each one is averaged over the horizontal and vertical degrees of freedom. Also included are the modal model predictions based on the experimental conditions present during the measurement (see Table 2.7). The subcarrier signals (WFS1, WFS2 and WFS3) are insensitive to the ETM alignment degrees of freedom and both the predicted and measured signals are ≤0.01, which are rounded to zero in Table 5.1.

	PHASES		ANGULAR DEGREES OF FREEDOM				
PORT	RF	GUOY	RM	ITM1	ITM2	ETM1	ETM2
① refl, SC NR	I	152°	**-2.59**	0.34	0.43	0	0
			-3.50	0.40	0.45	0	0
② refl, SC NR	I	92°	-1.42	**0.76**	**0.78**	0	0
			-2.04	**0.67**	**0.75**	0	0
③ dark, SC	Q	168°	-0.67	**-2.77**	**2.98**	0	0
			0.30	**-2.89**	**3.14**	0	0
④ dark, CR	Q	80°	-1.01	14.8	-12.1	**15.5**	**-12.6**
			-0.74	11.4	-11.8	**13.6**	**-11.1**
⑤ refl, CR	I	87°	-2.05	3.65	3.67	**3.74**	**3.77**
			-3.28	3.28	3.62	**3.37**	**4.01**
⑥ rec, CR	I	140°	-20.7	32.4	32.8	**30.4**	**30.8**
			-25.0	**22.0**	27.3	**21.4**	**24.3**

Table 5.1: The calculated and measured (shaded rows) alignment sensitivity matrix elements.

Fig. 5.1 shows the significant elements of the alignment sensitivity matrix with their associated errors. The quantitative agreement between the modal model predictions and the measurement, evinced in Fig. 5.1, is an unequivocal validation of the model.

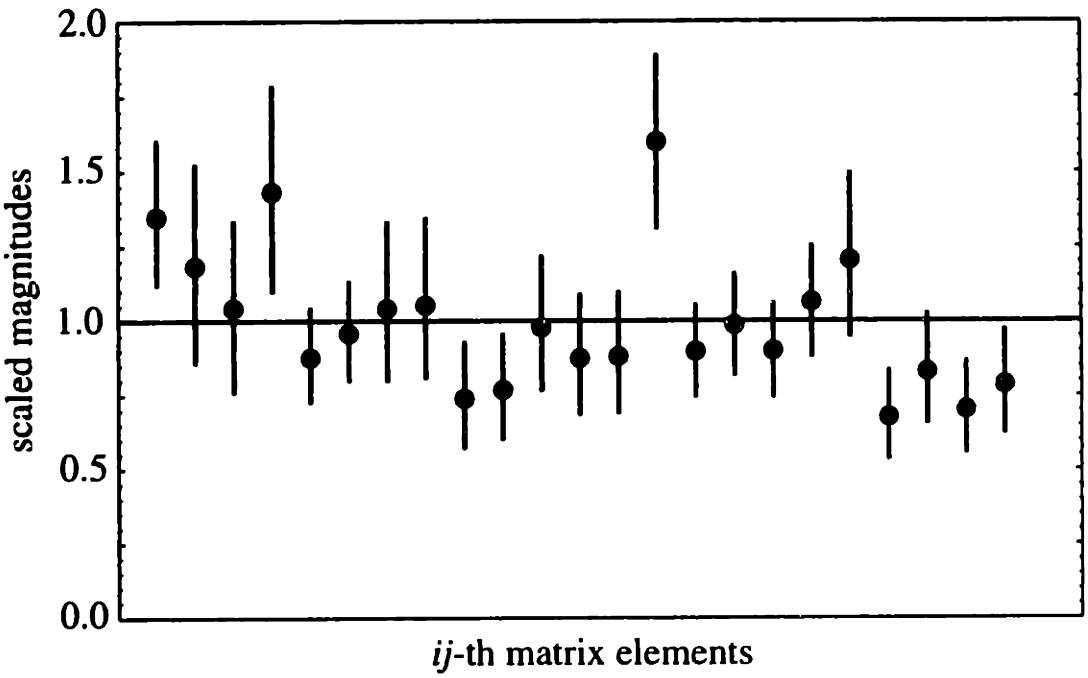

Figure 5.1: Non-zero matrix elements of the measured alignment sensitivity matrix. The measurements are scaled to the predicted values, which are normalized to 1.0.

The only (small) matrix element which is measured with the "wrong" sign is the RM signal on WFS3 at the dark port. Generally, RM signals are strongly suppressed at the dark port since they are not differential signals. However, any imperfection of the interferometer at the beamsplitter will appear at the dark port, which implies that this matrix element is expected to have an intrinsically larger uncertainty than the other (larger) elements of the alignment sensitivity matrix and does not represent a robust data point in the measurement. It should also be noted that this element does not carry important alignment information and is completely irrelevant for the servo design.

It is clear from Table 5.1 that the measured wavefront sensing signals give good discriminants for the individual angular degrees of freedom, that is, the alignment sensitivity matrix is clearly non-singular. By inverting the matrix and multiplying by the measured wavefront sensor signals, robust error signals for each individual mirror angle

are obtained. Fig. 5.2 shows the time evolution of two angular error signals with the power level in the recycling cavity when the angular servo system is switched on.

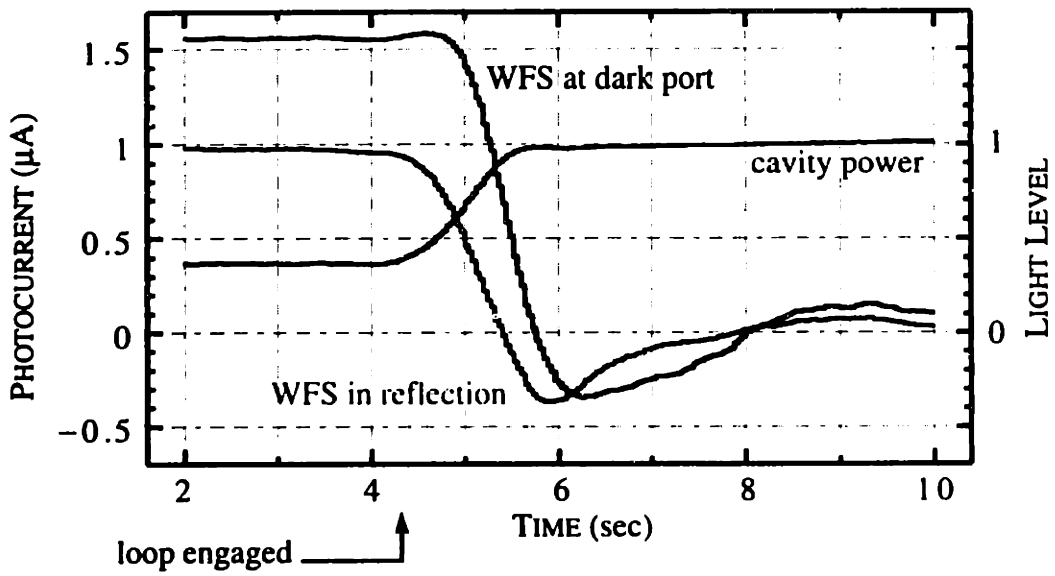

Figure 5.2: Closed loop control demonstration. The power in the recycling cavity is maximized when the alignment loops are engaged.

We see that the angular servo drives the error signals to zero and at the same time the power in the recycling cavity increases, indicative of improved alignment. During our dither measurements, the angular servo system for all degrees of freedom is used to keep the interferometer aligned. The bandwidth of this servo loop is just a few Hertz so that it does not interfere with the angular dither frequencies at 40 Hz or higher.

5.2 Applications to LIGO

In the following sections we use the modal model as a simulation tool to study the effects of small misalignments in the long baseline LIGO detector and to design a wavefront sensing scheme for it.

First we highlight some features of the LIGO optical design, in particular where it differs from the FMI, which we have studied in detail in the preceding chapters. The most significant difference is, of course, the change in the macroscopic interferometer lengths. In LIGO each arm cavity is 4 km long, while the recycling cavity is typically between 6 and 12 m long (to be decided). The interferometer lengths are bounded by the vacuum

envelope. This is also true for the *input mode cleaner*, a Fabry-Perot cavity between the laser and the recycling mirror, which acts as a spatial filter for the light incident on the interferometer. Since all modulation frequencies must pass through the mode cleaner (that is, they must be resonant in the mode cleaner) and most of them must resonate in the recycling cavity, the mode cleaner and the recycling cavity lengths are chosen to satisfy these multiple resonance conditions. The asymmetry is chosen to optimally couple the resonant sidebands out the antisymmetric port.

The disparity in the lengths of the recycling and the arm cavities results in a nearly degenerate recycling cavity (where all higher-order spatial modes occur at the same frequency as the fundamental or are degenerate with it). This could be circumvented by introducing a strongly focussing element in the recycling cavity, but is not currently planned for in LIGO. An unfortunate consequence of the degeneracy of the recycling cavity is that it does not have good filtering properties for the light circulating in the interferometer, except for the carrier, which has a double resonance in both the recycling and the arm cavities. Furthermore, from our discussion in Section 2.4.3, we recall that the wavefront sensing technique cannot ordinarily be used to distinguish misalignment of the input and rear mirrors of a degenerate cavity (since the Guoy phase shift $\eta = tan^{-1}(z/z_0) \sim 0$ when $z \ll z_0$). In Section 5.2.2 below, we see that the double resonance of carrier is a special case and can be used to obtain distinct wavefront signals for RM and ITM_C misalignments.

We also note that the laser source planned for LIGO is a solid state Nd:YAG laser at 1.064 μm.

5.2.1 Effects of misalignment

There are a number of reasons why misalignment is detrimental to the performance of the interferometer. The gravitational wave sensitivity can be degraded by *static misalignment*. Misalignment of the optical components of the interferometer with respect to the incident TEM_{00} laser light causes light in the fundamental mode of the interferometer to be coupled into higher-order modes. This reduces the amount of power circulating in the arm cavities due to diminished coupling of light into them, resulting in reduced phase sensitivity. Higher-order modes leaking out the signal extraction port of the interferometer result in increased photocurrent and shot-noise, and effectively lower the

contrast of the interferometer, which, in turn, lowers the light power incident on the arm cavities. In both cases the signal-to-noise ratio of the gravitational wave signal readout is compromised. Furthermore, since misalignments can affect the two arms independently, there is less common mode rejection of fluctuations in the laser power, laser frequency and input beam jitter for differential misalignments. *Beam jitter coupling* can be a significant source of phase noise. The modal model is used to study the effects of misalignment in the long baseline LIGO interferometer and the results presented in this chapter draw heavily upon the work of Daniel Sigg [9], [33], [34] and Peter Fritschel [35].

For the calculations involving the LIGO interferometer, the interferometer and modulation parameters used are listed in Table 5.2 and Table 5.3, respectively. Since the subcarrier is not used to probe the gravitational wave signal (L_D), most of the results presented here use the modified single carrier modulation scheme discussed in Section 2.2.2. Parameters for the subcarrier in Table 5.3 are not fully optimized.

PARAMETER	UNIT	ARM (ITM)	ARM (ETM)	REC (RM)
LENGTH	m	3999.01		9.38
ASYMMETRY	m	0.21		
POWER TRANSMISSION	%	3.0	0.0015	2.44
LOSSES	ppm	50	50	60
RADII OF CURVATURE	m	−14571	7400	−9999
WAVELENGTH	μm	1.06		

Table 5.2: Interferometer parameters.

MODULATION PARAMETER	FREQ. SHIFT (MHZ)	DEPTH (Γ)
CARRIER	0.000	1.0 W
CARRIER RESONANT SB (CSB)	23.971	0.45
CARRIER NON-RESONANT SB (CNR)	35.956	0.045
SUBCARRIER	727.121	1.0 W
SUBCARRIER RESONANT SB (SCSB)	15.980	0.45
SUBCARRIER NON-RESONANT SB (SCNR)	43.946	0.045

Table 5.3: Modulation parameters.

Degradation of gravitational wave sensitivity

If $S(\Delta L)$ is the down-converted signal at the dark port as a function of the differential arm cavity length ΔL, the gravitational wave sensitivity can be written as:

$$S_{sens} = \frac{d}{d\Delta L} S(\Delta L) \tag{106}$$

If S_{sens} is a also function of $\hat{\theta}$, the 5-component vector of the horizontal (vertical) misalignment angles, then $S_{sens}(\hat{\theta})$ can be Taylor expanded to give:

$$S_{sens}(\hat{\theta}) \approx S_{sens}(0) + \sum_i \frac{\partial}{\partial \theta_i} S_{sens}\theta_i + \frac{1}{2}\sum_{ij} \frac{\partial^2}{\partial\theta_i \partial\theta_j} S_{sens}\theta_i\theta_j + \ldots \tag{107}$$

This sensitivity has a maximum if the interferometer is perfectly aligned and is hence only second-order sensitive to misalignment. For a misaligned system, it can be approximated by:

$$S_{sens}(\hat{\theta}) = S_{sens}(0)\left[1 + \frac{1}{2}\hat{\theta} H \hat{\theta}\right] \tag{108}$$

where the Hessian matrix, H, given by

$$H_{ij} = \frac{\partial^2}{\partial\theta_i \partial\theta_j} S_{sens}(\hat{\theta}) \tag{109}$$

is (upto a constant) the inverse of the covariance matrix C:

$$C = 2H^{-1} \tag{110}$$

Diagonalizing the covariance matrix gives the eigenvectors u_i which are the axes of the variance-ellipsoid (in the 5 dimensional angular space) and the corresponding eigenvalues σ_i^2 which are the square of the axes lengths (variances). Using the new basis u_i to express the misalignment angles ψ_i the relative loss of sensitivity δ can be easily calculated by:

$$\delta = -2\sum_i \left(\frac{\psi_i}{\sigma_i}\right)^2 \tag{111}$$

where the factor of 2 comes from the fact that we have so-far neglected the vertical misalignment angles. If the rms misalignment angles, $\Delta\theta_{rms}$, are equal for all degree of freedoms, one obtains

$$\Delta\theta_{rms} = \sqrt{\frac{-\delta}{2\sum_i \frac{1}{\sigma_i^2}}} \tag{112}$$

The signal-to-noise ratio of the gravitational-wave detection at the dark port is written by replacing the signal sensitivity S_{sens} in equation (106) with the signal-to-noise sensitivity:

$$\left(\frac{S}{N}\right)_{sens} = \frac{\frac{d}{d\Delta L}S(\Delta L)}{\sqrt{P_{cr} + \frac{3}{2}P_{sb}}} \tag{113}$$

where P_{cr} and P_{sb} are the average light intensities of the carrier and the sidebands leaking out of the dark port (predominantly stored in the sidebands). The factor of 3/2 comes from the formulation for non-stationary shot noise [36].

The misalignment angles used for the calculations are linear combinations of the individual mirror angles θ_i, as indicated in eqn. (93) (see Section 3.5.1 for the sign convention of the misalignment angles).

The modal model is used to calculate the covariance matrix, which is diagonalized for the signal-to-noise ratio of the gravitational wave readout. The directions of the ellipsoid axes u_i and the variances σ_i^2 are given in Table 5.4. The eigenvalues are a measure of the degree of misalignment which degrades the gravitational wave sensitivity by 100%

EIGENVALUE	EIGENVECTOR (ELLIPSOID AXIS)				
σ_i^2 (θ_D^2)	*RM*	ITM_C	ITM_D	ETM_C	ETM_D
–6.39	**–0.537**	**–0.747**	0.000	**0.393**	0.000
–0.834	**0.231**	**0.317**	0.000	**0.920**	0.000
–0.116	0.000	0.000	**0.909**	0.000	**–0.421**
–0.0006	**0.811**	**–0.584**	–0.002	–0.002	–0.005
–0.0005	0.005	–0.004	**0.417**	0.000	**0.909**

Table 5.4: Eigenvalues (variances) and eigenvectors (direction of the axes of the variance ellipsoid) of the covariance matrix describing the degradation of the gravitational wave sensitivity due to misalignment. The σ_i are measured in units of the beam divergence angle in the arm cavities $\theta_D = w_0/z_0 \approx 9.65\times10^{-6}$ rad.

($\delta = 1$), while the eigenvectors represent the combination of individual mirror angles which lead to that degree of misalignment. Larger values of σ_i^2 indicate greater insensitivity to that degree of freedom. The most sensitive degree of freedom, then, is a differential misalignment of the ETMs with a differential tilt of the ITMs in the opposite direction, as shown in Fig. 5.3(b). This happens because all the TEM_{10} mode produced differentially in each arm efficiently exits the antisymmetric port and gravitational wave sensitivity is reduced due to *shot noise production*. The next most sensitive misalignment degree of freedom is a common rotation of the ITMs with an opposite rotation of the RM (see Fig. 5.3(c)). In the degenerate recycling cavity, the build-up of the resonant sideband is rapidly reduced by misalignment, so the sideband power exiting the antisymmetric port decreases. This lead to loss of gravitational wave sensitivity due to *signal reduction*. The least sensitive misalignment is the one where all mirrors are rotated in the same direction, which simply reduces the coupling of light power into the interferometer. In Fig. 5.3 the dominant mirror misalignments represented by each eigenvector in Table 5.4 are illustrated. We also note that the alignment of the ETM mirrors is as critical as the alignment of the ITM and RM mirrors. If the alignment can done equally well for all angular degrees of freedom and if the loss of sensitivity to gravitational waves must not exceed 0.5%, for example, then eqn. (112) implies that each rms misalignment angle should be smaller than $\Delta\theta_{rms} = 8.0\times10^{-9}$ rad.

A negative sign of the eigenvalue indicates a maximum, whereas a positive sign would

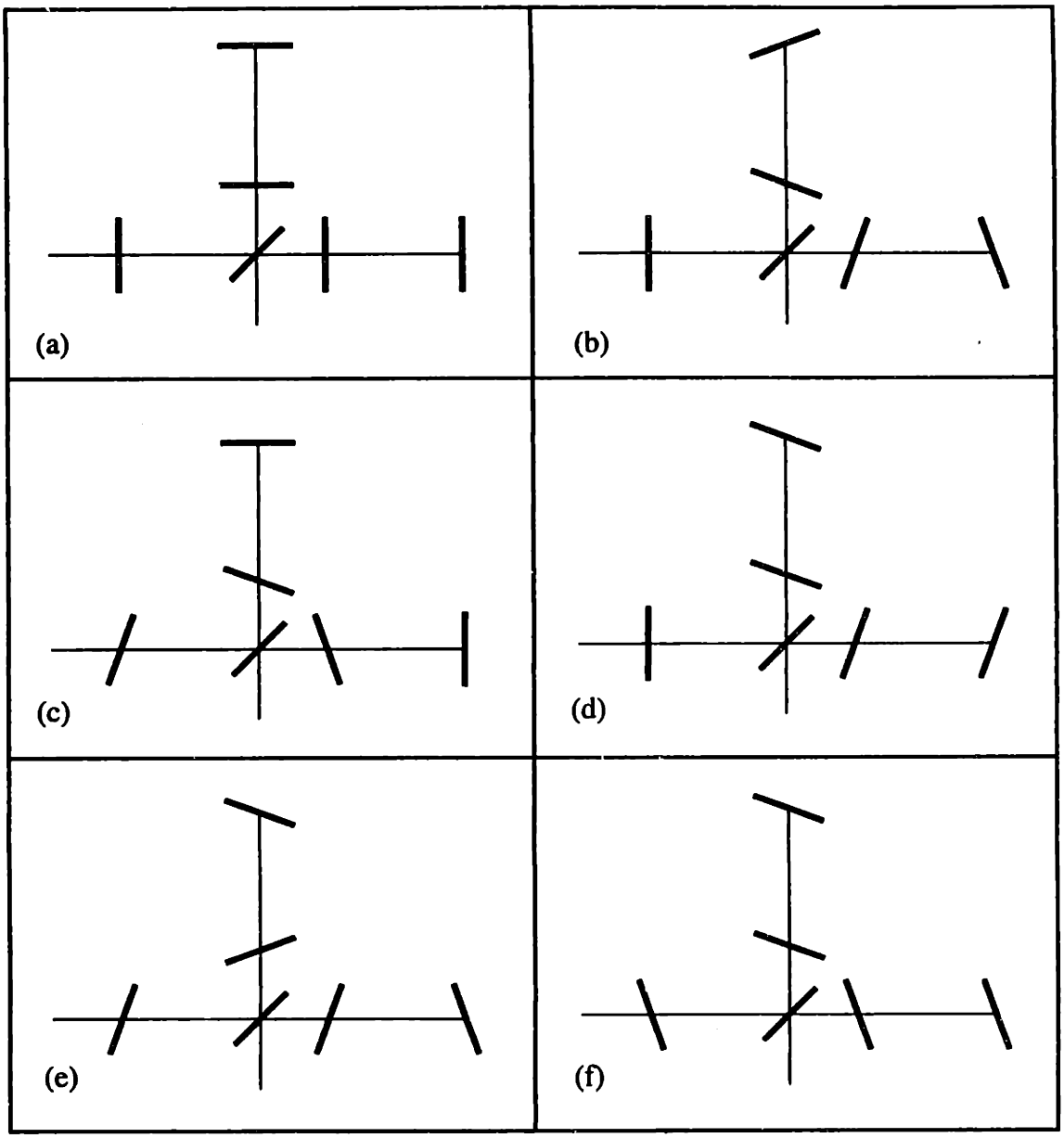

Figure 5.3: Combinations of mirror misalignment which degrade the gravitational wave sensitivity: (a) perfectly aligned; (b) $\sigma^2 = -0.0005$ (most sensitive); (c) $\sigma^2 = -0.0006$; (d) $\sigma^2 = -0.116$; (e) $\sigma^2 = -0.834$; (f) $\sigma^2 = -6.39$ (least sensitive).

indicate a minimum. For the signal-to-noise ratio all eigenvalues are negative, implying that the perfectly aligned case is a true maximum of gravitational wave sensitivity. For the shot noise alone this is not true, that is, for some misalignments the power at the dark port increases and for others it decreases.

Input beam jitter

So far we have neglected the effects of a misaligned beamsplitter or tilted and shifted input laser beam, since both the misalignment of the beamsplitter and the input beam can be expressed as linear combinations of misalignments of the interferometer mirrors.

Input beam jitter can, however, couple directly into the gravitational wave readout if the interferometer mirrors have a static misalignment [35]. For a perfectly aligned interferometer this is a second-order effect, but when the interferometer mirrors are misaligned, the length error signals become first-order sensitive to the direction of the input beam. It is a very small effect for common misalignment of the test masses and the recycling mirror and significantly more pronounced for the differential misalignment of the test masses. The reason for this can be understood in the modal picture. All the power in the TEM_{10} mode excited by differential misalignments of the interferometer mirrors is coupled directly out the antisymmetric port. The TEM_{10} component of the sideband of the input beam also exits the dark port since the recycling cavity is highly degenerate. The photocurrent on the length detector at the dark port is due the superposition of the carrier beating against the sidebands for each $TEM_{m,n}$ mode, that is,

$$i_d \propto \sum_{m,n} [(E_0^{m,n*} E_+^{m,n} + E_0^{m,n} E_-^{m,n*}) exp(i\Omega t + \eta_{m,n}) + CC] \qquad (114)$$

An important concern, then, is the effect of input beam direction fluctuations in the gravitational wave detection band, at 150 Hz[1], for example. This question is addressed by expressing the TEM_{10} component of the input beam (due to jitter) as audio frequency sidebands imposed on the carrier and RF sidebands in the modal model. We find that the transfer function between the gravitational wave demodulation signal at audio frequencies and the input beam tilt or shift is remarkably flat out to 1 kHz [35]. This is perfectly plausible given that the TEM_{10} mode does not resonate in the arm cavities and is, therefore, not affected by the double cavity pole.

Since the beam jitter coupling to the gravitational wave readout does not have a strong frequency dependence in the signal band, we use the DC modal analysis to determine the sensitivity to input beam misalignment. The gravitational wave induced signal at the dark port can be written as:

1. Near the best gravitational wave sensitivity for LIGO.

$$GWS_{jitter}(\alpha, x_0, \Theta) = \frac{1}{2}\sum_i \Theta_i(B_i\alpha + C_i x_0) \qquad (115)$$

where x_0 is the lateral shift of the input beam (in units of the beam waist size) and α is the input beam tilt (in units of the beam divergence angle). Table 5.5 lists the equivalent differential arm length change for the constants B_i and C_i.

	ANGULAR DEGREE OF FREEDOM				
INPUT BEAM	ETM_D	ITM_D	ETM_C	ITM_C	RM
TILT (B_i in m/rad^2)	**-20.60**	**-9.34**	$< 10^{-3}$	$< 10^{-3}$	$< 10^{-2}$
SHIFT (C_i in /rad)	**-10.9×10^{-4}**	**-5.16×10^{-4}**	$< 10^{-7}$	$< 10^{-7}$	$< 10^{-7}$

Table 5.5: Gravitational wave sensitivity to beam jitter and misalignment. The values are in units of meters of differential arm length change per square radian for B_i and per radian per meter for C_i.

If we require that the gravitational wave signal at about 150 Hz due to beam jitter is smaller than 10^{-20} m/$\sqrt{\text{Hz}}$ and if we assume that the alignment servo system controls the angular degrees of freedom to within 10^{-8} rad rms at low frequencies (<10Hz), then the beam jitter at 150 Hz has to be smaller than 6×10^{-14} rad/$\sqrt{\text{Hz}}$ for both tilt directions and smaller than 10^{-9} m/$\sqrt{\text{Hz}}$ for the shifts in x and y.

5.2.2 Implementation of an automatic alignment system

In this section we propose a practical implementation of the wavefront sensing scheme for a long baseline LIGO interferometer. The alignment sensitivity matrices for two modulation configurations are presented along with a discussion of the relevant signals and estimated shot noise limits.

Alignment sensitivity matrix

Using the parameters in Table 5.2 the calculated alignment sensitivity matrix is given in Table 5.6. The ij-th matrix element denotes the RF amplitude of the signal on the i-th wavefront sensor due to misalignment of the j-th degree of freedom. The values of A_{ij} are scaled by the corresponding RF modulation depths and are given in units of divergence

angle.

	PHASES		ANGULAR DEGREES OF FREEDOM				
PORT	RF	GUOY	*RM*	ITM_C	ITM_D	ETM_D	ETM_C
CARRIER SIGNALS							
1 reflection, CNR	I	0°	**–1.84**	0	0	0	0
2 reflection, CSB	I	90°	**–9.60**	**6.21**	0	0	–0.5
3 reflection, CSB	Q	145°	0	0	**–1.37**	0.05	0
4 dark port, CSB	Q	90°	0	0	**–11.4**	**–25.0**	0
5 reflection, CNR	I	90°	0	**–0.92**	0	0	**–2.01**
SUBCARRIER SIGNALS							
1 reflection, SCNR	I	0°	**–136**	96.5	0.1	0	0
2 reflection, SCNR	I	0°	136	**–96.5**	0	0	0
3 dark port, SCSB	Q	0°	1.05	–0.66	**–10.4**	0	0

Table 5.6: Possible alignment sensitivity matrix for LIGO.

An interesting feature of this matrix is that the two wavefront sensors, WFS2 and WFS4, measure approximately the same linear combination of misalignment angles which most dramatically reduce the signal-to-noise ratio of the gravitational wave readout (lowest rows in Table 5.4). Due to the high degeneracy of the recycling cavity, the non-resonant sidebands are absolutely essential to distinguish misalignment of the recycling mirror from a common ITM misalignment. It also a better way to detect the common ETM misalignment which is usually a rather small effect when measured with other wavefront sensors. The use of the non-resonant sideband to distinguish RM and common ITM tilts relies on a subtle coupled cavity effect. Ordinarily, a highly degenerate single cavity produces similar signals for input and the rear mirror misalignments and prospects for fully decomposing the misalignment signals in the LIGO recycling cavity may look bleak. A coupled cavity, however, has the unique property that a tilt of the middle mirror changes the resonant eigenmode in the rear cavity, so the light reflected from the middle mirror (rear cavity) is laterally shifted with respect to the incident beam. From eqns. (39) and (41), we recall that there is an additional π phase shift for a tilted beam relative to a laterally displaced beam, which then separates the signals from the RM and the ITMs in Guoy phase.

For comparison we also include the matrix elements for alignment of the near Michelson degrees of freedom (RM and ITMs) using the frequency-shifted subcarrier. We see that the non-resonant sideband of the subcarrier cannot be used to distinguish the *RM* and ITM_C misalignments, since the subcarrier does not resonate in the arm cavities, further confirming that the double resonance is essential for decoupling these degrees of freedom in the highly degenerate recycling cavity.

Estimated shot noise limited sensitivity

Assuming perfect contrast and no scattering into higher-order modes, the power levels of the various fields circulating in the interferometer are listed in Table 5.7. We do not include input power levels for the frequency shifted subcarrier since they are expected to be less than one-tenth that of the carrier; the latter dominate the shot noise budget.

LIGHT	INPUT	DARK PORT	REFL PORT	REC CAVITY	ARM CAVITY
CARRIER	5.42	0	0.17	306	20000
RESONANT SIDEBAND	0.577	0.497	0.056	11.4	0.04
NR SIDEBAND	0.0061	$< 10^{-5}$	0.0061	$< 10^{-4}$	$< 10^{-6}$

Table 5.7: Light Intensities. All numbers are in Watts for a 6.0 W input beam, assuming perfect contrast.

Having determined the dominant light intensities at the extraction ports, we calculate the shot noise which limits the wavefront sensing. The rms photocurrent due to shot noise in the detector, assuming stationarity, is

$$i_{SN} = \sqrt{2q\varepsilon P_i f_{BW}} \tag{116}$$

where q is the elementary charge, ε the photodetector efficiency, P_i the light level at the extraction port and f_{BW} is the bandwidth of the detector. Multiplying the signal in eqn. (50) by the quantum efficiency, we get the photocurrent due to misalignment on the i-th detector:

$$i_{WFS} = 2\varepsilon J_0(\Gamma)J_1(\Gamma)P_i\sum_j A_{ij}\Theta_j cos(\eta - \eta_{ij}) \tag{117}$$

Assuming that the Θ_j have an rms value Θ_{rms} and that they are independent, equating i_{SN} to i_{WFS} leads to the shot noise limited detection angles:

$$\Theta_i^{SN} = \frac{1}{J_0(\Gamma)J_1(\Gamma)}\sqrt{\frac{q(P_i/P)}{2\varepsilon P f_{split}}}\frac{1}{|A_i|} \tag{118}$$

where $|A_i|$ is the absolute value of the signal amplitude for the corresponding wavefront sensor:

$$|A_i| = \sqrt{\sum_j A_{ij}^2 cos^2(\eta - \eta_{ij})}, \tag{119}$$

The shot noise limited detection angles are listed in Table 5.8. We assume that the contrast of the interferometer is perfect, that the fraction of light split-off for each wavefront sensor is $f_{split} = 10^{-2}$ at each extraction port, that the input laser intensity is $P = 6.0$ W and that the photodetector efficiency for Nd:YAG laser light is $\varepsilon = 0.39$ A/W.

WAVEFRONT SENSORS				
1	**2**	**3**	**4**	**5**
37×10^{-15}	0.7×10^{-15}	6.1×10^{-15}	0.44×10^{-15}	61.6×10^{-15}

Table 5.8: Shot noise limited detection angles. The values are given in rad/$\sqrt{\text{Hz}}$.

It can be seen from Table 5.8 that the shot noise limited detection angles are tiny compared to the 10^{-8} rad rms misalignment tolerance determined above.

5.3 Final remarks

To summarize, a table-top scale fixed mirror interferometer using the optical configuration planned for LIGO was used to experimentally determine the discriminants for misalignment of the interferometer mirrors and to use these discriminants for closed loop control of the mirror angles. The wavefront sensing discriminants were extracted using a heterodyne phase modulation technique. A model based on mode decomposition of the field was developed and implemented to calculate the coefficients of the sensitivity matrix for all ten angular degrees of freedom. Agreement between the predicted values

and the measured discriminants was good, with an average measurement error of ±20%.

The modal model presented here has played a pivotal role in our understanding of the effects of misalignment in gravitational wave detectors, the mechanisms by which the gravitational wave sensitivity of the detector is compromised and methods of extracting alignment signals which are sensitive to particular degrees of freedom at the various ports of the interferometer. Specifically, the modal model was used to study the effects of misalignment in a long baseline LIGO interferometer and to design an automatic alignment system for LIGO. This study resulted in the imposition of stringent requirements on the degree of misalignment which can be tolerated in LIGO: $\sim 10^{-8}$ rad rms per mirror angle and $\sim 10^{-14}$ rad/$\sqrt{\text{Hz}}$ for input beam jitter at 150 Hz. A robust set of wavefront sensor discriminants which distinguish all angular degrees of freedom were also calculated for the LIGO interferometer.

With an eye to the future, there is much potential in the modal model to study misalignments and more general optical distortions in interferometers. The modal model implementation in this work utilized only the first higher-order modes of the field (TEM_{10} and TEM_{01}), which is adequate for small misalignments. To study the effects of larger misalignments, higher-order modes must be included in the mode expansion [37]. Effects such as mode matching and astigmatism excite — to first order — the second higher-order modes and can be studied with the TEM_{20}, TEM_{02} and TEM_{11} modes [38]. Another limitation of the present model is that only steady-state optical fields are analyzed. If the dynamics of the system are to be understood, the temporal dependence of the fields must be included [39]. Implementation of these extensions of the modal model are underway and will be useful for the study of the dynamic behavior of near-resonant and non-resonant interferometer fields. In addition, advanced detector configurations, such as a dual-recycled interferometer [40], can also be studied using the modal model.

We conclude that the wavefront sensing technique is well understood, both theoretically and experimentally, and that this technique is feasible for closed loop servo control of complex interferometers.

References

[1] A. Einstein, *Preuss. Akad. Wiss. Berlin, Sitzungsberichte der Physikalisch-mathematischen Klasse*, 688 (1916).

[2] K.S. Thorne, *"Gravitational Radiation"* in *300 Years of Gravitation*, S. W. Hawking and W. Israel (eds.), Cambridge University Press, Cambridge, 330 (1987).

[3] G. E. Moss, L. R. Miller, and R. L. Forward, Appl. Opt. **10**, 2495 (1971).

[4] R. Weiss, *Quarterly Progress Report of the Research Laboratory of Electronics of the Massachusetts Institute of Technology*, **105**, 54 (1972).

[5] R. W. P. Drever, in *Gravitational Radiation*, N. Deruelle and T. Piran (eds.), North Holland, Dordrecht, 320 (1983).

[6] A. Abramovici, W.E. Althouse, R.W.P. Drever, Y. Gürsel, S. Kawamura, F.J. Raab, D. Shoemaker, L. Sievers, R.E. Spero, K.S. Thorne, R.E. Vogt, R. Weiss, S.E. Whitcomb, and M.E. Zucker, Science **256**, 325 (1992).

[7] See, e.g., A. Yariv, *Optical Electronics*, Saunders College Publishing (1991).

[8] Y. Hefetz and N. Mavalvala, Proc. Seventh Marcel Grossman Meet. on Gen. Rel. (1994).

[9] D. Sigg, *"Modal Model Update 2: Gravitational Wave Sensitivity to Angular Misalignment"*, LIGO Technical Note, LIGO-T960114-00-D (1996).

[10] P.Fritschel, *"Alignment Sensing/Control Design Requirements Document"*, LIGO Technical Note, LIGO-T952007-03-I (1996).

[11] G. Gonzàlez, *"ASC: Environmental Input to Alignment Noise"*, LIGO Technical Note, LIGO-T960103-00-D (1996).

[12] E. Morrison, B.J. Meers, D.I. Robertson, and H. Ward, Appl. Opt. **33**, 5037 (1994).
E. Morrison, B.J. Meers, D.I. Robertson, and H. Ward, Appl. Opt. **33**, 5041 (1994).

[13] Y. Hefetz, N. Mavalvala, and D. Sigg, *"Principles of Calculating Alignment Signals in Complex Resonant Optical Interferometers"*, accepted for publication in J. Opt. Soc. Am. **B** (Nov. 1996).

[14] For an excellent introduction to interferometric gravitational wave detectors, see P. R. Saulson, *Fundamentals of Gravitational Wave Detectors*, World Scientific Publishing Co., Singapore (1994).

[15] B. J. Meers, Phys. Lett. A **142**, 465 (1989).

[16] A. Schenzle, R. DeVoe and G. Brewer, Phys. Rev. A **25**, 2606 (1982).

[17] R.W.P. Drever, J.L. Hall, F.V. Kowalski, J. Hough, G.M. Ford, A.J. Munley and H. Ward, Appl. Phys. B **31**, 97 (1983).

[18] M.W. Regehr, F.J. Raab, and S.E. Whitcomb, Opt. Lett. **20**, 1507 (1995).

[19] M. W. Regehr, "*Signal Extraction and Control for an Interferometric Gravitational Wave Detector*", Ph.D. dissertation (California Institute of Technology, Pasadena, CA, 1995).

[20] J. A. Giaime, "*Studies of Laser Interferometric Design and a Vibration Isolation System for Interferometric Gravitational Wave Detectors*", Ph.D. dissertation (Massachusetts Institute of Technology, Cambridge, MA, 1996).

[21] L. Schnupp, Max Planck Institute for Quantum Optics, Garching, Germany, private communication (1986).

[22] C.N. Man, D. Shoemaker, M. Pham Tu, and D. Dewey, Phys. Lett. A **148**, 8 (1990).

[23] D.Z. Anderson, Appl. Opt. **23**, 2944 (1984).

[24] N. Sampas, and D.Z. Anderson, Appl. Opt. **29**, 394 (1990).

[25] A.E. Siegman, "*Lasers*", University Science, California (1986).

[26] J. Vinet, P. Hello, C.N. Man and A. Brillet, J. Phys. I France **2**, 1287 (1992).

[27] P. Saha, "*Fast Estimation of Transverse Fields in High Finesse Optical Cavities*", to be submitted in J. Opt. Soc. Am. A.

[28] An introduction to group theory can be found, e.g., in: H. Georgi, *Lie Algebras in Particle Physics*, Benjamin/Cummings Publ. Co., California (1982).

[29] P. Fritschel, G. Gonzales, N. Mavalvala, D. Shoemaker, D. Sigg, and M. Zucker, "*Alignment of a long baseline gravitational wave interferometer*", in preparation.

[30] D. Sigg, "*Wavefront Sensor*", LIGO Technical Note, LIGO-T960111-A-D (1996).

[31] W. H. Press, S. A. Teukolsky, W. T. Vetterling, and B. P. Flannery, *Numerical Recipes in C: The Art of Scientific Computing*, Cambridge University Press (1992).

[32] G. F. Franklin, J. D. Powell, and A. Emami-Naeini, *Feedback Control of Dynamic Systems*, Addison-Wesley Publishing Company, Inc. (1994).

[33] D. Sigg, "*Modal Model Update 1: Interferometer Operators*", LIGO Technical Note, LIGO-T960113-00-D (1996).

[34] D. Sigg, "*Modal Model Update 3: Small Angle Regime*", LIGO Technical Note, LIGO-T960115-00-D (1996).

[35] P. Fritschel, "*Misalignment-Beam Jitter Coupling in LIGO*", LIGO Technical Note, LIGO-T960xxx (1996).

[36] T. M. Niebauer, R. Schilling, K. Danzmann, A. Rüdinger, and W. Winkler, Phys. Rev. A **43**, 5002 (1991).

[37] D. Sigg, "*Modal Model Update 5: Large Angle Regime*", LIGO Technical Note, LIGO-T960117-00-D (1996).

[38] D. Sigg, "*Modal Model Update 4: Mode Mismatch*", LIGO Technical Note, LIGO-T960116-00-D (1996).

[39] R. Beausoleil, "*Spatiotemporal Model of the LIGO Interferometer*", private communication (1996).

[40] B. J. Meers, Phys. Rev. D **38**, 2317 (1988).

Appendix A Formulae for mode decomposition theory

In the following appendix the detailed equations of the modal model formalism are worked out using the Hermite-Gaussian representation.

A.1 Formulae

In the paraxial approximation, the solutions to the scalar wave equation in one dimension can be expressed as a superposition of Hermite-Gaussian modes [25]:

$$U_m(x,z) = \left(\frac{2}{\pi}\right)^{1/4}\left(\frac{1}{2^m m! w(z)}\right)^{1/2} H_m\left(\frac{\sqrt{2}x}{w(z)}\right) \exp\left(-x^2\left(\frac{1}{w(z)^2}+\frac{ik}{2R(z)}\right)\right)\exp\left(i\left(m+\frac{1}{2}\right)\eta(z)\right) \tag{A.1}$$

where the z-axis points in the beam propagation direction and where $\eta(z)$, $w(z)$ and $R(z)$ are the mode-dependent Guoy phase shift, the spot size and the curvature of the phase front at position z, respectively,

$$\eta(z) = tan^{-1}\left(\frac{z}{z_0}\right),\quad w(z) = w_0\sqrt{1+\left(\frac{z}{z_0}\right)^2} \quad \text{and} \quad R(z) = z+\frac{z_0^2}{z} \tag{A.2}$$

and the Rayleigh length, z_0, is given by $z_0 = \pi w_0^2/\lambda$ with w_0 the waist size. $H_m(x)$ is the Hermite polynomial of order m. The following relations are used repeatedly in the calculations which follow:

$$\int_{-\infty}^{\infty} U_m^{\dagger}(x,z)\, U_n(x,z)dx = \delta_{mn} \tag{A.3a}$$

$$2xH_m(x) = H_{m+1}(x) + 2mH_{m-1}(x) \tag{A.3b}$$

$$\frac{d}{dx}H_m(x) = 2mH_{m-1}(x) \tag{A.3c}$$

$$\int_{-\infty}^{\infty} U_m^{\dagger}(x,0)\frac{H_i(\sqrt{2}x/w_0)}{H_k(\sqrt{2}x/w_0)}U_k(x,0)dx = \sqrt{\frac{2^i i!}{2^k k!}}\delta_{mi} \tag{A.3d}$$

Eqn. (A.3a) is the orthonormality condition; eqns. (A.3b) and (A.3c) are recursion relations to be used to derive Hermite polynomials of any order, beginning with $H_0(x) = 1$. In two dimensions the Hermite-Gaussian modes are given by

$$U_{mn} = U_m(x, z)U_n(y, z)e^{-ikz} \tag{A.4}$$

with the plane wave phase shift factor included for completeness [25].

A.2 The wavefront distortion operator

The generator for the wavefront distortion operator is given in eqn. (58b). Multiplying the operator which is given between the bra-ket by $H_q(x)H_r(y)/H_q(x)H_r(y)$ and expanding the numerator as a series of Hermite polynomials, one obtains

$$H_i(x)H_j(y)H_q(x)H_r(y) = \sum_{st} h^{ij}_{st,qr} H_s(x)H_t(y) \tag{A.5}$$

Substituting eqn. (A.5) back into eqn. (58b) and using (A.3d) finally gives

$$T^{ij}_{op,qr} = \frac{h^{ij}_{op,qr}}{2}\sqrt{\frac{2^o o!2^p p!}{2^q q!2^r r!}} \tag{A.6}$$

In particular, for a simple tilt around the y-axis one gets eqn. (59).

A.3 The lateral shift operator

If a beam is laterally shifted with respect to the direction of propagation, the shift operator $O(\Delta x,\Delta y)$ is defined as

$$E(x + \Delta x, y + \Delta y, z) = O(\Delta x, \Delta y) \otimes E(x, y, z) \tag{A.7}$$

Expanding the left hand side in a Taylor series about x and y gives

$$O(\Delta x, \Delta y) = exp\left(i\left(\Delta x \frac{1}{i}\frac{d}{dx} + \Delta y \frac{1}{i}\frac{d}{dy}\right)\right) \tag{A.8}$$

In the modal basis, this unitary operator can be written as

$$O_{mn,kl}(\Delta x, \Delta y) = \langle mn| exp\left(i \sum_{op,qr} |op\rangle\left(\frac{\sqrt{2}\Delta x}{w(z)} T^x_{op,qr} + \frac{\sqrt{2}\Delta y}{w(z)} T^y_{op,qr}\right)\langle qr|\right)|kl\rangle \tag{A.9a}$$

$$\text{with} \quad T^{x}_{op,qr} = \delta_{pr} \int_{-\infty}^{\infty} dx\, U^{\dagger}_{o}(x,z) \frac{w(z)}{i\sqrt{2}} \frac{d}{dx} U_{q}(x,z) \tag{A.9b}$$

where the straightforward integration over y is already done. $T^{y}_{op,qr}$ can be deduced from the right hand side of eqn. (A.9b) by replacing x with y and by interchanging the indices o,p with q,r. Once again, the recursion relations of eqn. (A.3) are used to solve the integration:

$$H_r\left(\frac{\sqrt{2}x}{w(z)}\right) \frac{w(z)}{i\sqrt{2}} \frac{d}{dx} U_r(x,z) = \left(\frac{1}{2} H_{r+1}\left(\frac{\sqrt{2}x}{w(z)}\right) t + r H_{r-1}\left(\frac{\sqrt{2}x}{w(z)}\right) t^{*}\right) U_r(x,z) \tag{A.10a}$$

$$\text{where} \quad t = i - \frac{w(z)^2 k}{2R(z)} = i - \frac{z}{z_0} \tag{A.10b}$$

The generator of shifts in x is obtained by using eqn. (A.3d):

$$T^{x}_{op,qr} = \frac{1}{\sqrt{2}} \delta_{pr} (\sqrt{o}\, t\, \delta_{o,q+1} + \sqrt{q}\, t^{*} \delta_{o,q-1}) \tag{A.11}$$

A.4 The demodulation operator

If Ω denotes the area of the photodetector, the demodulated signal is given by:

$$\begin{aligned} S = & \iint_{\Omega} dx\, dy\, p(x,y) [P(\eta,x,y) E^{CR}(x,y)]^{\dagger} [P(\eta,x,y) E^{SB-}(x,y)] \\ & + \iint_{\Omega} dx\, dy\, p(x,y) [P(\eta,x,y) E^{SB+}(x,y)]^{\dagger} [P(\eta,x,y) E^{CR}(x,y)] \end{aligned} \tag{A.12}$$

where $p(x,y)$ is a pupil weighting function and where $E^{CR}(x,y)$ and $E^{SB\pm}(x,y)$ are the field amplitudes at the output of an optical system for the carrier and sidebands of the modulated light, respectively. $P(\eta,x,y)$ is the propagator between the output and the photodetector. In the modal space coordinates the first term in eqn. (A.12) becomes

$$\sum_{mn,kl} (E^{CR}_{mn})^{\dagger} e^{i(m+n+1)\eta} \iint_{\Omega} dx\, dy\, p(x,y)\, U^{\dagger}_{mn}(x,y,z)\, U_{kl}(x,y,z)\, e^{i(k+l+1)\eta} E^{SB-}_{kl} \tag{A.13}$$

Comparing this expression with the definition of the demodulation operator in the modal space in eqn. (65) gives

$$D^{\Omega}_{mn,kl} = \iint_{\Omega} dx\,dy\; p(x,y)U^{\dagger}_{mn}(x,y,z)U_{kl}(x,y,z) \tag{A.14}$$

When the photodetector size is constant relative to the beam spot size, the demodulation operator is independent of the position of the photodetector. For a full-plane detector the pupil weighting function becomes $p(x, y) = 1$ and eqn. (A.14) reduces to the orthonormality condition of eqn. (A.3a), i.e.

$$D^{full-plane}_{mn,kl} = \delta_{mk}\delta_{nl} \tag{A.15}$$

For a half-plane detector which is split along the y-axis and where the signals from the two half-planes are subtracted from each other the pupil weighting function is $p(x, y) = 1$ for $x \geq 0$ and $p(x, y) = -1$ for $x < 0$. The integration can then be written as:

$$\iint_{\Omega} dx\,dy\,p(x,y) \rightarrow \int_{-\infty}^{\infty} dy \left\{ \int_{0}^{\infty} dx - \int_{-\infty}^{0} dx \right\} \tag{A.16}$$